University of California Santa Barbara

FINAL REPORT (2019)

Department of Energy Grant: DOE DE-SC0008879

DUCTILE-PHASE TOUGHENED TUNGSTEN FOR PLASMA FACING MATERIALS

DE-FG03-94ER54275 (UCSB)

PI: G. Robert Odette (odette@engineering.ucsb.edu)

Md Ershadul Alam, Kevin Cunningham

University of California, Santa Barbara, CA

Submitted to

Daniel Clark (Program Manager)

Office of Fusion Energy Sciences, FES SC-24

US Department of Energy

Submission Date: September, 2019

ABSTRACT

Tungsten (W) and W-alloys are the leading candidates for plasma-facing components in nuclear fusion reactors because of their high melting point, high temperature strength, good thermal conductivity and low sputtering yield, however, they are too brittle to serve a structural function. A variety of processing approaches were employed to fabricate ductile-phase-toughened (DPT) tungsten (W) composites, that includes consolidating elemental W powder with Cu- or WC-coated W-wires via spark plasma sintering (SPS). Laminated W-composites with Cu-foils were also fabricated by hot-pressing or brazing. Mechanical testing and analytical modeling were used to guide composite development. The fracture toughness of thin W plate or laminated W-composites was measured in three-point bending (3PB) at room temperature (RT). Crack arrest and crack bridging were observed for the laminated composites, and fracture resistance curves were successfully calculated. An analytical model of crack bridging was developed using the specimen geometry, matrix properties, and the stress-displacement function of a ductile reinforcement ("bridging law") to calculate the fracture resistance curve (R-curve) and load-displacement curve (P-D curve) for any test specimen geometry. The code was also implemented to estimate the bridging law of an arbitrary composite using R-curve data.

In another approach, commercially available liquid-phase sintered W alloys with four different compositions were characterized in terms of microstructure, tensile and fracture toughness at different specimen, size, geometry and testing temperatures. The room temperature (RT) average maximum load fracture toughness values (K_{Ic} or K_{Jm} ≈ 38 to 107 MPa√m) of WHA, containing only 3 to 10 wt.% of a NiFe-based ductile phase (DP), are ≈ 5 to 13 times higher than for monolithic W (≈ 8 MPa√m). Most RT tests show extensive stable ductile tearing (DT) at all W contents, including 97W (K_{Jm} ≈ 69 MPa√m), for small baseline bend bars (B=1.65mm, W=2B). Exceptions to DT, include RT elastic fracture at 97W observed in 3x larger specimens than the baseline specimens. However, the WHA K_{Ic} was

still almost 5 times higher than that for monolithic W. The other exception to RT ductile tearing was for some of the 6 to 8x larger 95W alloy specimens that contained large ceramic initiating inclusions at the precrack front, along with lower DP%, with a $K_{Ic} \approx 59$ MPa$\sqrt{m}$, compare to their stable DT $K_{Jm} \approx 82$ MPa$\sqrt{m}$. Small specimen tests down to -196°C, to partially emulate irradiation hardening, also transition to elastic fracture at a temperature (-150 for 90W to -25ºC for 97W) that depends on the W content. However, even at -196°C, the K_{Ic} at 97W is ≈ 3 times that of monolithic W at RT. In contrast to classical ductile phase toughening by macrocrack bridging, WHA toughening mainly involves new mechanisms associated with arrest, blunting and bridging of numerous process zone microcracks. Later, these WHAs were used to fabricate W-WHA hybrid composites by coating elemental W powder on WHA using SPS. Three-point bend bars were fabricated and fracture toughness was tested at room temperature. Crack initiated and propagated from W-part to the WHA part for the well-bonded (interface) W-WHA composites for 90 and 92.5WHAs, however, crack arrested and diverted at/or through the interface for loosely bonded W-95/97WHAs with increasing load.

ACKNOWLEDGEMENTS

We gratefully acknowledge the support provided by U.S. Department of Energy through the Office of Fusion Energy Sciences (DOE DE-SC0008879, at UCSB: DOE 8-442520-22403-3 ROF02). Our initial work on the W-FeNi WHA was in collaboration with Drs, C. Henager and R. Kurtz at PNNL. We also thank our UCSB colleagues Dr. S. Pal, K. Fields and D. Gragg for their important contributions to this work. The U.S. National Science Foundation supported California Nanoscience Institute provided facilities critical the success of this research.

DISCLAIMERS

This final report contains four chapters.

Chapter No	Title	Page No
Chapter 1	Ductile Phase Toughened Tungsten for Plasma Facing Materials	1
Chapter 2	On the Remarkable Fracture Toughness of 90 to 97W-NiFe Alloys Revealing Powerful New Ductile Phase Toughening Mechanisms	49
Chapter 3	Influence of Specimen Size, Geometry and Large Impurity Inclusions on the Fracture Toughness of Tungsten Heavy Metal Alloys	91
Chapter 4	On the Fracture Behavior of WNiFe Heavy Metal Alloy Hybrids	113

TABLE OF CONTENTS

LIST OF FIGURES

LIST OF TABLES

CHAPTER 1
DUCTILE PHASE TOUGHENED TUNSTEN FOR PLASMA-FACING MATERIALS

ABSTRACT

A variety of processing approaches were employed to fabricate ductile-phase-toughened (DPT) tungsten (W) composites. Mechanical testing and analytical modeling were used to guide composite development. This work provides a basis for further development of W composites to be used in structural divertor components of future fusion reactors.

W wire was tested in tension, showing significant ductility and strength. Coatings of copper (Cu) or tungsten carbide (WC) were applied to the W wire via electrodeposition and carburization, respectively. Composites were fabricated using spark plasma sintering (SPS) to consolidate W powders together with each type of coated W wire. DPT behavior, e.g. crack arrest and crack bridging, was not observed in three-point bend testing of the sintered composites.

A laminate was fabricated by hot pressing W and Cu foils together with W wires, and subsequently tested in tension. This laminate was bonded via hot pressing to thick W plate as a reinforcing layer, and the composite was tested in three-point bending. Crack arrest was observed along with some fiber pullout, but significant transverse cracking in the W plate confounded further fracture toughness analysis.

The fracture toughness of thin W plate was measured in three-point bending. W plates were brazed with Cu foils to form a laminate. Crack arrest and crack bridging were observed in three-point bend tests of the laminate, and fracture resistance curves were successfully calculated for this DPT composite.

An analytical model of crack bridging was developed using the basis described by Chao in previous work by the group. The model uses the specimen geometry, matrix properties, and the

stress-displacement function of a ductile reinforcement (“bridging law”) to calculate the fracture resistance curve (R-curve) and load-displacement curve (P-D curve) for any test specimen geometry. The code was also implemented to estimate the bridging law of an arbitrary composite using R-curve data.

Finally, a parametric study was performed to quantitatively determine the necessary mechanical properties of useful toughening reinforcements for a DPT W composite. The analytical model has a broad applicability for any DPT material.

1.1. INTRODUCTION

The objective of this study is to develop the materials science of tungsten (W) composites as candidates for plasma-facing components (PFCs) in future fusion reactors [1-6]. Tungsten and W-alloys are the leading candidates for the PFCs of future fusion reactors, such as the International Thermonuclear Experimental Reactor (ITER) and Demonstration Power Plant (DEMO), because of their high melting point, strength at high temperatures, and low sputtering yield [7-11]. In the design for ITER, W is implemented solely as a non-structural armor in the divertor component. An excellent overview of the divertor design may be found in recent work by Merola et al. [12] The goal for this study and others worldwide is to develop structural W materials to enable advanced divertor designs [13].

Tungsten and most W alloys exhibit low fracture toughness (K_{IC}) and a high ductile-brittle transition temperature (DBTT) that would render them as brittle materials in pulsed reactor operations [7, 9, 14]. The DBTT for unirradiated W-alloys typically ranges from 573K to 1273K (300 to 1000°C) and in a reactor environment radiation hardening would further elevate this range [9, 15, 16]. Metallurgical approaches to toughen W alloys, including alloying with rhenium (Re) and severe plastic deformation (SPD), have resulted in modest DBTT decreases [15, 17].

However, they would be difficult or impossible to implement, due to high costs and implications to irradiation hardening (W-Re alloys) or complex processing demands (SPD) [18-20]. To prevent mechanical failure, a toughening mechanism is needed for W before it can be considered an effective plasma facing component material (PFCM).

There are several types of tungsten under consideration for fusion reactor components. These include the oxide dispersion strengthened alloy WL10 (W-1.0La_2O_3), the cemented composite MT-185 (W-2.1Ni-0.9Fe), and other fiber-reinforced or laminated composites with a variety of secondary/debonding phases [13, 21]. Composite development is still in the early stages, and these materials are not available on a commercial scale.

W-alloys toughened by engineered reinforcement architectures, such as ductile-phase toughening (DPT), are strong candidates for PFCMs. Previous work on a commercial W-Cu material was promising, showing nearly a threefold improvement in fracture resistance over monolithic W by reinforcing the matrix with 50% Cu by volume [2]. Copper is not a viable reinforcement choice for DPT tungsten PFCMs because of its relatively low melting point; however, it is useful for fabricating model composites because it is immiscible in W [22].

This study aims to demonstrate DPT in a model W composite, and to preserve and advance the analytical modeling of DPT materials. This thesis will first describe the experimental methodology and results of fabricating and testing W composites, followed by the approach and results of computational efforts.

1.2. EXPERIMENTAL PROCEDURES

1.2.1 Ductile Phase Toughening

In DPT, a ductile phase is included in a brittle matrix to prevent fracture propagation. This is accomplished by the formation of an intact bridging zone behind the crack tip, which provides

reinforcement, resulting in an increase in the remote load stress intensity for continued crack growth with increasing crack length [23-25]. The principles of DPT are illustrated in Figure 1.2.1, which shows ductile bridging ligaments stretching across an open crack in a W-Cu composite [3].

For a brittle material containing a suitable volume fraction of a ductile phase, a highly effective resistance curve toughening mechanism develops as the crack extends. As the crack propagates through a brittle matrix, it leaves a bridging zone of ductile ligaments over a length L behind the crack tip. As the crack extends, L increases. The ligaments act in opposition to the applied loading stress intensity factor, $K_{I,P}$. This reduces the effective crack tip stress intensity factor so that $K_{I,eff} < K_{I,P}$. For small-scale bridging, when the bridging zone is much smaller than the length of the crack, the bridging zone size and the fracture resistance both reach steady-state values. This study focuses on large-scale bridging, where the material fracture resistance does not reach a steady-state value for a small test specimen. The crack opening (Δ) increases with increasing distance behind the crack-tip until the reinforcement breaks at its failure displacement, Δ_2 [23-25].

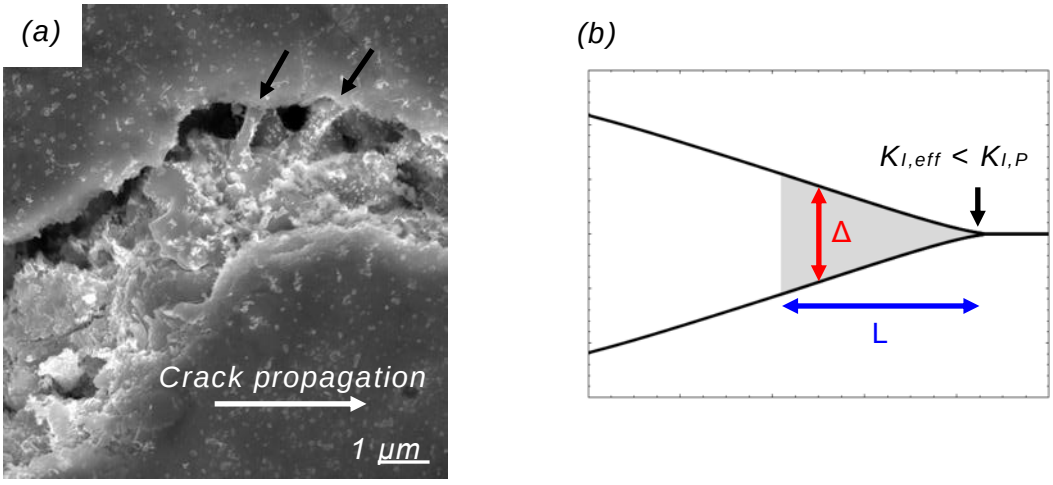

Figure 1.2.1. a) SEM image of Cu ligaments (indicated by black arrows) bridging a crack in a W-Cu composite. b) Schematic of cracked material oriented showing crack-face displacement (Δ) and bridging zone length (L). The effective stress intensity at the crack tip is shielded by a reinforcing material (the shaded area) [3].

There are many choices for ductile phases. Copper is useful for fabricating model W composites because it is immiscible with W and does not form brittle intermetallic phases [22]. Another option explored in this study is W wire, which has high strength and some ductility, and can be coated with a weak debonding interface material. Maximizing the volume fraction of W in the final composite is preferable for reducing activation and plasma contamination in a fusion reactor [26], so W wires are an attractive reinforcement option.

1.2.2 Materials

Elemental W powder of 99.95% purity with a particle size of 4-6μm from Stanford Materials was used in this study. An additional W powder, cryogenically milled from this pure 4-6μm precursor at Aegis Technology, was also examined, but ultimately not used because it contained tantalum oxide impurities. The pure powders were consolidated via spark plasma sintering (SPS) to form pure W disks and composites.

Tungsten wires of varying diameter (15, 250, and 500 μm, 99.95% purity) were ordered from Alfa Aesar for use as ductile reinforcements. Each wire size was tested in tension, and 250-μm wire was used in fabricating both sintered and hot-pressed composites.

Tungsten and copper foils were ordered from ESPI Metals (W, 99.98% purity) and Basic Copper (Cu, 99.9% purity), respectively, with nominal thickness 127 μm. Both materials were tested in tension and then used to fabricate a hot-pressed laminate.

Tungsten plate of 1 ± 0.2 mm thickness and 99.97% purity was ordered from Plansee, and subsequently sent to Production Lapping for lapping to smooth and parallel the top and bottom surfaces. Surface roughness after lapping was measured to be less than 1 μm. The material toughness was measured in precracked three-point bending and the plates were used to fabricate a brazed composite.

1.2.3 Fabrication Techniques

1.2.3.1 Spark Plasma Sintering

Disk-shaped specimens were consolidated from elemental W powders using spark plasma sintering. SPS is a rapid consolidation technique that uses an electric current to heat a conductive powder directly (insulating powders are heated by the conductive die set) combined with uniaxial compression in a vacuum chamber. Figure 1.2.2 shows a schematic diagram of the SPS process.

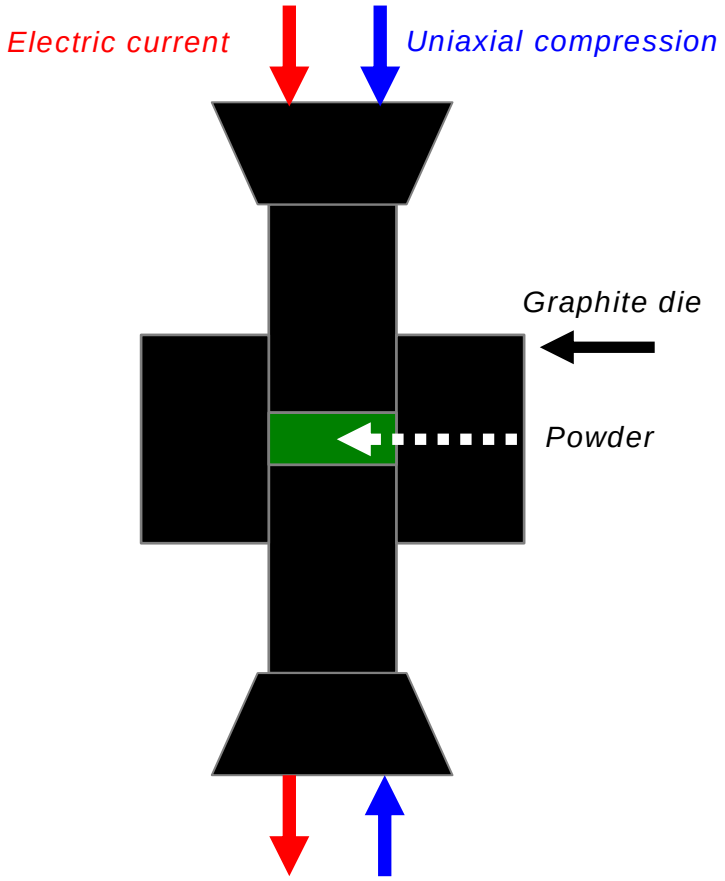

Figure 1.2.2. Schematic diagram of SPS process. The electric current heat the die set and powders. The powder is loaded in uniaxial compression.

The powder was loaded under an argon environment into a 20-mm inner-diameter graphite die with a layer of 0.15” graphite foil between the powder and die. Additional specimens were prepared using 0.005” niobium (Nb) foil instead of graphite foil, to reduce formation of tungsten carbide [27]. When using Nb foil, one layer of foil was used for each face of the disk, and two layers were used around the circumference of the die. An initial study of the effect of temperature and dwell time on density was carried out to optimize the process. Composites were fabricated by laying up coated W wires within the W powder in the SPS die and consolidating the mixture.

Sintering temperatures between 990 and 1900 °C were used for various specimens as detailed later in this report. Dwell times up to 1 hour were used. The heating rate was 100 °C/min for each specimen, and continuous electric current was used (in contrast to a pulsed current).

After sintering, the disks were polished to remove any residual graphite. The disks were sectioned using a low-speed diamond saw (Buehler), then mounted and polished to 0.5 µm. A 5 x 5 mm section was also cut for density measurements. The grain size was determined optically after etching in a 30% hydrogen peroxide solution for 10 minutes in an ultrasonic bath [28].

1.2.3.2 Electrolytic Plating

Copper is a good choice for fabricating model W composites because of its immiscibility in W. Plating W wires with Cu was investigated as a means of creating a weak debond layer for the composite. To prepare the wires for plating, first they were wiped with mineral oil to remove large particles, then soaked in an ultrasonic bath at 50°C for 15 minutes (solution: 0.1g sodium carbonate, 0.3g sodium borate in 19.6g water). The clean wires were plated at 50°C under direct current, 162 A per m_2 of immersed wire (aqueous solution of 0.625M sulfuric acid, 0.4M copper sulfate, and 2 g/L urea) [29-31].

A small-scale plating apparatus was constructed using a rectangular bath (3 x 5 cm by 10 cm tall) with three bus wires running above the plating solution. The two outer bus wires were connected and Cu wire was hung from them to form the cathode. W wire was hung from the center bus to form the anode (See Fig. 1.2.3 for diagram). Eight lengths of tungsten wire were plated simultaneously for 35 minutes with approximately 8cm immersed in the plating solution for each. Plating thickness was measured with a micrometer.

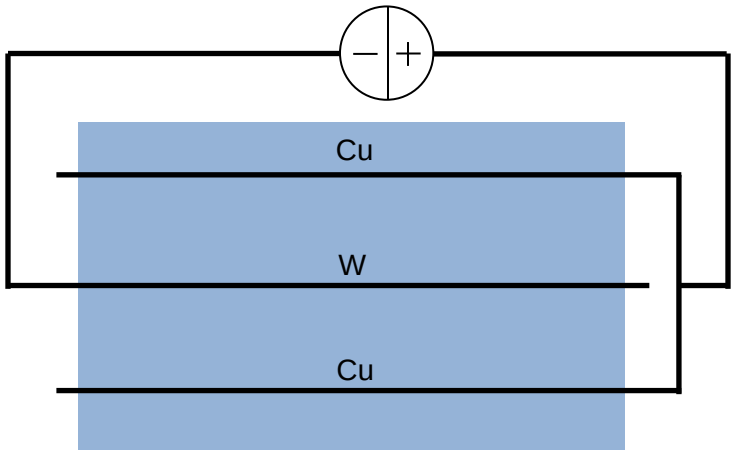

Figure 1.2.3. Top-down schematic of plating apparatus. The bare wire above the plating bath allows multiple lengths of current-carrying wire to be suspended within the bath. The W and Cu labels indicate the wire that hangs from each bus [2].

1.2.3.3 Carburization

Tungsten carbide was investigated as a potential highly stable debonding layer because C is a suitable element for the divertor in terms of low neutron activation and reduced potential for plasma contamination [26]. 12-mm lengths of 250-μm W wire were placed apart in loose graphite powder (2-15 μm particle size, Alfa Aesar), and then compacted at 35 MPa at ambient temperature in the SPS system. The compact was heat treated at 1800°C for 1 minute under vacuum with a heating ramp of 300°C/min under a minimum load of 9 MPa. Coated wires were cleaned in an ultrasonic bath to remove excess graphite particles.

1.2.3.4 Hot Pressing

To avoid the issue of Cu melting and wicking during the sintering of a W matrix, a hot-pressing fabrication route was developed for W wires sandwiched between W and Cu foils, as illustrated in Figure 1.2.4a-b. The top and bottom layers were 127-µm W foils. The inner layers were the 127-µm Cu foils, while the middle layer contained 250-µm W wires. The laminate was 50 x 50mm, with an average of 50 µm at the shortest distance between the parallel fibers. After hot pressing at 900°C at 38 MPa for 5 minutes, the W-wires were embedded in the Cu, forming a 3-layer sandwich.

The W-foil/Cu/W-wire sandwich reinforcement was then hot pressed between 4-mm thick W plates, as illustrated in Figure 1.2.4c. Since the surface roughness of the reinforcement was ≈ 100 µm, reflecting the underlying topology of the stronger W-wires, a Cu bond layer of 127-µm foil was used between the W-plates and sandwich. The volume fraction of Cu was approximately 10% in the laminate as shown in Figure 1.2.4c.

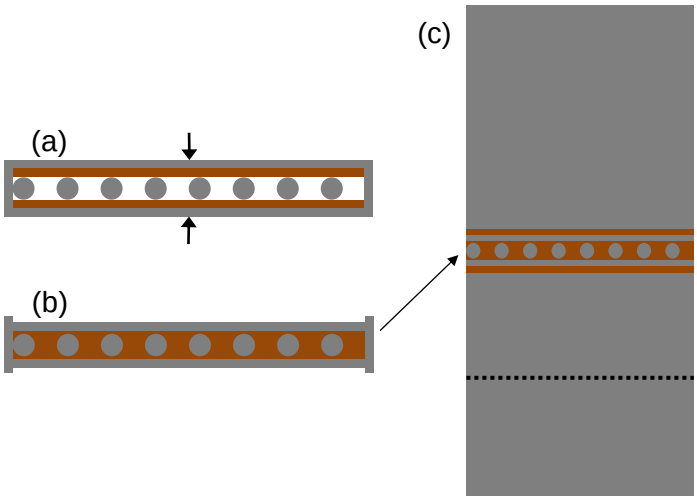

Figure 1.2.4. Schematic diagram of hot-pressed reinforcement cross-section a) before and b) after hot pressing, as well as c) the schematic diagram of hot-pressed bend specimen cross-section. Dashed line indicates notch depth. Note that images (a) and (b) are the same scale, while (c) is not [4].

1.2.3.5 Brazing

Diffusion bonding of W to Cu via hot pressing was found to be inconsistent, so brazing W plates with thin layers of Cu was explored. Lapped 0.85 x 50 x 50 mm W plates were stacked alternating with 75-μm Cu foils, and secured with stainless steel wire. The W plates were aligned using the rolling direction. One of the outer plates was rotated 90° from the others, as will be discussed later. The layup was heated in an Ar-5%H_2 environment to 1113 °C at 15 °C/min and held for 6s before cooling.

1.2.4 Measurements and Mechanical Tests

1.2.4.1 Microhardness Testing

The hardness of the SPS-consolidated W was measured using a Leco M-400A microhardness tester. A series of 8-10 indents was made along the cross-section of each disk with a load of 500g. Indent locations were chosen manually to avoid scratched areas. The hardness of the W wire was measured before and after several high-temperature processing steps using the same methods.

1.2.4.2 Density Measurements

The density of SPS-consolidated disks was calculated using a Micrometrics AccuPyc 1330 helium pycnometer. Disk sections were cleaned, dried, and weighed on a balance to an accuracy of 10 μg. For each pycnometer measurement, the instrument was calibrated with a reference volume and the sample volume was taken as the average of 10 measurements.

1.2.4.3 Tensile Testing

Tensile testing of 15-, 250-, and 500-μm tungsten wire was performed using techniques and equipment developed for ceramic fiber testing. The 15-μm wire specimens were prepared by mounting each length of wire to a rigid holder with epoxy, and then severing the holder once

installed in the grips. The 250- and 500-μm wire specimens were prepared by sandwiching the ends of each wire section in epoxy between two polyamide plates. Tests were performed at ambient temperature in air at a crosshead displacement rate of 0.5 mm/min.

Tensile tests were performed on 127 μm thick W and Cu foils at a strain rate of 0.011 min^{-1} at ambient temperature in air, with a gauge length and width of 9 mm and 2 mm, respectively. Specimens were prepared by punching directly from the stock material. Strain was measured with a laser extensometer.

Tensile test samples of the hot-pressed W-Cu reinforcement (See Fig. 1.2.4b) were EDM-cut with a gauge length, width, and thickness of 6.4 mm, 2.45 mm, and 0.8 mm, respectively. The tensile direction was parallel to the wire direction. Tensile testing was performed with crosshead displacement rates of 0.1 and 0.1125 mm/min at ambient temperature in air.

1.2.4.4 Fracture Testing

Notched specimens of the W-WC sintered composite were tested in three-point bending with the goal of observing debonding behavior during crack propagation. Notched three-point bend test samples were EDM-cut with a test span, width, thickness, and notch depth of 10 mm, 3.6 mm, 3.6 mm, and 0.5 mm, respectively. The crack propagation direction was perpendicular to the wire direction. Bend testing was performed with a crosshead displacement rate of 0.05 mm/min at ambient temperature in air.

For the hot-pressed W-Cu composite, notched three-point bend test samples were EDM cut with a test span, width, thickness, and notch depth of 27.6 mm, 8.9 mm, 3.1 mm, and 2 mm, respectively. The crack propagation direction was perpendicular to the wire direction. Bend testing was performed with a crosshead displacement rate of 0.02 mm/min at ambient temperature in air.

For the 1-mm W plates, notched bend bars were EDM-cut with dimensions 21 x 4.65 x 0.85 mm with a notch depth of 0.93 mm. Specimens were pre-cracked by standing them upright in a load frame with the span along the fatigue loading direction as shown in Figure 1.2.5. The specimens were compression-compression fatigued at 20 Hz and the crack length was observed at intervals of 10,000 cycles until reaching a length of approximately a/W = 0.3. The pre-crack depth was marked by applying a dye penetrant prior to fracture testing and observed on the fracture surface. Tests were performed on a 20.5-mm span at ambient temperature in air with a crosshead displacement rate of 0.05 mm/min.

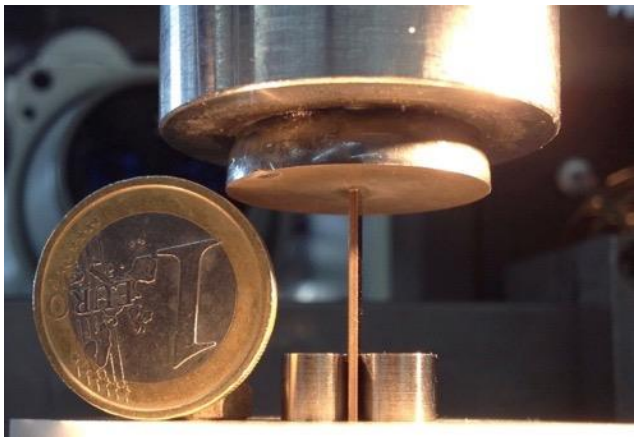

Figure 1.2.5. Photograph of end-on compression fatigue setup for 0.85-mm thickness W bend bars. A steel clip is used to help stand the specimen upright. A coin is shown for scale [5].

For the W-Cu brazed laminate, notched three-point bend bars were EDM-cut with dimensions 21 x 4.65 x 2.125 mm with a notch depth of 0.93 mm. Specimens were separated into “edge” and “face” categories, for which the direction of crack propagation was normal to the edge or face of the ductile laminate layers, respectively. Specimens were labeled “L” or “T” with respect to the rolling direction of the W plates they contained, indicating if the crack propagation direction was

parallel (L) or perpendicular (T) to the rolling direction. Additional specimens were created with a mixture of L and T plates, called L+T.

Several specimens were fatigued in three-point bending to attempt to develop a precrack, without success. Those that did not develop a pop-in to a/W ≈ 0.9 were tested on a 20.5-mm span at a crosshead displacement rate of 0.1 mm/min.

The majority of brazed laminate specimens were pre-cracked to a/W ≈ 0.3 in compression-compression fatigue, similar to the pure W plate specimens. Tests were performed on a 20.5-mm span at ambient temperature in air at a crosshead displacement rate of 0.05 mm/min. A microscope mounted on the load frame was used to observe the increments of crack growth for correlation with the load-displacement data. The crack shape at the end of each test was marked by oxidizing the W surface at 400°C in air.

1.2.5 Data Analysis

1.2.5.1 Tensile Testing

Engineering stress was calculated using the initial cross-section of the test specimen. For the W wires, the yield stress was calculated using an analogy to the 0.2% strain offset method, where the displacement divided by the initial gauge length was used instead of strain. For the pure W and Cu foils, yield stress was calculated using the 0.2% strain offset method. For the hot-pressed laminate reinforcement, engineering stress was calculated using the initial cross-section of all material in the laminate, excluding porosity, for the initial elastic loading. After the load drop, engineering stress was calculated assuming only the Cu foils were intact.

1.2.5.2 Fracture Testing

For three-point bend tests, the maximum load at each increment of measured crack length was used to calculate the fracture resistance corresponding to the arrested crack length following

ASTM E399-12 [32]. For toughness measurements of brittle materials such as the W plate, only the initial precrack length was used. For the W-Cu brazed laminate, multiple crack lengths were measured during each test, giving rise to a resistance [K_{IR}(da)] curve associated with crack bridging by the ductile layer.

Some composite test specimens were not precracked, and as such they cannot provide real fracture toughness data. Nevertheless, these tests still guided fabrication efforts by indicating whether debonding occurred between the matrix and reinforcement.

1.3. EXPERIMENTAL RESULTS

1.3.1 Materials

1.3.1.1 Tungsten Wire

Table 1.3.1 summarizes the tensile properties of W-wire of various diameters. A general trend of increased strength and decreased ductility is observed as the wire diameter decreases. The tested specimens were examined microscopically to verify cup-and-cone fracture to confirm uniform stress distribution in the wire. The ultimate strength reached a remarkable value of 4.31 GPa in the 15-μm wire, with about 1.0% total elongation. The larger diameter wires had lower strength but showed greater total elongation.

Table 1.3.1. Average values of W wire properties from tensile testing [4].

Diameter (μm)	Yield Stress (MPa)	Ultimate Tensile Strength (MPa)	Total Elongation (%)	Reduction in Area (%)
15	3.58	4.31	1.0	N/A
250	1.78	2.31	1.7	29.9
500	1.34	2.12	2.4	27.1

The 250-µm W wires, used to make various composites, were analyzed with EBSD to quantify how their properties evolved after several of the high-temperature fabrication steps. After processing at 1900°C for 5 minutes during the carburization process described above, a decrease in texture strength and a higher fraction of smaller grains was observed in the W wire as shown in Figure 1.3.1. The hardness of the wire decreased about 9% (from 673.6 to 613.0 HV) after 370 minutes at 900°C through 3 processing steps: 1) hot pressing at 38 MPa in vacuum for 5 minutes, 2) an oxide reduction in Ar-5%H_2 for 360 minutes, and 3) hot pressing at 34 MPa in vacuum for 5 minutes.

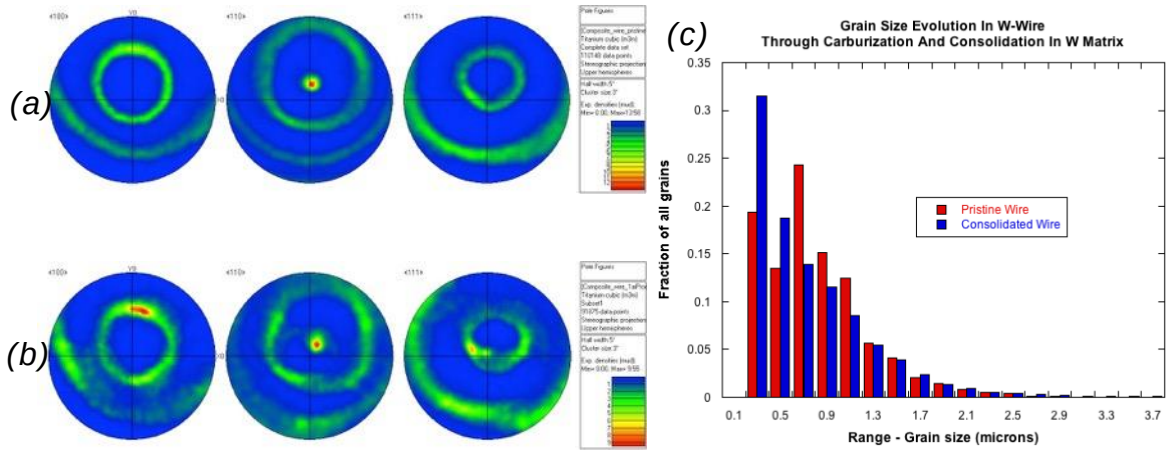

Figure 1.3.1. Microstructure evolution in W wire during processing to form W-WC composite. a) Pole figure contour maps for pristine wire showing {110} texture out of plane (axial direction of the wire). b) Pole figure contour maps for W wire after consolidation in composite showing qualitatively weaker {110} texture out of plane (more diffuse peaks). c) Histogram of grain sizes shows a higher fraction of smaller grains after processing. Note that in parts (a) and (b), the difference in the scan areas (110148 and 91875 data points, respectively) convolutes a quantitative interpretation of the difference in the peak intensities (13.58 and 9.55, respectively), requiring instead a qualitative comparison of peak sharpness.

1.3.1.2 Tungsten and Copper Foils

Representative stress-strain curves for the pure tungsten and copper foils are shown in Figure 1.3.2. The tensile properties are summarized in Table 1.3.2. The W-foil has a high strength and limited ductility. The Cu-foil has low strength, but high ductility.

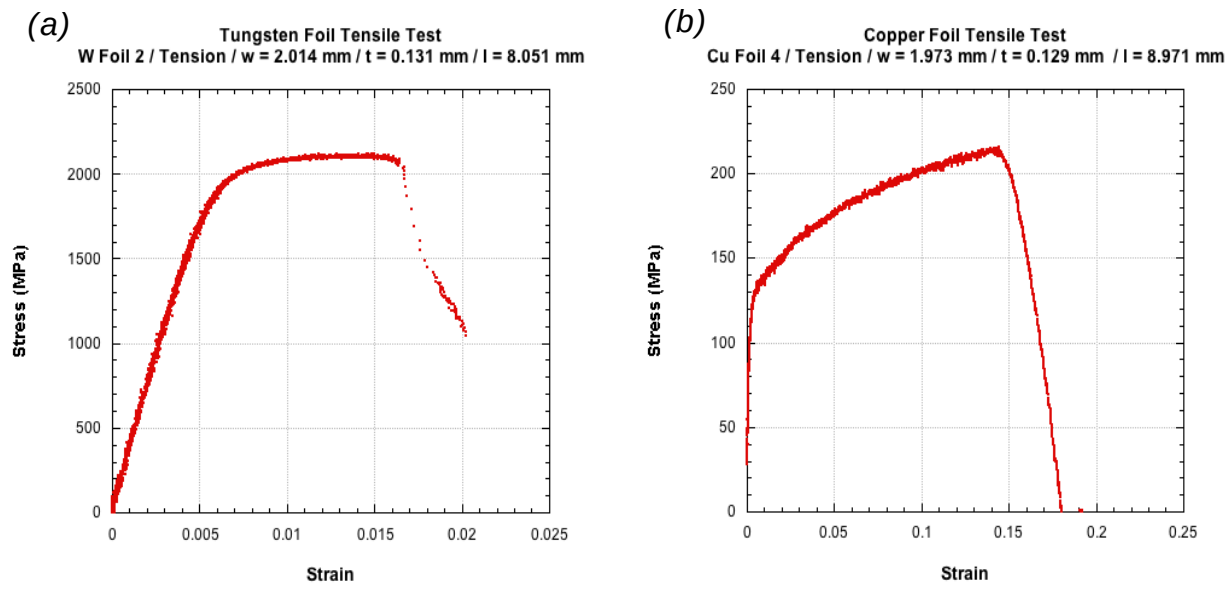

Figure 1.3.2. Representative stress-strain curves for a) tungsten and b) copper foils. Note the order-of magnitude differences for both the stress and strain axes between graphs [4].

Table 1.3.2. Summary of tensile data for W and Cu foils [4].

Material	Yield Stress (MPa)	Ultimate Tensile Strength (MPa)	Total Elongation (%)
W	1997.7 ± 10.5	2119.4 ± 4.5	3.4 ± 1.3
Cu	130.2 ± 4.6	218.7 ± 4.9	16.9 ± 3.3

1.3.1.3 Tungsten Plate

A summary of fracture toughness testing of the W plate in both the L and T orientations is shown in Table 1.3.3. The average W toughness and standard deviations were 13.06 ± 2.34 and 20.90 ± 0.45 MPa√m in the L and T directions, respectively.

Table 1.3.3. Summary of fracture toughness tests for pure W plate [5].

Specimen	a/W	Load (N)	Toughness (MPa√m)
L2	0.26	101.60	10.5
L5	0.28	98.96	10.7
L6	0.33	120.70	14.7
L7	0.27	129.73	13.6
L8	0.31	135.54	15.7
T2	0.27	195.29	20.5
T3	0.30	190.81	21.5
T6	0.27	199.55	20.9
T8	0.26	200.55	20.8

1.3.2 Sintered Composites

The results of the SPS consolidation study for pure W powders are summarized in Table 1.3.4. These results were used to establish acceptable parameters for consolidating sintered composites.

Table 1.3.4. Summary of SPS conditions and W disk properties.

Temperature (°C)	Dwell Time (mins)	Density (% Max)	Hardness (HV)	Grain Size (μm)
1700	1	79.8	165.1 ± 6.1	6.1 ± 1.5
1700	60	92.0	332.4 ± 9.6	8.7 ± 3.0
1900	21	91.3	322.0 ± 9.2	9.0 ± 2.8
1900	60	92.1	338.6 ± 7.3	13 ± 5.8
1900*	60	93.9	343.6 ± 6.8	29 ± 6.5
1900*	5	95.2	224.6 ± 3.3	7.2 ± 3.8

The percent given for density references a maximum density of 19.3 g/cm^3 for pure single-crystal tungsten. In each case the heating rate was 100 °C/min approaching the maximum temperature and the uniaxial pressure was 50 MPa. Asterisks indicate samples prepared using Nb foil instead of graphite [2].

After electroplating, micrometer measurements indicated an average Cu coating thickness of 30 μm on the W wires. The carburization process resulted in a 12-μm layer of WC on the wire. The summary of SPS composite fabrication processes and outcomes is shown in Table 1.3.5.

Table 1.3.5. Summary of process parameters for SPS system and outcomes for composite fabrication and W-wire carburization. Multiple lines per row indicate sequential processes on the same material [3].

Materials	**Pressing (MPa)**	**Heating rate (°C/min)**	**Dwell T (°C)**	**Dwell t (min)**	**Result**
Cu-coated W wire + W	50	100	1700	5	Cu melted, found in matrix pores
Cu-coated W wire + W	50 50	100 100	990 1700	25 0	Cu melted, found in matrix pores
W wire + C	35 9.5	- 300	- 1800	- 1	12- μm WC coating on W wires
WC-coated W wire + W	50	100	1900	10	WC intact at interface

In the case of the Cu-coated wires, neither direct sintering nor an attempt to partially consolidate W at low temperature before finishing at high temperature was successful in maintaining a Cu layer at the wire-matrix interface. Instead, a small amount of wicked Cu was found via energy dispersive x-ray spectroscopy (EDS) to coat the porous matrix, as shown in Figure 1.3.3. In contrast, the 12-μm WC coating was intact after consolidation.

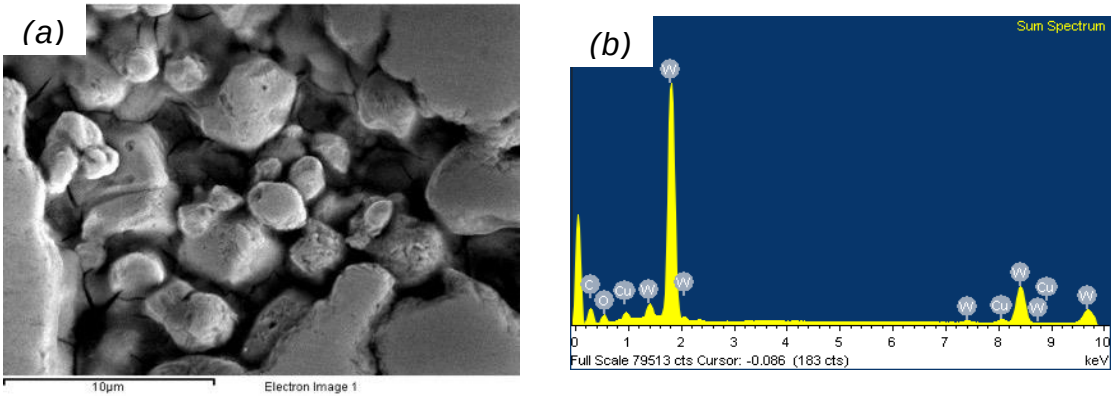

Figure 1.3.3. a) SEM image of a porous area in W matrix. Sample is single-temperature SPS route for W powder consolidated around Cu-coated W wires. b) EDS spectrum shows Cu detected in pore. The wire-matrix interface was characterized only by a change in porosity between the dense wire and the slightly porous matrix, and showed no contrast in scattering, microstructure, or chemistry (via EDS) [3].

No bridging was observed in the W-WC sintered composite, since the cracks ran directly though the coated wire without any debonding as shown in Figure 3.4. Despite the presence of some porosity at the WC-matrix interface, this may be due to the fact that the WC layer was strongly bonded to both the W matrix and wire. Further analysis of chemistry and crystal structure may indicate the extent of reaction to form both WC and W_2C, and may help to explore the shift in fracture character in the wire from the edges to the center.

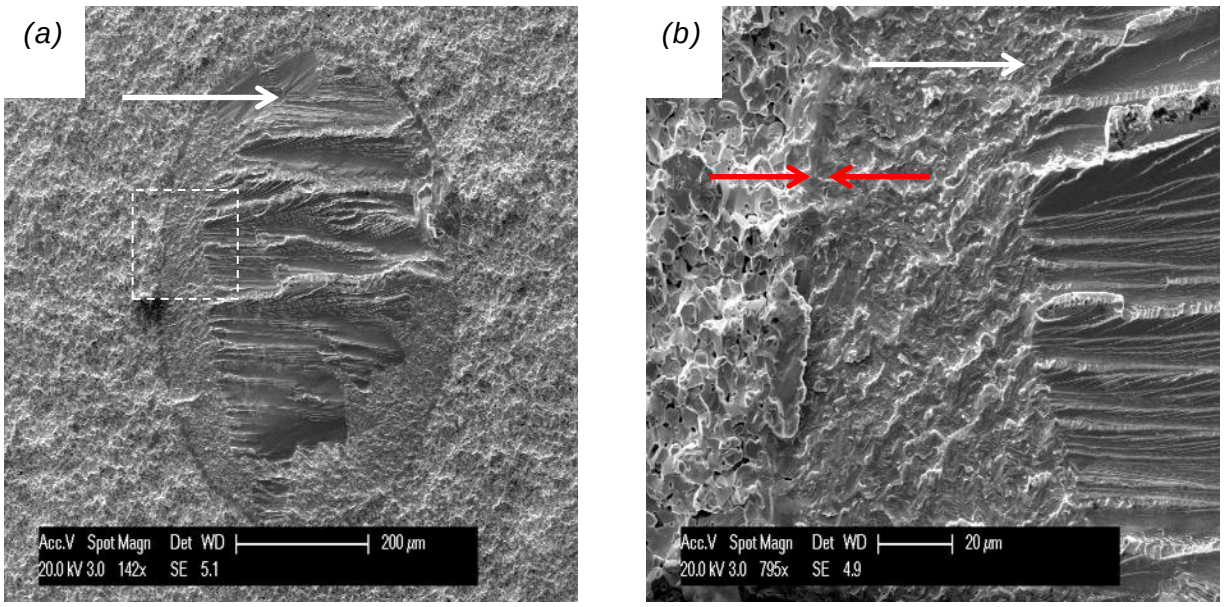

Figure 1.3.4. SEM images at 2 different magnifications of a W-WC bend bar fracture surface. White arrows indicate the direction of crack propagation. Red arrows show thickness of WC layer. There is no evidence of debonding along the W-WC interface.

1.3.3 Hot-Pressed Composites

The results of laminate reinforcement tensile testing are summarized in Figure 1.3.5. Note that the plot shows a single curve with a discontinuity, as the test was paused and resumed after the W foils cracked. The reinforcement showed some evidence of fiber pullout but no indication of plasticity in the W-wires. The outer W-foils cracked at the peak stress, followed by fracture of the W-wires. Deformation occurred in the Cu layer at a much lower stress until ductile failure.

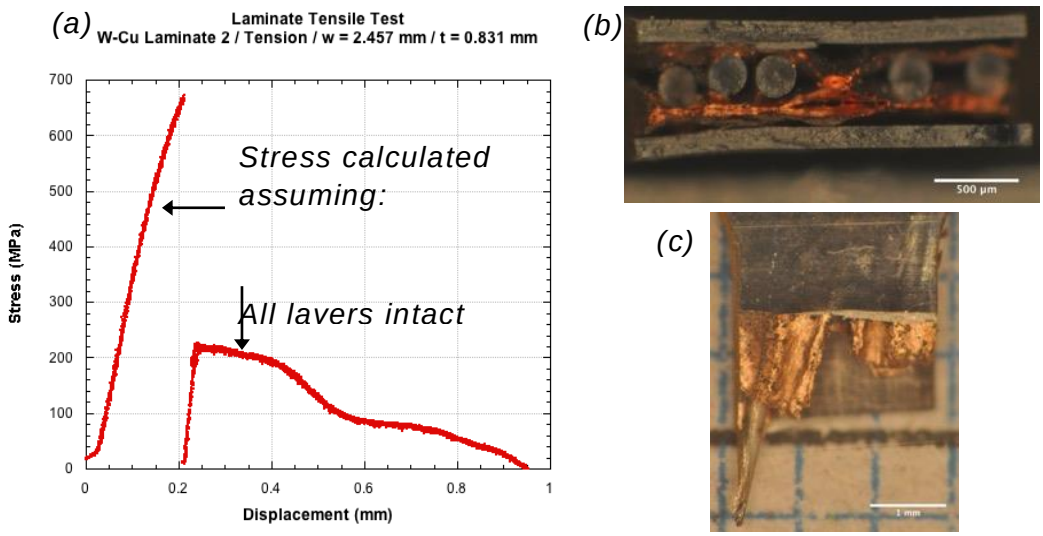

Figure 1.3.5. Summary of laminate reinforcement tensile tests. a) The stress-displacement curve uses the initial cross-sectional area of entire specimen for elastic loading, and the cross-sectional area of Cu only for plastic region. b) Fracture surface of specimen 1. Necking is seen in Cu but not in W foil or wire. c) Protruding W wire from specimen 2 suggests energy dissipation by pullout [4].

The results of laminate fracture testing are summarized in Figure 1.3.6. The stress was calculated using the applied load and initial geometry of the test specimen. In one test (specimen 1), the crack propagated through the W plate up to the embedded laminate and re-nucleated on the other side, leaving the reinforcement sandwich intact. At this point the specimen could only sustain a low load of ≈ 130 N. In a second test (specimen 2), cracks grew from the notch parallel to the sandwich, before branching with one crack deflecting 90° and propagating up to the sandwich at the first pop-in stress drop. This crack arrested and the stress increases again until the crack re-nucleated at the back of the sandwich marked by the second stress drop. However, the laminate composite was still able to sustain a significant load in this case, which actually then increased prior to a gradual drop-off associated with continued deformation of the sandwich layer. Removing the Cu using a nitric acid bath showed that several of the W wires had fractured between 0.075

to 1.4 mm away from the bending point, indicating that fiber pullout could play a role in the mechanical response of the composite. Peak-load stress intensity factor values ranged from 20 to 34 MPa√m.

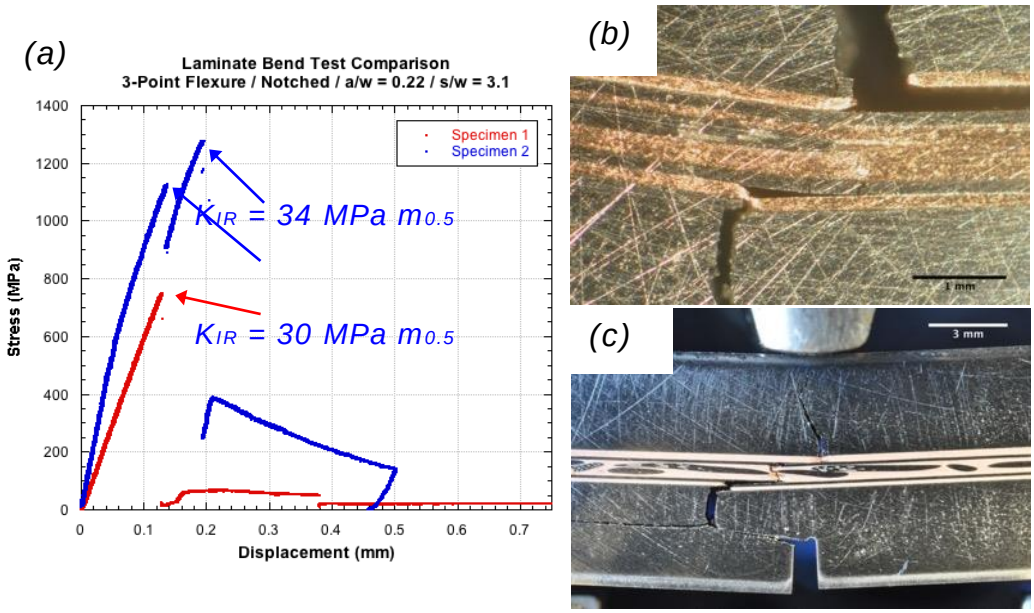

Figure 1.3.6. Summary of hot-pressed laminate fracture tests. a) Stress-displacement curves for two specimens are compared showing calculated stress intensity at peak load points. b) Specimen 1 after testing (notch side is bottom of image). c) Specimen 2 after testing [4].

1.3.4 Brazed Composites

Bend testing on the notched, non-precracked W-Cu laminate did not show pseudo-ductile behavior, but crack bridging did occur. In Figure 1.3.7, the dye penetrant on the fracture surface of the broken specimen indicates that when the specimen was still intact with an a/W ≈ 0.9, the Cu the reinforcement was bridging the crack. An increase in load-bearing capacity and fracture resistance is not seen in these specimens because the applied stress intensity needed to grow a

sharp crack from the blunt notch tip was greater than that needed to unstably propagate a sharp dynamic crack to a/W = 0.9, since the corresponding crack opening profile does not activate a significant bridging traction.

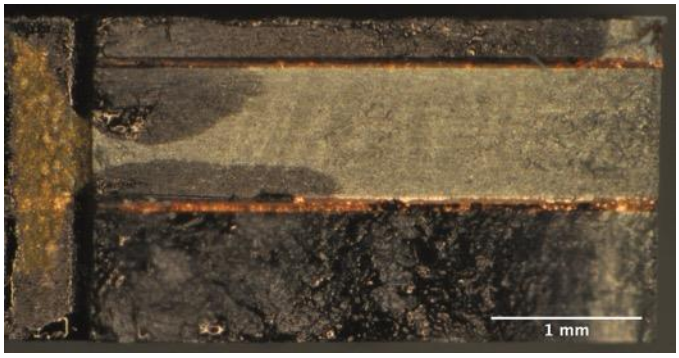

Figure 1.3.7. A representative fracture surface of W-Cu brazed laminate. Specimen was marked with dye penetrant at a measured a/W = 0.9 before breaking. Notch is on the left side of image. Lack of penetration through Cu layers indicates Cu was bridging the crack [5].

No face-orientation material was tested because the compression-compression precracking method caused shear failure at the W-Cu interfaces. Edge-orientation fracture was characterized by varying increments of unstable crack growth followed by crack arrest (pop-ins) due to the Cu reinforcement, as illustrated in Figure 1.3.8 from an L+T oriented specimen. A representative fracture surface image of a heat-tinted sample is shown in Figure 3.9 from the same L+T specimen.

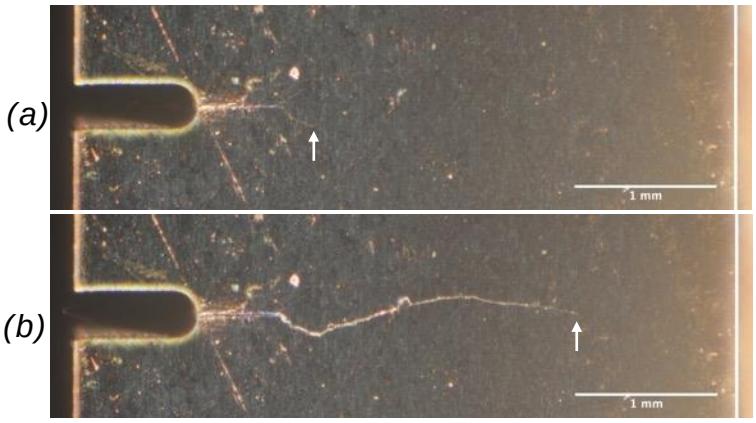

Figure 1.3.8. Comparison of two successive images taken during three-point bend testing on W-Cu laminate (specimen O3-2). a) The crack at a/W = 0.36 grows unstably b) to a/W = 0.76 before being arrested by the Cu reinforcement. Arrows indicate the crack tip in each image, and the vertical line at right indicates the edge of the specimen [6].

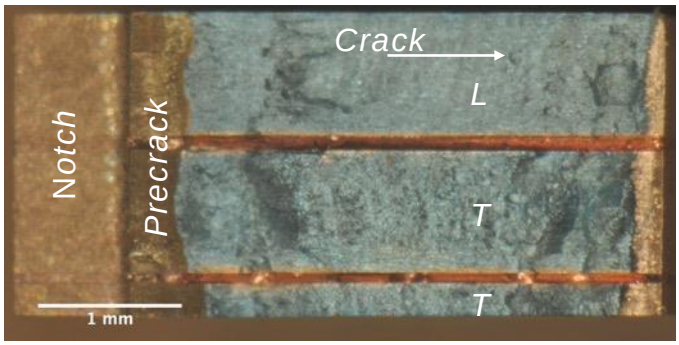

Figure 1.3.9. Fracture surface of W-Cu laminate bend bar (O3-2). Blue coloration on W layers is from heat tinting to observe the final crack length in different W plates. Crack is longer in L-oriented plate than in T plates. Dark contrast in blue test crack region is from surface features; L plate has relatively flat fracture surface while T plates are rough [6].

Precrack fronts had a concave or flat shape instead of the usual convex “thumbnail” shape, and in the mixed orientation the crack propagated to a greater depth in the L-oriented versus T-oriented plates. This is qualitatively consistent with the anisotropic toughness of the W matrix, as the rolled plate is tougher in the T direction than the L direction by a factor of about 1.6.

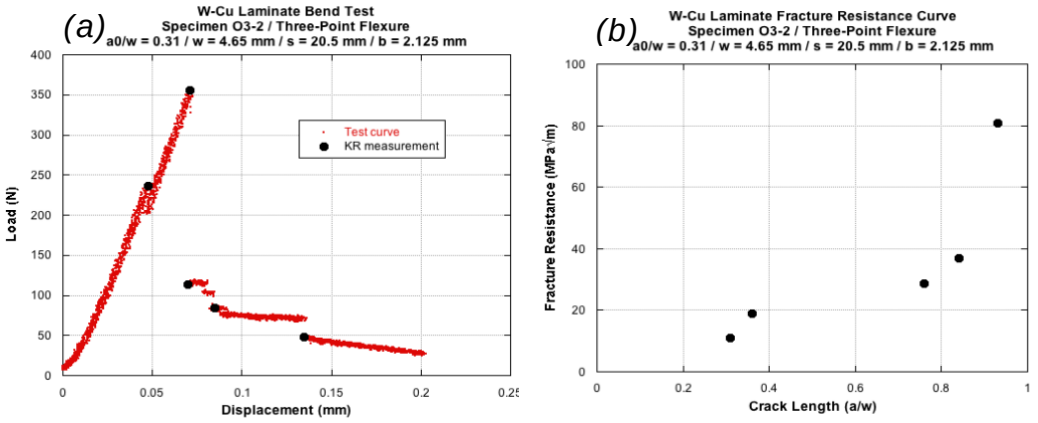

Figure 1.3.10. a) P-D curve, and b) R-curve for W-Cu laminate bend specimen O3-2. Black points on P-D curve indicate the maximum load at each measured crack length used to calculate K_R. Significant load drops were observed corresponding to unstable crack growth and subsequent crack arrest [6].

A representative P-D curve along with the corresponding R-curve is shown in Figure 1.3.10, illustrating the load drops associated with unstable crack growth as well as the loads used to calculate each point in the R-curve. A summary of all calculated R-curves is given in Figure 1.3.11 as a set of plots grouping tests by orientation (L, T, or L+T). The T orientation showed greater increases in toughness with crack extension than the L orientation, but had less stable crack growth.

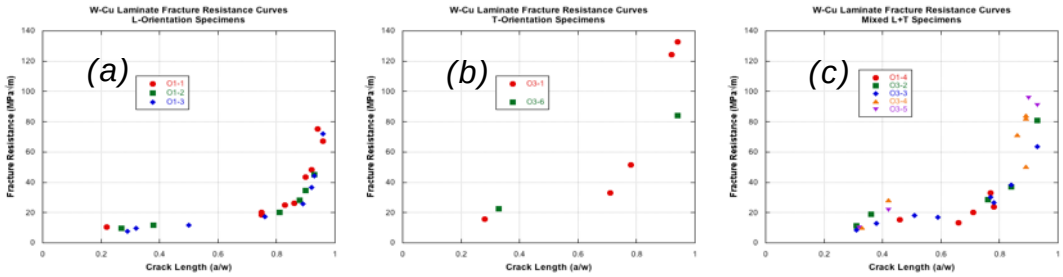

Figure 1.3.11. Comparison of R-curves for W-Cu laminate specimens of different orientations. Plots are grouped by specimens with a) only L-orientation W plates, b) only T-orientation plates, or c) a mix of L and T plates. The T specimens have higher initiation toughness as expected, as well as a greater increase in fracture resistance

with crack growth. The L specimens show more stable crack growth, evidenced by the greater number of points per specimen. In mixed specimens, initiation toughness appears controlled by the L orientation, with the subsequent R-curve shape a mixed character of L and T [6].

For the mixed orientation, in which one of the three W plates was a different orientation than the other two (one L and two T, or vice versa), had a small initial increment of higher R-curve slope than the L orientation, but plateaued around a/W = 0.5, and reached a maximum K_{IR} between those for the L and T orientations at very large a/W. Again, this behavior simply reflects the differences in the T and L matrix toughness. These data do not show a significant difference in R-curve behavior between areas of the laminate containing 2L+1T versus 1L+2T plates.

Since the K_{IR} curves show significant toughness increases only at large a/w, one might conclude that the small amount (< 8% by volume) of relatively weak (annealed Cu) and thin reinforcement had little beneficial effects on the fracture resistance of the composite versus the monolithic W. Indeed, this is the case if the metric is the relative engineering strength of the composite. However, crack arrest and increments of quasi-stable growth are observed, providing some degree of engineering ductility in the composite that is entirely absent in the monolithic W plate. Therefore, a composite with a higher volume fraction of stronger reinforcing phase, with an optimized thickness, would be expected to perform significantly better. To this end, the crack bridging model may guide the fabrication of an improved composite.

1.4. MODELING APPROACH

In parallel with fabrication efforts, a code was developed to model ductile-phase-toughened composites. The code can accommodate any test specimen geometry for which the K_I solution is known, and may be applied to arbitrary composite architectures. The code is adapted from work by Odette and Chao on TiAl-TiNb laminates [23-25, 33].

The two major processes this code performs are: 1) predicting fracture resistance and load-displacement curves (R-curves and P-D curves), and 2) estimating the reinforcement stress-displacement function σ(Δ), the "bridging law." Both cases require input of the specimen geometry and matrix properties. For additional inputs, Case 1 requires the bridging law, and Case 2 requires the calculated R-curve from test data along with the measured failure displacement of the ductile ligaments.

The code was validated first by matching its Case 1 results with those published by Odette and Chao [24]. The Chao code was validated using experimental data, but only its inputs and results were available, not the program itself. The Case 2 results were validated by independently estimating the bridging laws used by the Case 1 code to create R-curves. In this way, the estimate of the bridging law could be compared to the known one.

The form of the bridging law was described with four parameters: the peak load (σ_{max}), the peak-load displacement (Δ_1), a post-peak shape exponent (n), and the failure displacement (Δ_2). A schematic of the bridging law is shown in Figure 1.4.1, and the role of the n parameter in defining the shape of the post-peak curve is described by Equation 1.4.1.

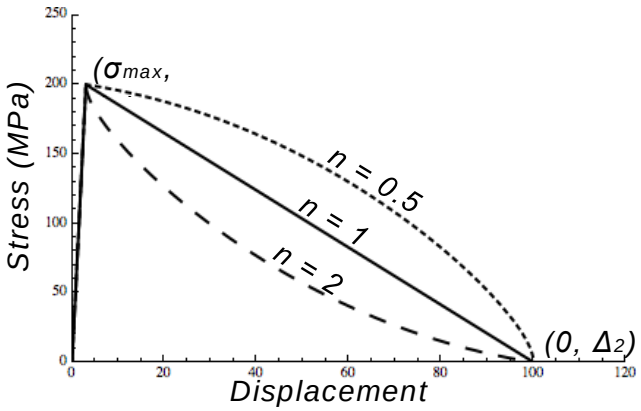

Figure 1.4.1. Example bridging law function. The function is defined by four parameters, and assumes linear elastic behavior approaching the peak load. Examples of the effect of n on the post-peak shape are given [7].

$$\sigma(\Delta) = \frac{\sigma_{max}}{2}\left(1-\frac{\Delta-\Delta_1}{\Delta_2-\Delta_1}\right)^n + \frac{\sigma_{max}}{2}\left(1-\left(\frac{\Delta-\Delta_1}{\Delta_2-\Delta_1}\right)^{1/n}\right),\ \Delta_1 < \Delta < \Delta_2 \qquad [1.4.1]$$

A parametric study was performed by calculating R-curves and P-D curves for a matrix of various values for each bridging law parameter, and are shown in Table 1.4.1.

Table 1.4.1. Values used for each parameter in parametric study. The resulting data set contains 256 associated R-curves and P-D curves to allow for a quantitative comparison of reinforcements for a W-matrix composite [7].

σ_{max} (MPa)	100	200	300	400
Δ_1 (μm)	1	3	5	7
n	0.3	1	3	9
Δ_2 (μm)	50	150	250	350

1.4.1 Analytical Basis

The core mechanic of the program is an iterative calculation that generates a self-consistent solution between the bridging law [σ(Δ)], the opening displacements of the crack [Δ(x)], and the distribution of tractions along the crack face [σ(x)], as shown in Figure 1.4.2.

It is assumed that the matrix crack can be described by linear elastic fracture mechanics, and that the crack is pure Mode I. Using a three-point bend specimen shown in Figure 1.4.3 as an example, relevant solutions are taken from Tada [34] for the stress intensity at the crack tip.

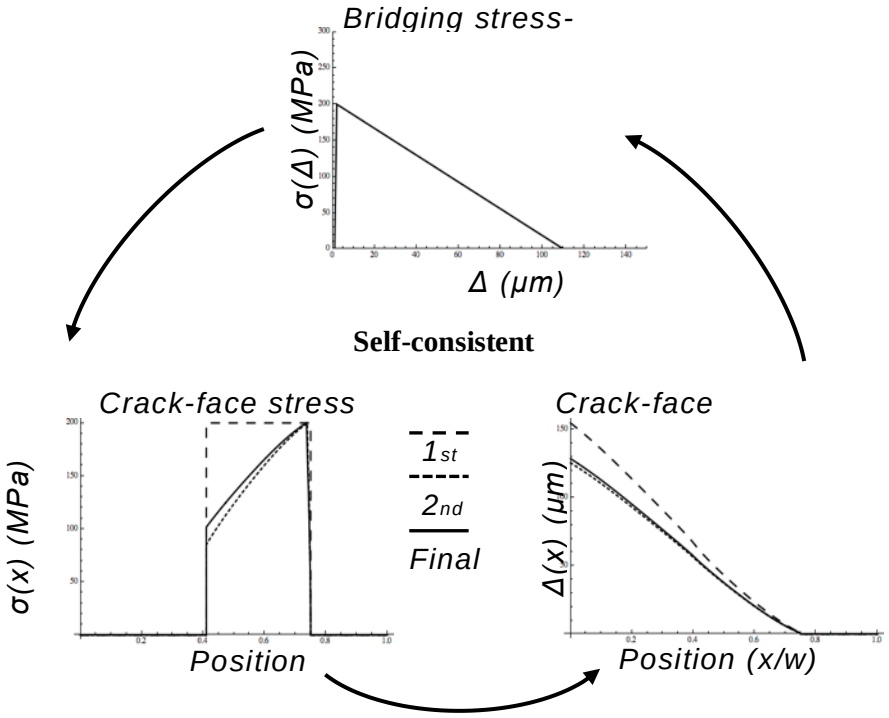

Figure 1.4.2. Visualization of the iterative process at the core of the large-scale bridging model.

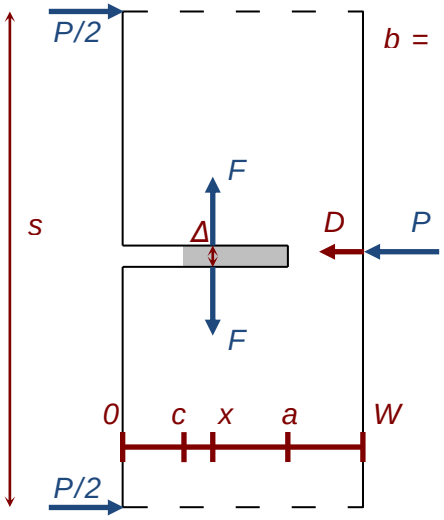

Figure 1.4.3. Schematic of a three-point bend specimen illustrating relevant dimensions (red) and stresses (blue). The shaded gray area represents the portion of the crack bridged by a reinforcing phase. The stresses are: the applied stress (P) and a point stress (F) at position x on the crack face. The displacements are: the crack-

face displacement (Δ) at point x, and the engineering load-point displacement (D). In the x-direction, the bridging zone runs from c to the crack length a. The specimen width is w, the test span is s, and the specimen thickness (out-of-page) is b [6].

$$K_{I,P}(P,a) = \frac{3\,P\,s}{2\,w^2}\sqrt{\pi a}\,F_1\left(\frac{a}{w}\right) \qquad [1.4.2]$$

$$K_{I,F}(F,x,a) = \frac{2\,F}{\sqrt{\pi a}}\,F_2\left(\frac{x}{a},\frac{a}{w}\right) \qquad [1.4.3]$$

$K_{I,P}$ is due to the applied stress P, and $K_{I,F}$ is due to a point stress F at position x on the crack face. The functions F_1 and F_2 are shown in the appendix. The effective stress intensity at the crack tip is the applied stress intensity minus the reduction in stress intensity due to the bridging stress distribution, $K_{I,eff} = K_{I,P} - \Delta K_{I,F}$. The principle of superposition is used to treat the bridging zone tractions as a series of point forces along the crack face, and $\Delta K_{I,F}$ is found by integrating over the bridging zone.

$$\Delta K_{I,F} = \int_0^a K_{I,F}[\sigma(x),x,a]\,dx \qquad [1.4.4]$$

The applied stress intensity reaches its critical value, the composite fracture resistance, ($K_{I,P} = K_{IR}$) when the effective stress intensity at the crack tip is equal to the matrix toughness ($K_{I,eff} = K_{IC}$), thus

$$K_{IR} = \Delta K_{I,F} + K_{IC}. \qquad [1.4.5]$$

Once the fracture resistance has been calculated, Castigliano's Theorem is applied to calculate the shape of the crack. Castigliano's Theorem states that the displacement due to a force Q in the direction of that force is equal to the partial differential of the total strain energy with respect to that force [34].

$$\Delta_Q = \frac{\partial U_T}{\partial Q} \qquad [1.4.6]$$

The strain energy may be separated into two components: the strain energy of the uncracked body, and the additional energy due to introducing the crack while holding the forces constant [34]:

$$U_T = U_{nc} + \int_0^A \frac{\partial U_T}{\partial A} dA. \qquad [1.4.7]$$

Substitute into Castigliano's Theorem to derive the displacements of the uncracked and cracked bodies, where the uncracked displacement is identically zero at the crack face. Also, substitute the energy release rate G_I for $\frac{\partial U_T}{\partial A}$ [34].

$$\Delta_Q = \frac{\partial U_{nc}}{\partial Q} + \frac{\partial}{\partial Q}\int_0^A G_I dA = \frac{\partial}{\partial Q}\int_0^A G_I dA \qquad [1.4.8]$$

From Irwin's relationship, and assuming a Mode I crack [34],

$$E' G_I = {K_I}^2 = \left(K_{I,P} + K_{I,F}\right)^2. \qquad [1.4.9]$$

Combining Equations 1.4.8 and 1.4.9 and allowing the virtual forces to approach zero, solutions are found for the opening and closing displacements, Δ_P and Δ_F. The net displacement Δ is the difference between the two [33].

$$\Delta_P(x) = \frac{2}{E'}\int_x^a K_{IP}(P, a') \frac{\partial K_{IF}(F,x,a')}{\partial F} da' \qquad [1.4.10]$$

$$\Delta_F(x) = \frac{2}{E'}\int_x^a \left[\int_0^{a'} K_{IF}(\sigma(x'), x', a') dx'\right] \frac{\partial K_{IF}(F,x,a')}{\partial F} da' \qquad [1.4.11]$$

$$\Delta(x) = \Delta_P(x) - \Delta_F(x) \qquad [1.4.12]$$

In both cases, the integrand consists of the stress intensity due to the opening or closing tractions at the instantaneous crack length a', multiplied by the partial derivative of the crack-face $K_{I,F}$ with respect to F. In the calculation of Δ_F, the stress intensity due to the bridging tractions at an instantaneous crack length a' is itself an integrated quantity, similar to $\Delta K_{I,F}$.

Finally, the load-point displacement is calculated as the elastic solution minus the contribution from the bridging zone. The former is given by Timoshenko and Tada, and the latter follows the above derivation applied to the case of displacements in the direction of P. The resulting solutions for the reduction in displacement due to the bridging zone (D_F), and the net displacement (D) are [33-34]

$$D_F = \frac{2}{E'}\int_0^a \left[\int_0^{a'} K_{IF}(x,a')dx\right]\frac{\partial K_{IP}(a')}{\partial P}da' \qquad [1.4.13]$$

$$D = P\left(\frac{s^3}{4E'w^3} + \frac{s}{2w}\left(\frac{3}{4G} - \frac{3}{10E'} - \frac{3\nu}{4E'}\right) - \frac{0.21}{E'}\right) + \frac{3Ps^2}{2E'w^2}V_2\left(\frac{a}{w}\right) - D_F \qquad [1.4.14]$$

where the function V_2 is defined in the appendix.

1.4.2 Procedural Structure

1.4.2.1 Determination of R-Curves and P-D Curves

Input data. Enter the specimen dimensions (width, span, thickness, precrack depth), matrix properties (Young's modulus, Poisson's ratio, fracture toughness), and bridging law (can be defined as any continuous function). A shape function may be used to define any discontinuities the crack front would encounter while propagating through the material (such as with a face-orientation laminate specimen). Specify the calculation parameters – crack growth step size and convergence criteria [σ(x) and bridging zone length].

Define functions. Set up functions that will be called often in the code, and create variable arrays that will be used to track the solutions for each step of the calculation.

Calculate the applied load needed to advance the crack. Start by growing the crack from its initial depth to the next increment, and assume that region to be the current bridging zone. Assume a constant stress over the bridging zone and calculate $\Delta K_{I,F}$ from that $\sigma(x)$. Then calculate K_{IR} and use the form of $K_{I,P}$ to find P.

Calculate the shape of the crack. Define a mesh of points on the crack face. Calculate the opening, closing, and net crack-face displacement at each point.

Update the bridging traction guess. Use the bridging law to calculate the stress corresponding to each crack-face displacement and interpolate over the mesh to update the guessed bridging stress distribution. Calculate the difference between the two stress distributions by taking the sum of the absolute difference at each point in the mesh. If the error is below the convergence criterion, accept the solution; otherwise, repeat the calculation with the updated $\sigma(x)$. After checking the convergence of the stress distribution, check the convergence of the bridging zone length. Repeat if the change in bridging zone size does not satisfy the convergence criterion. Once all calculations have converged, continue to the next crack length. Stop before the virtual crack grows past the width of the specimen.

Calculate the load-point displacements. Recall the $\sigma(x)$ and other solutions from the first iteration of crack length extension. Calculate the elastic load-point displacement for that crack length and the reduction in displacement due to the bridging zone. Repeat for each value of crack length.

When the algorithm has finished running, the solutions for $\sigma(x)$, $\Delta(x)$, K_{IR}, P, and D are all stored in arrays according to which crack length they correspond to. The evolution of each parameter

may be visualized graphically, and of course the R-curve and P-D curve may be plotted. R-curves are plotted as K_{IR} in MPa vs. normalized crack length (a/w). P-D curves are plotted as P/P' vs. D/D', where P' and D' are the elastic failure load and displacement of a pure-matrix specimen of the same geometry.

1.4.2.2 Determination of Bridging Law

Input data. Specify the same inputs as above with the following exceptions. Enter the R-curve data. Enter the bridging law parameters. As the parameters are not known except for the failure displacement Δ_2, enter initial guess values for σ_{max}, Δ_1, and n. The guess for Δ_1 should be small for the prediction to be most accurate. Define a step size for guesses in Δ_1, convergence criteria for the calculation of σ_{max} and n, and a gain value to help the n solution converge in fewer iterations. Store the R-curve as an interpolated function. A step size for crack growth is not necessary for this calculation.

Define functions. The set of functions to call during the calculation is the same. The set of empty lists is also the same with the addition of lists to hold the solutions for σ_{max}, Δ_1, and n after each iteration.

Estimate Δ_1 and σ_{max} simultaneously. Model a short crack extension ($a - a_0$). Use the elastic near-tip crack shape solution to solve for this crack length from a given Δ_1 [34].

$$\Delta = \frac{4\sqrt{2}}{\sqrt{\pi}E'} K_{IC}\sqrt{a - a_0} \quad \rightarrow \quad a = a_0 + \left(\frac{\Delta_1\sqrt{\pi}E'}{4K_{IC}\sqrt{2}}\right)^2 \qquad [1.4.15]$$

This method ensures that at no point in the bridging zone will $\Delta(x) > \Delta_1$; thus, the activated region of the bridging law will always be within the guessed elastic region and the post-peak shape has no effect. Use the guess value for σ_{max} as the constant-stress $\sigma(x)$ guess.

Proceed with the calculation of $\Delta K_{I,F}$ as in Case 1. Then use the known K_{IR} value for this crack length (from the interpolation of the R-curve data) to calculate the true $\Delta K_{I,F}$. Scale the guessed $\sigma(x)$ distribution as well as the σ_{max} guess by the ratio of the true $\Delta K_{I,F}$ to the initial guess, ensuring that the calculated K_{IR} value is correct, and proceed using the scaled $\sigma(x)$. Proceed as in Case 1 to calculate the crack shape and update the stress distribution, and then repeat the process until the change in the estimated σ_{max} satisfies the convergence criterion.

Accept this estimate of σ_{max} for the given crack length, then increase by one step in Δ_1, recalculate the corresponding crack length, and repeat to estimate a series of (Δ_1,σ_{max}) points. The resulting set of estimates looks like an approximation to the elastic portion of the bridging law. Stop increasing Δ_1 once the convergent σ_{max} value is lower than that for the previous Δ_1 step. Finally, choose from these points the best estimate of (Δ_1, σ_{max}).

Figure 1.4.4 explains the best-estimate selection process graphically. The current strategy is to find the point at which the estimated (Δ_1, σ_{max}) curve deviates from linearity. To do this, fit a series of linear regressions to the data, removing the last point with each successive fit (start with the blue fit in Fig. 1.4.4a). Analyze the list of goodness-of-fit values (R_2) from each linear regression to find the index of first local maximum (red circle in Fig. 1.4.4b). This index corresponds to the best estimate of Δ_1 and σ_{max} (red circle in Fig. 1.4.4a).

Estimate the post-peak shape parameter. At this point, the other three parameters are known and only the guess value for n remains. Calculate an R-curve using the current bridging law guess. In calculating the R-curve, use the same crack length values as those measured in the true R-curve data. Integrate each R-curve with respect to crack length and compare the respective area under each curve. Update the guess value for n,

$$n_i = n_{i-1}\left[\frac{\int K_{IR,guess}(a)\,da}{\int K_{IR,true}(a)\,da}\right]^z, \qquad [1.4.16]$$

where z is a gain exponent that accelerates convergence. Continue iterating until the change in n satisfies the convergence criterion.

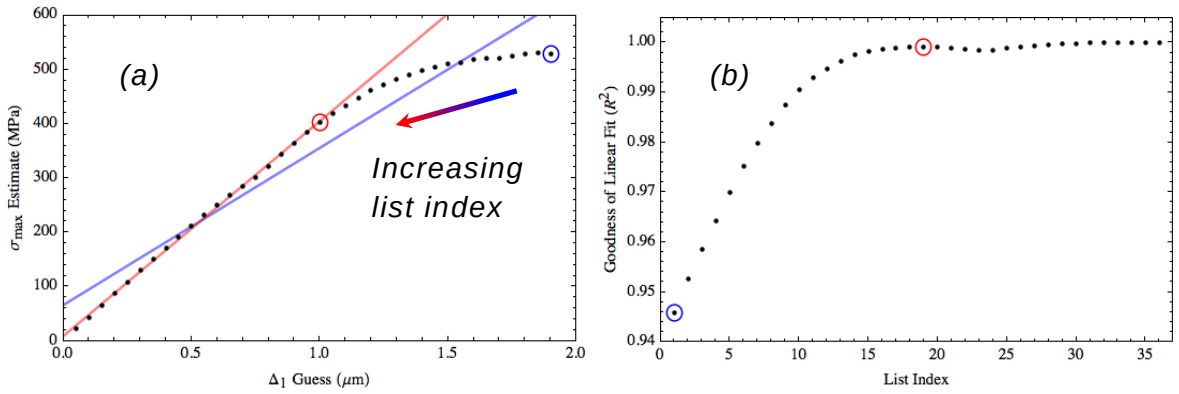

Figure 1.4.4. a) Plot of estimated (Δ_1, σ_{max}) points showing the first (blue) and the best-guess (red) linear fits. Colored circles around points indicate the highest Δ_1 value used in the corresponding fit. The best-guess (Δ_1, σ_{max}) point (red circle) is taken as the final estimate for the two parameters. b) Plot of goodness-of-fit value (R_2) for each linear regression vs. the list index as shown in Fig. 1.4.4a. Blue and red circles indicate the R_2 values corresponding to the fits shown in Fig. 1.4.4a. The best guess is selected by finding the first local maximum in R_2 (red circle).

1.5. MODEL RESULTS

1.5.1 Determination of R-Curves and P-D Curves

The large-scale crack bridging code results were compared the previous work of Odette and Chao [24], since that work was validated experimentally. Figure 1.5.1 shows resistance curves and load-displacement curves calculated for three different bridging stress-displacement functions, indicated by color. The new resistance curve calculations (points) compare very well with the previous results (lines) but the P-D predictions are only consistent up to nearly the peak

load. After the peak load, the load-point displacement is under-predicted with respect to the previous results. The calculation converges quickly when modeling specimens in the edge orientation because the reinforcement is continuous in the direction of crack propagation. Additional meshing steps are required for accurate face-orientation modeling.

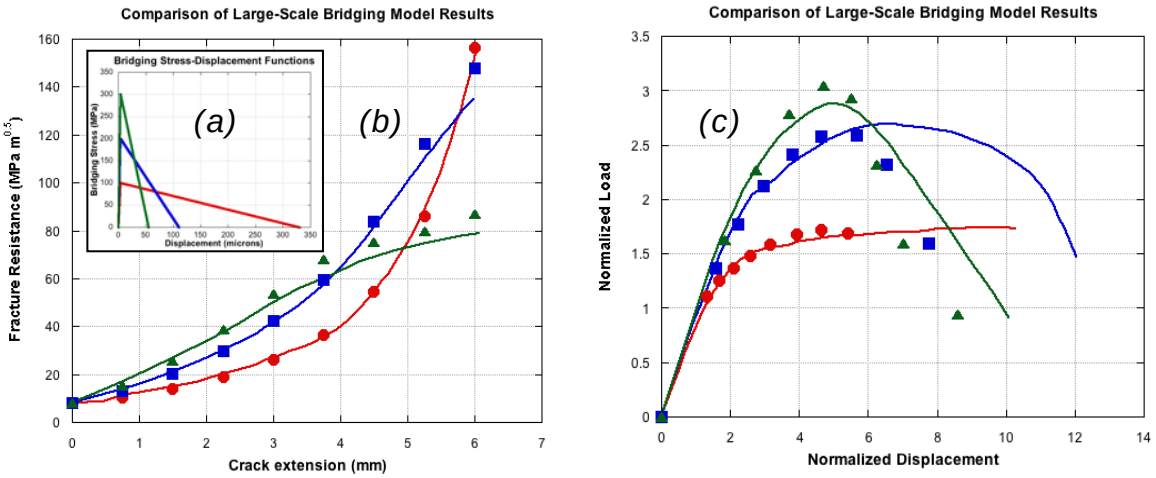

Figure 1.5.1. Experimentally-verified models (lines) compared with current models (points) for identical initial conditions, modeling a TiAl-TiNb laminate. a) Bridging law functions corresponding to the colors in each plot. b) Comparison of resistance curves. c) Comparison of load-displacement curves. Values are normalized by the load capacity and displacement at fracture of a non-reinforced test specimen [5, 24].

1.5.2 Determination of Bridging Law

It is generally not possible to directly measure σ(Δ) curves for embedded reinforcements since this depends on details like debonding and triaxial stresses in matrix cracks that are blunted in the ductile phase. However, as noted above they can be inversely extracted from test data. The estimation strategy for σ_{max} and Δ_1 successfully reconstructed the elastic loading portion of the bridging law as shown in Figure 5.2a. The estimate for n also converges near enough to the true value (Fig. 1.5.2b) that the R-curve fits well with the input data (Fig. 1.5.2c).

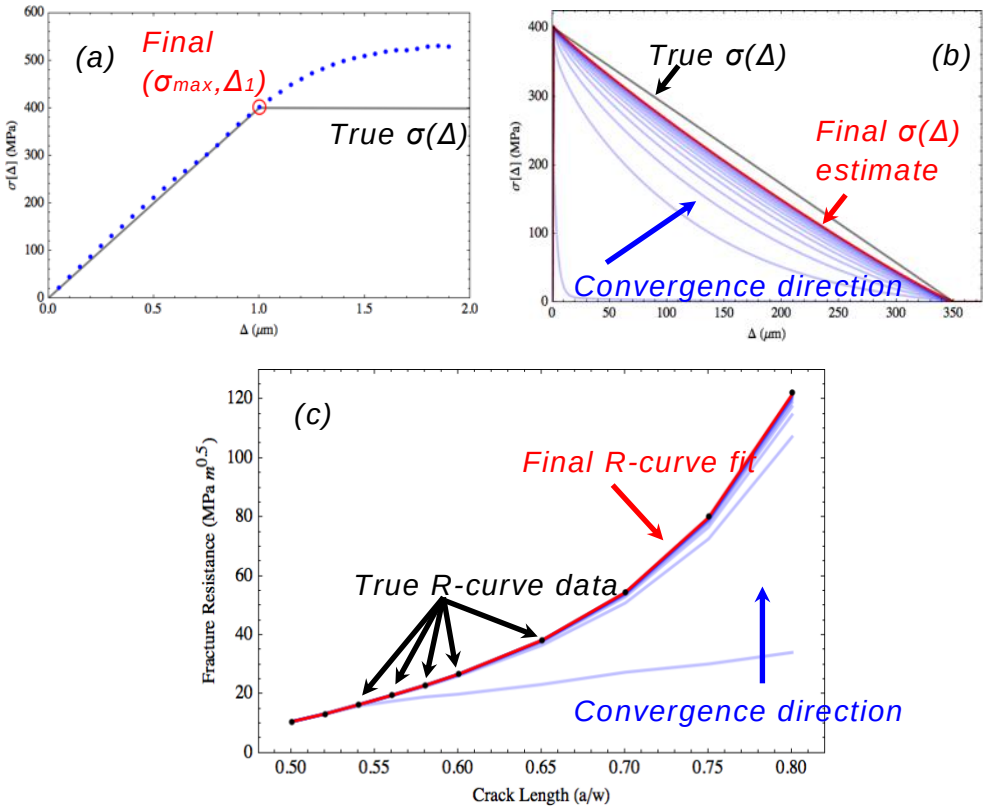

Figure 1.5.2. a) Estimate of (σ_{max},Δ_1) point (red circle) shown against a close-up view of the true bridging law (gray curve). Calculated values (points) track well with the elastic slope of the bridging law. b) Estimate of n parameter shown as a series of calculated bridging laws (blue curves), highlighting final estimate (red curve). Compare to the true bridging law (gray curve). c) Black points show the true R-curve. Blue curves show successive iterations during estimation of n, and red curve corresponds to the final bridging law estimate.

1.5.3 Parametric Study

A parametric study of reinforcement σ(Δ) was used to evaluate the effects of the controlling parameters individually and in combination as illustrated in Figure 1.5.3. Here the P-D curves are normalized by the corresponding loads and displacements at elastic fracture of the brittle matrix, P' and D', respectively.

σ_{max} [MPa]	Δ_1 [μm]	n -	Δ_2 [μm]	P-D Curves [P/P' vs. D/D']	R-Curves [K_{IR} (MPa) vs. a/w]
100 200 300 400	1	0.3	350	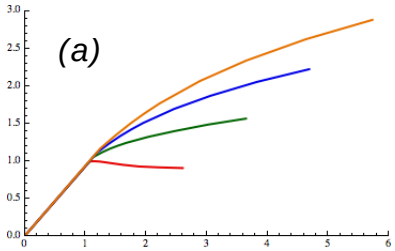	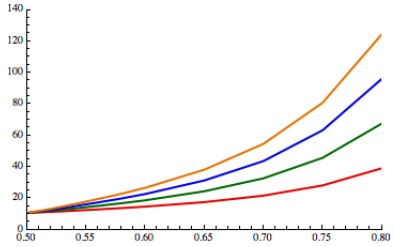
400	1 3 5 7	0.3	350	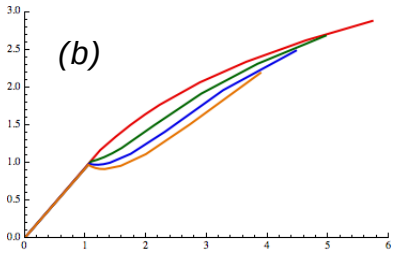	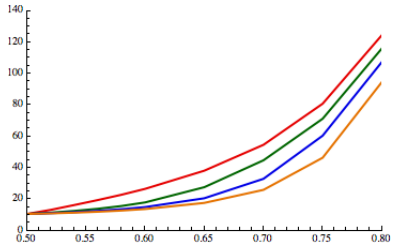
400	1	0.3 1 3 9	350	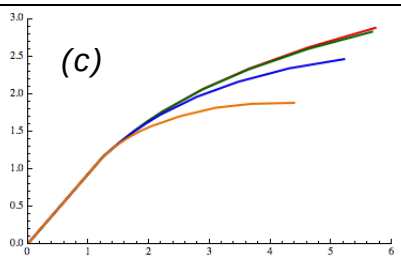	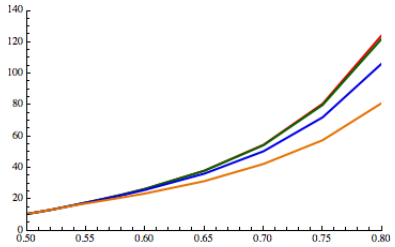
400	1	9	50 150 250 350	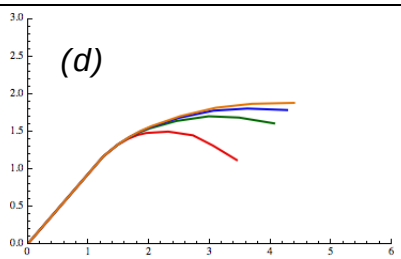	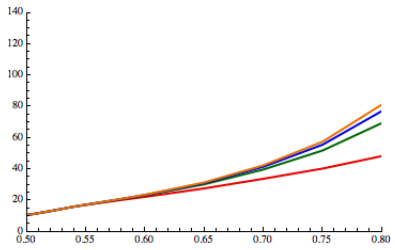

Figure 5.3. Parametric study summary. In each row of values and plots, one parameter is varied and the resulting P-D curves and R-curves are shown. Load and displacement values are normalized by the load capacity (P') and displacement (D') at fracture, respectively, of the unreinforced tungsten matrix. The mechanical behavior of the composite is more sensitive to σ_{max} and u_1 than to n and u_2 [6].

For a desirable, and expected, low value of Δ_1, the P-D and $K_{IR}(a/w)$ curves increase with increasing σ_{max}, resulting in a desirable increase in P_{max}, accompanied by increasing D or ductility (Fig. 1.5.3a). The detrimental effect of increasing Δ_1 is also revealed in the P-D curves (Fig. 1.5.3b). Both increasing the convex shape of the bridging law (Fig. 1.5.3c) and, to a lesser extent, increasing Δ_2 (Fig. 1.5.3d) increase the composite strength and ductility.

It must be emphasized that while these effects can be qualitatively anticipated, they all represent large-scale bridging effects for a growing bridging zone that cannot be quantitatively predicted based on intuition or simple energy-based concepts. The engineering performance capabilities of a DPT composite are reflected in the normalized P-D curves with values of P/P' and D/D' greater than 1, which is the limit for the elastically brittle monolithic matrix material. It is also worth noting that it is the initial slope of the R-curve that controls the crack growth initiation P-D and any subsequent stable crack growth for any expected practical initial crack length.

1.6. DISCUSSION AND CONCLUSIONS

The goal of this work was to demonstrate ductile-phase toughening in a tungsten composite. Early work to develop composites with spark plasma sintering or hot-pressing fabrication routes were unsuccessful in terms of enabling stable crack growth through crack bridging; however, a brazed W-Cu laminate demonstrated these properties in fracture testing. A large-scale crack bridging model was developed to predict mechanical properties of an arbitrary composite or its reinforcing phase.

The EBSD data collected to analyze the microstructure evolution in W wire during processing is limited but may indicate the beginning of recrystallization at high temperature of the highly-deformed wire. The extrinsic toughening at installation of a DPT W composite will indeed come from a ductile reinforcement, but more investigation is required to understand whether these

reinforcements will continue to provide such toughening by the end of the material's service life. The dominant mechanism may shift from deformation of the reinforcement to frictional sliding during pull-out, for example.

The toughness of the W plates is higher than the expected value for the as-sintered material, due to severe plastic deformation during the rolling process. However, considering the large-scale material demand for a fusion reactor, such processed forms of W should not be relied upon for composite research without a thorough investigation of the economics of scale for such processes. Generally speaking, the simplest processing route to a toughened composite should be pursued.

Sintering of W powders in this study resulted in greater than 95% densification. A 2-temperature sintering route to consolidate W around Cu-coated W wires is unlikely to be effective unless full matrix densification occurs at the low temperature. The pulsed current capabilities of the SPS have not been explored here, but may be useful in this effort.

Besides tungsten, carbon is the most favorable element for high-temperature use in a divertor application. The previous plan for ITER was to begin operation using a divertor with both carbon-carbon composite and W armor components before switching to full W – this plan was changed in favor of using only W from the beginning due to cost concerns. It must be noted that a fully carbon divertor gives rise to significant tritium retention issues, so minimizing the fraction of carbon in a W-composite debonding layer is a key concern [35]. In this study, tungsten carbide as an interface layer was too strongly bonded to the matrix to give rise to any crack bridging. Fugitive interfaces are a possible design choice in this case, where porosity is introduced at the interface [36]. This utility in aiding debonding must be balanced with thermal conductivity needs.

The complexity of the hot-pressed laminate material may not be amenable to large-scale processing. The general concept of embedding W wires in a W matrix, however, is still an intriguing one. Some evidence of fiber pullout was observed in tests on the hot-pressed laminate, and the embedded “sandwich” reinforcement was able to arrest the crack. A finer-scale laminate may allow for greater stable crack growth normal to the layers. Additionally, controlled precracking is vital for R-curve testing on W composites.

Ductile-phase toughening has been demonstrated for W plates brazed with Cu. Stronger reinforcements are needed to give an increased engineering strength, but even a weak reinforcement enabled crack arrest and significant ductility. While Cu is useful for developing model composites, it is not a viable choice for PFCs [26]. Further development should focus on acceptable elements.

The large-scale bridging model is a powerful tool for composite design and analysis. While in this study the possible composite architectures were constrained by available equipment, future fabrication efforts may choose processes better suited to working with, for example, larger and more ordered layups of coated W fibers. A parametric study of reinforcement bridging laws applied to a matrix of interest can guide the initial selection of reinforcement material and the required volume fraction of reinforcement. After preliminary R-curve testing, the actual bridging law for the new material may be derived using the model and then used to refine the composite design.

The calculation of R-curves is robust, but displacement calculations are too conservative in comparison to the previous model. The reduction in load-point displacement due to the bridging zone is calculated to be greater in the current code than in the previous one. This discrepancy may arise from a difference in the integration strategies used by each code. The algorithm for determining bridging laws is robust in its estimate of σ_{max} and Δ_1, and while errors remain in the

estimation of n, the calculated R-curve is not sensitive to this error. An improved code would include a more adaptive convergence algorithm for determining n, as well as estimation strategies for Δ_2 and potentially the residual stress.

1.7. RECOMMENDATIONS FOR FUTURE WORK

Development of W-composite PFCs must be guided by the evolving thermal and mechanical requirements for divertor components. Broadly, the three aspects of W-composite PFC development are the choice of reinforcement material and architecture, optimization of the fabrication route, and control of in-service microstructure evolution.

Efforts should be made to develop scalable fabrication routes for near-net-shape W-composite parts by pairing rapid consolidation techniques like SPS with fiber layup tools and green body forming techniques like powder-injection molding [12, 37]. Sintering around a preform can result in matrix cracking to relieve stress during consolidation, but this process could be useful for extrinsic toughening if a weak interface layer was designed to crack instead of the matrix [38]. The utility of a composite for large-scale application depends strongly on economy of fabrication, so it is helpful to design materials with this in mind. The availability of W product forms (wire, foil, plate, etc.) for large-scale composite fabrication should also be considered. For composite layups there is a need for appropriate tooling, such as near-net-shape sintering dies and fiber alignment tools.

Structural tungsten components remain a critical research need for the future of fusion energy. The next steps in developing DPT tungsten should involve choosing reinforcements that are compatible with the divertor environment. Low-activation elements include Fe, Cr, V, Ti, Si, and C [26]. Experimentation and modeling should proceed together in an iterative design process.

REFERENCES

[1] C. H. Henager, R. J. Kurtz, G. R. Odette, and F. W. Zok, “Ductile-phase toughened and fiber-reinforced tungsten for plasma facing materials,” Proposal to the U.S. Department of Energy Office of Science, Fusion Energy Sciences. Materials solicitation with focus on structural materials, blanket first walls, and divertor plasma facing components, 2011.

[2] K. H. Cunningham, K. Fields, D. Gragg, F. W. Zok, C. H. Henager, Jr., R. J. Kurtz, and T. Roosendaal, “Recent progress in the development of ductile-phase-toughened tungsten for plasma-facing materials,” in DOE/ER-0313/54 - Volume 54, Semiannual Progress Report, June 30, 2013. 2013, US DOE: ORNL, TN.

[3] C. H. Henager, Jr., R. J. Kurtz, T. J. Roosendaal, B. A. Borlaug, G. R. Odette, K. H. Cunningham, K. Fields, D. Gragg, and F. W. Zok, “Recent progress in the development of ductile-phase-toughened tungsten for plasma-facing materials,” in DOE/ER-0313/55 - Volume 55, Semiannual Progress Report, Dec. 31, 2013. 2013, US DOE: ORNL, TN.

[4] K. H. Cunningham, G. R. Odette, K. Fields, D. Gragg, F. W. Zok, C. H. Henager, Jr., R. J. Kurtz, T. J. Roosendaal, and B. A. Borlaug, “Recent progress in the fabrication and characterization of ductile-phase-toughened tungsten composites for plasma-facing materials,” in DOE/ER-0313/56 - Volume 56, Semiannual Progress Report, Jun. 30, 2014. 2014, US DOE: ORNL, TN.

[5] K. H. Cunningham, G. R. Odette, K. Fields, D. Gragg, T. Yamamoto, F. W. Zok, C. H. Henager, Jr., R. J. Kurtz, T. J. Roosendaal, and B. A. Borlaug, “Recent progress in the fabrication and characterization of ductile-phase-toughened tungsten laminates for plasma-facing materials,” in DOE/ER-0313/57 - Volume 57, Semiannual Progress Report, Dec. 31, 2014. 2014, US DOE: ORNL, TN.

[6] K. H. Cunningham, G. R. Odette, K. Fields, D. Gragg, T. Yamamoto, and F. W. Zok, “Recent progress in the fabrication and characterization of ductile-phase-toughened tungsten laminates for plasma-facing materials,” in DOE/ER-0313/58 - Volume 58, Semiannual Progress Report, Jun. 30, 2015. 2015, US DOE: ORNL, TN.

[7] M. Rieth, J. L. Boutard, S. L. Dudarev, T. Ahlgren, S. Antusch, N. Baluc, M. F. Barthe, C. S. Becquart, L. Ciupinski, J. B. Correia, C. Domain, J. Fikar, E. Fortuna, C. C. Fu, E.

Gaganidze, T. L. Galán, C. García-Rosales, B. Gludovatz, H. Greuner, K. Heinola, N. Holstein, N. Juslin, F. Koch, W. Krauss, K. J. Kurzydlowski, J. Linke, C. Linsmeier, N. Luzginova, H. Maier, M.S. Martínez, J. M. Missiaen, M. Muhammed, A. Muñoz, M. Muzyk, K. Nordlund, D. Nguyen-Manh, P. Norajitra, J. Opschoor, G. Pintsuk, R. Pippan, G. Ritz, L. Romaner, D. Rupp, R. Schaublin, J. Schlosser, I. Uytdenhouwen, J. G. Van Der Laan, L. Veleva, L. Ventelon, S. Wahlberg, F. Willaime, S. Wurster, and M. A. Yar, "Review on the EFDA programme on tungsten materials technology and science," *Journal of Nuclear Materials* **417**, 463-467 (2011).

[8] R. A. Pitts, A. Kukushkin, A. Loarte, A. Martin, M. Merola, C. E. Kessel, V. Komarov, and M. Shimada, "Status and physics basis of the ITER divertor," *Physica Scripta* **T138**, 014001 (2009).

[9] P. Mertens, T. Hirai, M. Knaup, O. Neubauer, V. Philipps, J. Rapp, V. Riccardo, S. Sadakov, B. Schweer, A. Terra, I. Uytdenhouwen, and U. Samm, "A bulk tungsten divertor row for the outer strike point in JET," *Fusion Engineering and Design* **84**(7-11), 1289-93 (2009).

[10] A. Gervash, R. Giniyatulin, T. Ihli, W. Krauss, A. Makhankov, I. Mazul, P. Norajitra, and N. Yablokov, "Fabrication of a He-cooled divertor module for DEMO reactor," *Journal of Nuclear Materials* **367-370**, 1472-1475 (2007).

[11] M. Merola, W. Danner, and M. Pick, "EU R&D on divertor components," *Fusion Engineering and Design* **75-79**, 325-331 (2005).

[12] M. Merola, F. Escourbiac, A. R. Raffray, P. Chappuis, T. Hirai, S. Gicquel, the ITER Blanket and Divertor Sections procuring Domestic Agencies, and the Blanket Integrated Product Team, "Engineering challenges and development of the ITER Blanket System and Divertor," *Fusion Engineering and Design* (2015), DOI: 10.1016/j.fusengdes.2015.06.045.

[13] M. Rieth, S. L. Dudarev, S. M. Gonzalez de Vicente, J. Aktaa, T. Ahlgren, S. Antusch, D. E. J. Armstrong, M. Balden, N. Baluc, M.-F. Barthe, W. W. Basuki, M. Battabyal, C. S. Becquart, D. Blagoeva, H. Boldyryeva, J. Brinkmann, M. Celino, L. Ciupinski, J.B. Correiam, A. De Backer, C. Domain, E. Gaganidze, C. García-Rosales, J. Gibson, M.R.

Gilbert, S. Giusepponi, B. Gludovatz, H. Greuner, K. Heinola, T. Höschen, A. Hoffmann, N. Holstein, F. Koch, W. Krauss, H. Li, S. Lindig, J. Linke, Ch. Linsmeier, P. López-Ruiz, H. Maier, J. Matejicek, T.P. Mishra, M. Muhammedl, A. Muñoz, M. Muzyk, K. Nordlund, D. Nguyen-Manh, J. Opschoor, N. Ordás, T. Palacios, G. Pintsuk, R. Pippan, J. Reiser, J. Riesch, S.G. Roberts, L. Romaner, M. Rosiński, M. Sanchez, W. Schulmeyer, H. Traxler, A. Ureña, J.G. van der Laan, L. Veleva, S. Wahlberg, M. Walter, T. Weber, T. Weitkamp, S. Wurster, M.A. Yar, J.H. You, and A. Zivelonghi, "Recent progress in research on tungsten materials for nuclear fusion applications in Europe," *Journal of Nuclear Materials* **432**, 482-500 (2013).

[14] P. Mertens, V. Philipps, G. Pintsuk, V. Riccardo, U. Samm, V. Thompson, and I. Uytdenhouwen, "Clamping of solid tungsten components for the bulk W divertor row in JET-precautionary design for a brittle material," *Physica Scripta* **T138**, 014032 (2009).

[15] B. Gludovatz, S. Wurster, A. Hoffmann, and R. Pippan, "Fracture toughness of polycrystalline tungsten alloys," *International Journal of Refractory Metals and Hard Materials* **28**(6), 674-8 (2010).

[16] S. J. Zinkle and N. M. Ghoniem, "Operating temperature windows for fusion reactor structural materials," *Fusion Engineering and Design* **51-52**, 55-71 (2000).

[17] M. Faleschini, H. Kreuzer, D. Kiener, and R. Pippan, "Fracture toughness investigations of tungsten alloys and SPD tungsten alloys," *Journal of Nuclear Materials* **367-370**, 800-805 (2007).

[18] T. Tanno, A. Hasegawa, J. C. He, M. Fujiwara, M. Satou, S. Nogami, K. Abe, and T. Shishido, "Effects of transmutation elements on the microstructural evolution and electrical resistivity of neutron-irradiated tungsten," *Journal of Nuclear Materials* **386-388**, 218-221 (2009).

[19] T. Tanno, A. Hasegawa, M. Fujiwara, H. Jian-Chao, S. Nogami, M. Satou, T. Shishido, and K. Abe, "Precipitation of solid transmutation elements in irradiated tungsten alloys," *Materials Transactions* **49**(10), 2259-64 (2008).

[20] T. Tanno, A. Hasegawa, H. Jian-Chao, M. Fujiwara, S. Nogami, M. Satou, T. Shishido, and K. Abe, “Effects of transmutation elements on neutron irradiation hardening of tungsten,” *Materials Transactions* **48**(9), 2399-402 (2007).

[21] J. Riesch, T. Höschen, C. Linsmeier, S. Wurster, and J.-H. You, “Enhanced toughness and stable crack propagation in a novel tungsten fibre-reinforced tungsten composite produced by chemical vapour infiltration,” *Physica Scripta* **T159**, 014031 (2014).

[22] P. R. Subramanian and D. E. Laughlin, “Cu-W (Copper-Tungsten),” in monograph, “Phase diagrams of binary tungsten alloys,” ed. S. V. N. Naidu and P. R. Rao, Indian Institute of Metals, Calcutta, 76-79 (1991).

[23] R. Venkateswara, G. R. Odette, and R. O. Ritchie, “Ductile-reinforcement toughening in TiAl intermetallic-matrix composites: Effects on fracture toughness and fatigue-crack propagation resistance,” *Acta Metallurgica et Materialia* **42**(3), 893-911 (1994).

[24] G. R. Odette, B. L. Chao, J. W. Sheckherd, and G. E. Lucas, “Ductile phase toughening mechanisms in a TiAl-TiNb laminate composite,” *Acta Metallurgica et Materialia* **40**(9), 2381-9 (1992).

[25] J. A. Heathcote, “The fracture behavior of intermetallic/metallic microlaminate composites,” Ph.D. Dissertation, University of California, Santa Barbara, 1996.

[26] N. Baluc, “Material degradation under DEMO relevant neutron fluences,” *Physica Scripta* **T138**, 014004 (2009).

[27] I. Charit, D. P. Butt, M. Frary, and M. C. Carroll, “Fabrication of tungsten-rhenium cladding materials via spark plasma sintering for ultra high temperature reactor applications,” U.S. Department of Energy (FY2009 NE-UP Program), 10/1/2009 to 9/30/2012.

[28] K. Williams and R. S. Muller, “Etch rates for micromachining processing,” *Journal of Microelectromechanical Systems* **5**(4), 256-269 (1996).

[29] ASTM Standard B322, 1999 (2009), “Guide for cleaning metals prior to electroplating,” ASTM International, West Conshohocken, PA, DOI: 10.1520/B0322-99R09.

[30] ASTM Standard B482, 1985 (2008), “Practice for preparation of tungsten and tungsten alloys for electroplating,” ASTM International, West Conshohocken, PA, 10.1520/B0482-85R08.

[31] I. S. Mahmoud, “Copper plating bath and process for difficult to plate metals.” Patent 4,990,224. 5 February 1991.

[32] ASTM Standard B322, 2012, “Standard test method for linear-elastic plane-strain fracture toughness K_{IC} of metallic materials,” ASTM International, West Conshohocken, PA, DOI: 10.1520/E0399-12.

[33] G. R. Odette and B. L. Chao, unpublished notes.

[34] H. Tada, P. C. Paris, and G. R. Irwin, “The stress analysis of cracks handbook,” 3rd ed., American Society of Mechanical Engineers, New York, 2000.

[35] R.A. Pitts, S. Carpentier, F. Escourbiac, T. Hirai, V. Komarov, S. Lisgo, A.S. Kukushkin, A. Loarte, M. Merola, A. Sashala Naik, R. Mitteau, M. Sugihara, B. Bazylev, and P.C. Stangeby, “A full tungsten divertor for ITER: Physics issues and design status,” *Journal of Nuclear Materials* **438**, S48-S56 (2013).

[36] J. H. Weaver, J. Yang, and F. W. Zok, “Control of interface properties in oxide composites via fugitive coatings,” *Journal of the American Ceramic Society* **91**(12), 4003-4008 (2008).

[37] S. Antusch, P. Norajitra, V. Piotter, H.-J. Ritzhaupt-Kleissl, and L. Spatafora, “Powder injection molding – An innovative manufacturing method for He-cooled DEMO divertor components,” *Fusion Engineering and Design* **86**, 1575-1578 (2011).

[38] W. J. Clegg, “The fabrication and failure of laminar ceramic composites,” *Acta Metallurgica et Materialia* **40**(11), 3085-93 (1992).

CHAPTER 2

ON THE REMARKABLE FRACTURE TOUGHNESS OF 90 TO 97W-NiFe ALLOYS REVEALING POWERFUL NEW DUCTILE PHASE TOUGHENING MECHANISMS

ABSTRACT

Tungsten is a leading candidate for fusion reactor divertors, but is too brittle to serve a structural function. Here, we explore the remarkable fracture toughness of 90 to 97 wt.% W liquid phase sintered W heavy alloys (WHAs). The room temperature WHA fracture toughness, containing only 3 wt.% of a NiFe-based ductile phase, is ≈ 9 to 18 times higher than for unalloyed W. All the WHAs show extensive stable crack growth, with an average maximum load toughness K_{Jm} ≈ 69 to 107 MPa√m, and a blunting line toughness, prior to significant crack growth, averaging ≈ 170 MPa√m. In contrast to classical ductile phase toughening, which is primarily due to macrocrack bridging and deflection, WHA toughening mainly involves new mechanisms associated with arrest, blunting and bridging of numerous process zone microcracks. Tests down to -196°C, to partially emulate irradiation hardening, show large K_{Jm} even at very high W strength.

2.1. INTRODUCTION

Due to its high melting temperature, good conductivity, low sputtering rates and high strength, tungsten (W) is currently considered to be the most promising candidate for plasma facing components of the fusion reactor divertor applications [1–4]. However, elevated brittle to ductile transition temperatures and low toughness (and low tensile ductility), which are further degraded in service by neutron irradiation, limit the application of monolithic W as a structural material [1–7]. There have been many attempts to improve the ductility and toughness of tungsten by alloying, grain refining-nanostructuring and compositing [1–3,5–17]. For example, Re is known to improve the ductility of W by solid solution softening that enhances dislocation mobility, and by

increasing the number of available slip systems [1,12–16]. However, the use of Re in W has been ruled out due to its cost and detrimental effect on radiation damage [1,18]. Other solutes, like Ta, V, Mo, Os, Ti and Cr, have negligible to negative effects on W ductilization [1,15–17]. Grain refinement by rolling, severe plastic deformation (SPD), and oxide dispersion stabilization, generally improves W ductility to some extent, but has mixed effects on toughness [6–9,19]. However, such deformation processing paths result in highly anisotropic properties and textured microstructures, and are otherwise unsuitable for fabricating complex components [1,6–10].

One promising approach to toughening is to composite W with a ductile phase. Ductile phase toughening (DPT) restricts crack propagation in brittle matrix systems by crack bridging, arrest/re-nucleation and deflection mechanisms. Indeed DPT has been successfully applied in many brittle matrix systems [20–23]. Tungsten heavy (metal) alloys (WHAs), or composites, typically containing 78-98 wt.% W, along with a balance of ductile phase metals like Ni, Fe, Cu, Co, have been studied for several decades [24–40]. The WHAs are typically W powders consolidated by liquid phase sintering (LPS). Most of the previous research focused on processing optimization and relating WHA microstructures to their tensile properties. WHAs are used in radiation shields, kinetic energy penetrators, counterbalances, vibration dampers, and rocket nozzles. A good review paper on WHAs can be found in [41].

Recently, various WHAs have been considered as potential structural plasma facing materials for fusion reactor divertor applications [5,28,42,43]. Important characteristics of the WHA ductile phase constituent include:

Melting temperature (T_m)

Strength, ductility and toughness

Immiscibility with W and the absence of brittle intermetallic phase formation

The W-ductile phase interface bond strength

Long half-life radioactivity of ductile phase constituents

For example, W-Cu WHAs have been extensively studied, but suffer both from a low Cu $T_m \approx$ 1085ºC and strength, compared to the 50Ni30W20Fe face centered cubic solid solution phase that forms during the LPS of the W powders. The NiWFe phase $T_m \approx$ 1450ºC [44] is comfortably above the 1300°C limit, typically imposed on monolithic W, in order to avoid highly embrittling recrystallization [42,43]. Further, W-based divertor components will almost certainly be metallic hybrid systems; for example, the WHA may serve as a crack arrest layer for He-cooled plasma facing thimbles composed of bonded multilayers, like W-WHA-ODS-Cu [1–3].

WHAs generally have fairly good room to high-temperature tensile strength and ductility [28–31,34–36,39–41]. However, the key limiting structural property for W and W-alloys is fracture toughness and high brittle to ductile transition temperatures (BDTT) [3,6–8]. It is important to emphasize that fracture toughness relates to the resistance of a material to the propagation of a pre-existing sharp crack. Thus, fracture toughness cannot be determined by the strength and ductility as measured in tensile or flexure tests. Indeed, a metal may be ductile in a tensile test, while being extremely brittle in a fracture toughness test. Low fracture toughness is a significant issue for fusion divertor applications, since high and cyclic thermal loads typically result in the formation of many sharp surface cracks [1,2,11,45].

There are very few papers in the literature reporting pre-cracked fracture toughness data on W-NiFe WHAs. The most useful study reported room temperature (RT) resistance curve J-da R-curve data for ≈ 93-95W WHAs [37]. The ASTM E813-88 based initiation K_{Jc} ranged from 152 to 210 MPa$\sqrt{m}$. Strong resistance curve behavior was observed along with extensive stable crack growth.

The objective of this study is to measure the fracture toughness, and to explore the toughening mechanisms, in four 90 to 97W-NiFe WHAs from RT down to liquid nitrogen temperature (-196°C), using fatigue precracked bend bars following ASTM test standards discussed below. The lower temperature tests were intended to partially emulate the irradiation hardening that occurs at higher temperatures in service. Microhardness and uniaxial tensile tests from -196°C to RT were also conducted. Optical and scanning electron microscopy (SEM) were used for microstructural characterization and to investigate the fracture mechanisms and modes.

The W-NiFe WHA microstructure is composed of a 3-dimensional, NiWFe ductile phase honeycomb web surrounding the unalloyed W powders. Our study revealed that the toughening in the W-NiFe WHA is dominated by new mechanisms associated with this microstructure. In most classical ductile phase toughening systems, the matrix phase remains brittle, while the ductile phase toughening is due to bridging of the *macrocrack* wake, as well as crack arrest-re-nucleation-deflection mechanisms [20,22]. However, in the case of the W-NiFe WHA, toughening is dominated by *microcrack* arrest, blunting and bridging in a fully ductilized crack tip plastic zone. Plastic zone deformation, including in the embedded W particles, and dilatational microcrack blunting, dissipate large amounts of energy. Further, the process-zone dilatation extensively shields the crack tip stress fields, including wake effects. Microcrack blunting shielding is far more effective than that provided by elastic microcracks in brittle matrix systems [46–48]. To the best of our knowledge, these *ductile* process zone microcrack toughening mechanisms have not previously been identified and explored in metallic alloys. However, similar toughening effects have been observed in some polymer-rubber composites [49].

2.2. MATERIALS AND METHODS

2.2.1 Materials

The four commercial (Mi-Tech Metals, Indianapolis, IN, USA) liquid-phase sintered (LPS) were received in the form of 100mm x 100mm x 14mm plates. The WHAs contained 90, 92.5, 95 and 97 wt. % W, as shown in Table 2.2.1, with a balance of an initially 70% Ni and 30 %Fe phase. The Ni-Fe phase becomes enriched with 30%W during LPS resulting in an fcc solid solution composition of ~ 50% Ni, 30% W and 20% Fe, which we call the NiWFe ductile phase (DP). The NiWFe phase forms a semi-continuous honeycomb web structure surrounding a much larger volume fraction of W-particles.

Table 2.2.1 WNiFe alloy compositions (wt.%) and the size and contiguity of the W particles

WHA	W	Ni	Fe	W particle size (μm)	W-W contiguity, C_w
90W	90.27	6.78	2.95	17 ± 7	0.161
92.5W	92.48	5.33	2.19	18 ± 7	0.197
95W	95.03	3.48	1.49	26 ± 11	0.224
97W	97.13	2.01	0.86	38 ± 15	0.315

2.2.2 Microstructural Characterization

The WHA specimens (see below) were fabricated by electrical discharge machining (EDM). They were ground with 220 to 2000 grit sand paper to remove EDM damage and residual surface stresses. Some specimens were then polished down with 0.5μ-diamond paste and etched in a 30% hydrogen peroxide solution for 10 min to facilitate microstructural characterization. Scanning electron microscopy (SEM) with energy dispersive spectroscopy (EDS), and electron backscatter diffraction (EBSD) were used to image the W particles and the surrounding NiWFe

ductile phase, and to identify their respective compositions. The W particle size distribution was determined by sampling ~500 individual grains using 'ImageJ64' software. The particle aspect ratio (PAR) was defined by dividing the longest dimension (l) to the shortest dimension (s) of a particle. The cleavage crack length and the mid-crack opening displacement were defined by measuring the length and the maximum width of a crack, respectively. Contiguity (C_w) defines the amount of W-W contact, and is expressed as $C_w = (S_{w-w})/S_w$ where S_w is the surface area of the W grains, and S_{w-w} is the surface area of W-W contacts [34,35]. The area fraction of the NiWFe was determined by converting SEM EBSC micrographs into binary black-white images, and measuring the fraction of the white area (see Fig. 2.1). The NiWFe DP honeycomb structure thickness (t) was measured using a line-intercept method (LIM), as the average width of the NiWFe phase measured on lines drawn on the binary image [30]. The NiWFe DP thickness/W length ratio was also calculated by the same LIM, by dividing the total intersected DP length by the total intersected W length. The percentages of the various local fracture modes were also determined by the LIM.

2.2.3 Microhardness and Tensile Testing

Vickers microhardness measurements (H_v) at RT were performed on the polished surfaces at a 500g load with 10 seconds dwell, using a LECO M-400A semi-automated hardness tester. The reported average values and standard deviations are based on 10 to 15 indents. A Zwick microhardness tester was used for corresponding H_v measurements at the liquid nitrogen (LN_2) boiling point of -196°C, also at a 500g load. In this case, polished hardness specimens were located inside a small insulated stainless steel cup mounted on a stage below the indenter. A charge of LN_2 was poured into the cup to cool the specimen and indenter that were held for 5 minutes to reach a stable temperature of ≈ -196°C.

Uniaxial tensile tests from RT to -196°C were performed on EDM fabricated flat dog-bone shaped sub-sized SSJ-2 specimens with a gauge section length x width x thickness of 5.0 x 1.2 x 0.5 mm [50]. The tensile specimens were sanded with 1500 grit to remove surface oxides and contamination, minor cracks and local residual stresses due to the electrical discharge machining (EDM). Tests were carried out on a MTS 810 servo-hydraulic universal testing machine, equipped with a LN_2 cooling chamber. A controlled LN_2-air mixture was injected into the cooling chamber to reach the targeted temperature that was stabilized for 30 to 45 min before testing. The tensile tests were conducted at a displacement rate of 0.30 mm/min, equivalent to a strain rate ≈ 10^{-3}/s; at least 3 tests were conducted for each alloy-temperature condition. The tensile properties were generally determined in accordance with ASTM test standard E8M-15a [51]. The strain hardening exponent (n) was determined by fitting a simple power-law hardening equation

$$\sigma_t = k\varepsilon_t^n ,$$

where σ_t and ε_t are the true stress and true strain from yielding to the onset of necking (e.g., the plastic portion of true stress-strain), and k is strength coefficient.

2.2.4 Fracture Toughness Tests

Room temperature fracture toughness tests were primarily conducted on small fatigue pre-cracked, single-edge notch bend bar specimens with a nominal length (L) x width (W) x thickness (B) dimensions of 16 x 3.3 x 1.65 mm [52]. The specimens were pre-cracked to nominal crack length (a)-to width (W) ratios, (a/W) ≈ 0.40 to 0.5 up to a maximum ΔK_I =18 MPa$\sqrt{m}$ and a load ratio R = 0.1. The specimens were heat-tinted at 400ºC for 1 min to mark the pre-crack front. Both three-point (3PB) and four-point (4PB) bend fixtures were used on a 810 MTS servo-hydraulic universal testing machine. To facilitate *in-situ* optical observation of the crack tip region, the fracture specimen sides were sanded with a sequence of 2000 grit SiC followed by 9µ, 3µ

and 1μ diamond lapping paper. Initially 4PB tests were conducted at RT, in part to permit extensive crack growth without the influence of the loading tup. However, since the crack growth was generally found to be highly stable, subsequent fracture tests used a 3PB fixture with only limited crack growth.

The fracture tests were carried out at a crosshead speed of 0.04mm/min. ASTM standards E1921 [53] and ASTM C1421 [54] were used to calculate the elastic components of the fracture toughness, for the 3PB and 4PB tests, respectively. ASTM E1921 was used to calculate the plastic component for the both 3PB and 4PB tests. The K_{Jm} were calculated at the maximum load (P_m) in the load-displacement (P-d) curve. Blunting curve toughness ($K_{J0.8}$) was also evaluated at post-peak loads down to ≈ 80% of P_m, since there was minimal crack growth (< 200 μm) for the displacements up to this loading point. The 4PB tests were carried out down to very low P, resulting in extensive crack tearing to near the back of the specimen. The 3PB tests were stopped at P/P_m of 0.77 to 0.92 to better evaluate an initiation toughness and corresponding crack tip opening displacement (CTOD) which ranged from 16 to 56 μm, averaging 35 ± 13 μm. The pre-crack and post-test crack lengths were also measured after the specimens were broken in LN_2 to ensure no further ductile crack extension had occurred. All the low-temperature toughness tests were conducted using 3PB fixture, and P_m was used to calculate K_{Jm}. Three to seven specimens were tested for each condition.

Finally, small specimen 3PB tests were carried out at temperatures down to liquid nitrogen (LN_2) at ≈ -196°C. There is a transition from ductile tearing to elastic fracture at a temperature that depends on the WHA W content. However, the corresponding K_{Ic} were still ≈ 6 times higher than for monolithic W.

2.3. RESULTS

2.3.1 Microstructural Characterization

The SEM micrographs of the polished and etched W-NiFe plates shown in Fig. 2.3.1 reveal roughly spheroidal W particles (PAR: 1.1 ± 0.2) surrounded by an interconnected honeycomb web structure of the ductile NiWFe phase. As summarized in Fig. 2.3.1 and Table 2.3.1, multiple EDS and electron probe microanalysis (EPMA) scans show that the particles are close to 100% W (point 1 of Fig. 2.3.1g), while the NiWFe ductile phase is approximately 50%Ni, 30%W and 20%Fe, by wt.% (point 2 of Fig. 2.3.1g).

Figure 2.3.1 and Table 2.2.1 also show the W–particle size increases from ≈ 17 μm for 90W alloy to ≈ 38 μm for 97W alloy. The increase in the particle size with increasing particle loading is associated with less dissolution of W needed to maintain a similar composition in the NiWFe phase. The average NiWFe web thickness is roughly similar in all the W-NiFe WHAs at ≈ 4.9 ± 0.8 μm. As expected, the area fraction of the NiWFe phase decreases from ~16% for 90W to ~6% for 97W. However, microstructural inhomogeniety is observed for different batches of plates (for same WHA), or even within the same plate. For example, the average local DP area fraction for specimen-1 and 2, obtained from the same plate, is 22.4 and 13.1%, respectively, for 90W; and that is 9.2% and 5.7% for 97W (see Fig. 2.3.2). A higher W fraction lowers the NiWFe phase continuity and increases both the W-W contiguity and the frequency of particle bonded W-W interfaces [35], while reducing the NiWFe/W t/d ratio (Fig 2.3.1e,f and Tables 2.2.1 and 2.3.1).

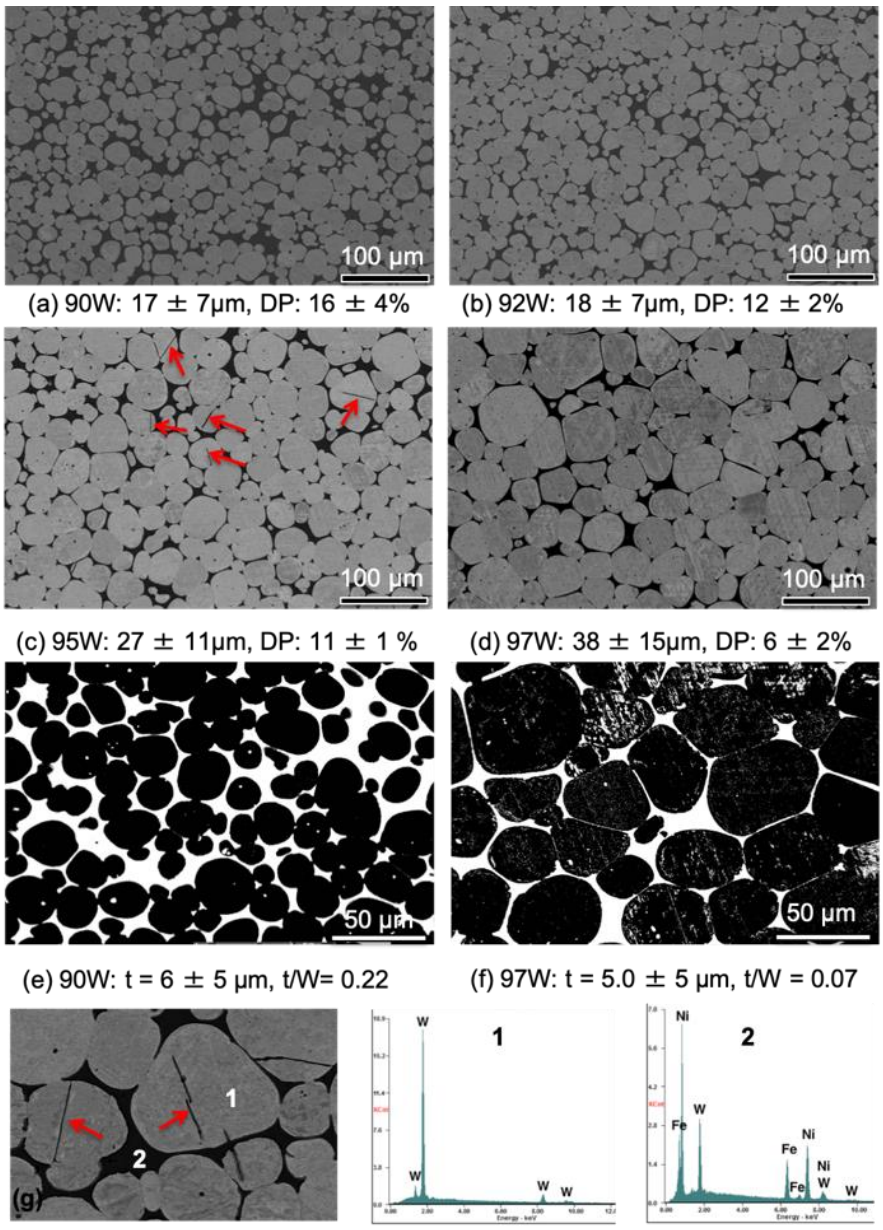

Figure 2.3.1 SEM images of the W particles (gray) and the ductile NiWFe phase (black) for: (a) 90W, (b) 92.5W, (c) 95W, and (d) 97W WHA, respectively. The binary black (W) and white (NiWFe) images of: (e) 90W, and (f) 97W highlight the NiWFe honeycomb web characterized by the web thickness (t), and the t/W, thickness to W particle fraction ratio. Fig. (g) shows cracked W particles (short red arrows) in the as-received condition. Point 1 and 2 in (g) show EDS spectra for the unalloyed W phase and NiWFe ductile phase, respectively.

Table 2.3.1 The composition and morphology of the NiWFe honeycomb web structure

WHA	Ni/W/Fe (wt.%)	NiWFe Area fraction (%)	Thickness, t (μm)	t/W (μm/μm)
90W	51.2/28.5/20.3	16.1 ± 3.8	5.9 ± 5.4	0.22
92.5W	49.1/31.3/19.6	11.8 ± 2.2	4.0 ± 3.7	0.12
95W	49.1/32.2/18.7	10.7 ± 1.3	5.1 ± 4.1	0.13
97W	48.3/34.3/17.4	6.4 ± 1.5	4.5 ± 5.0	0.07

t = NiWFe thickness, W = tungsten fraction

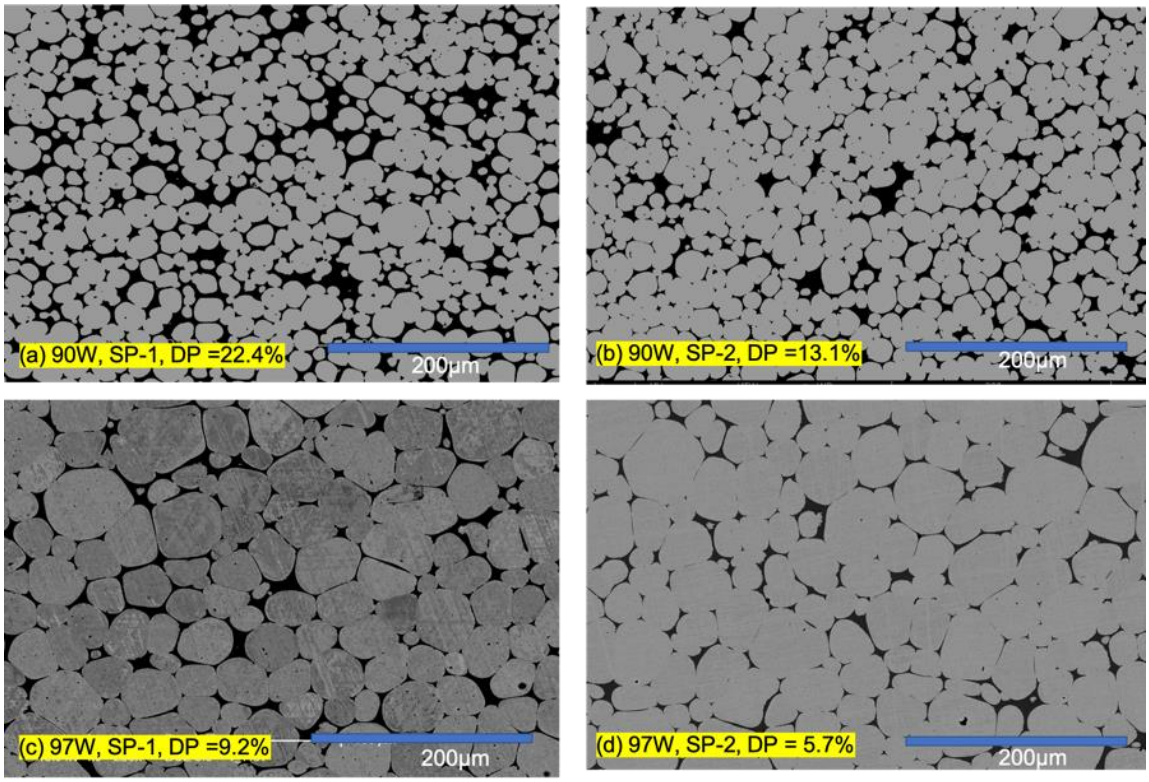

Figure 2.3.2 SEM Backscattered SEM images showing local microstructural variations prepared from two different specimens of same plate for: (a,b) 90W, and (c,d) 97W-NiFe alloys, respectively.

Fig. 2.3.1c shows the 95W WHA contains some pre-test cracked W particles (also, see the red short arrows in Fig. 2.3.1g), although the reason for this is not known. The EBSD inverse pole figure (IPF) maps (not shown) confirm expected random orientations of the W particles. Some large particles show multiple orientations, due to multiple internal grains or subgrains. These collective observations may be important considerations in tailoring the design of WHA.

2.3.2 Microhardness and Tensile Tests

Vicker's microhardness (H_v) results for W-alloys tested at RT and -196°C are shown in Fig. 2.3.3(a). The average hardness increases with increasing W at both RT (slightly) and -196°C (more strongly). As expected, the H_v is substantially higher at -196°C (507 ± 7 kg/mm$_2$ for 90W and 609 ± 21 kg/mm$_2$ for 97W) than at RT (321 ± 9 kg/mm$_2$ for 90W and 344 ± 9 kg/mm$_2$ for 97W). Monolithic W was also tested both at 23ºC (RT) and -196 °C, exhibiting a H_v of 358 ± 39 and 686 ± 79 kg/mm$_2$, respectively. No indentation cracking was observed in any of the alloy-test conditions.

Fig. 2.3.3(b) shows the engineering stress-strain $\sigma(\varepsilon)$ curves for all the WHA alloys tested at room temperature and -196ºC, along with a typical RT reactor pressure vessel (RPV) steel ($\sigma_y \approx 600$ MPa) for comparison. The corresponding tensile data is shown in Table 2.3.2, including for tests at -100°C. The RT $\sigma(\varepsilon)$ curves are generally similar, although the total elongation systematically decreases with increasing W. Significant strain hardening is observed in all cases at RT (see Table 2.3.2). The σ_y decreases above 92.5W at -100°C and above 90W at -196°C. In these cases, the tensile fracture is elastic with $\varepsilon_t = 0$, and at a fracture stress less than σ_y. Note that the microhardness increases with increasing W, especially at low temperatures, since loading is primarily in compression rather than tension.

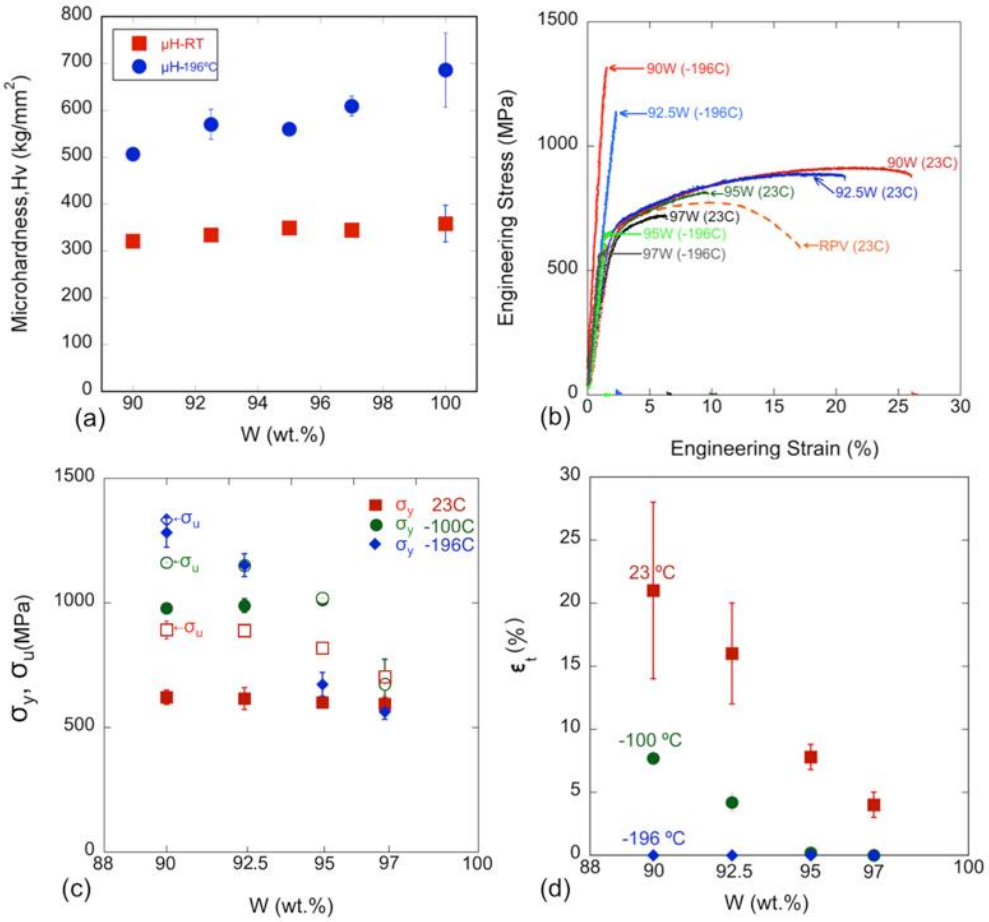

Figure 2.3.3 WHA tensile properties and hardness as a function of W content and temperature: (a) Vickers microhardness (H_v); (b) engineering stress-strain (σ-ε) curves; (c) the 0.2% yield (σ_y: filled symbols) and ultimate tensile (σ_u: unfilled symbols) stresses; and, (d) the total elongations ($\mathfrak{E}$).

Fig. 2.3.3(d) shows the total elongation (ε_t) decreases with increasing W at RT. The ε_t also decreases with decreasing temperature, falling from ≈ 21% to ≈ 8% for 90W and ≈ 16% to ≈ 4% for 92.5W at RT and -100ºC, respectively. Moreover, ε_t ≈ 0% at -196ºC for all W contents (see Table 2.3.2). The 95W to 97W also fall to 0% (elastic fracture) at -100ºC. The uniform elongation (ε_u) is very close to ε_t, since fracture takes place almost immediately after the onset of necking, except for 90W and 92.5W RT tests with the reductions of area (RA) varying between ≈ 27 to 13%, respectively.

Table 2.3.2 Tensile properties of WHAs as a function of W content and temperature

T (ºC)	WHAs	σ_y (σ_f) (MPa)	σ_u (MPa)	ε_u (%)	ε_t (%)	n
23	90W	621 ± 29	891± 35	18 ± 4	21 ± 7	0.23 ± 0.01
	92.5W	616 ± 44	886 ±12	13.5 ± 2.2	16 ± 4	0.23 ± 0.02
	95W	600 ± 15	818 ± 10	7.3 ± 1	8 ± 1	0.22 ± 0.02
	97W	594 ± 27	701 ± 67	3.4 ± 1	4 ± 0.7	0.16 ± 0.06
-100	90W	978 ± 16	1162 ± 20	7.5 ± 0.4	7.7 ± 0.4	0.16 ± 0.01
	92.5W	989 ± 28	1149 ± 16	4.0 ± 0.7	4.2 ± 0.7	0.15 ± 0.01
	95W	1019 ± 18	1019 ± 18	0	0	-
	97W	673 ± 101	673 ± 101	0.0	0.0	-
-196	90W	1292 ± 59	1332 ± 16	0.2 ± 0.4	0.2 ± 0.4	-
	92.5W	1151 ± 46	1151 ± 46	0	0	-
	95W	673 ± 48	673 ± 48	0	0	-
	97W	563 ± 31	563 ± 31	0	0	-

σ_y = 0.2% yield stress, σ_f = fracture stress, σ_u = ultimate tensile strength, ε_u= uniform elongation, ε_t= total elongation, n = hardening exponent.

SEM micrographs of the fracture surfaces of the broken RT tensile WNiFe specimens, shown in Fig. 2.3.4, manifest four local failure modes, namely: W-W intergranular fracture (WW), W cleavage (WC), W-NiWFe interfacial debonding (WD), and NiWFe ductile phase rupture (DR). These local failure modes have been widely reported in previous studies of WHA [24,29,30,33–35,37–40]. The WW interface is the weakest and, as expected, this fracture mode increases with increasing W [24,29,34,35,37–40]. More quantitatively, WW fracture correlates with the fraction of contiguity (C_w), which also increases with increasing W% (see Table 2.2.1). Global fracture often initiates at W-W fracture sites and continues by cleavage crack propagation through the W

particles, leaving intact NiWFe web ligaments that can arrest the microcracks. Figs. 2.3.4(a)-(d) show that the fraction of WC is highest for the 90W WHA, which experience the lowest number of WW events, and is least for the 97W alloys that experience more WW fracture. Notably, WC fracture appears to correlate with higher tensile strength and ductility (see Table 2.3.2 and Fig. 2.3.4). Ductile web knife-edge rupture features surround the fracture facets.

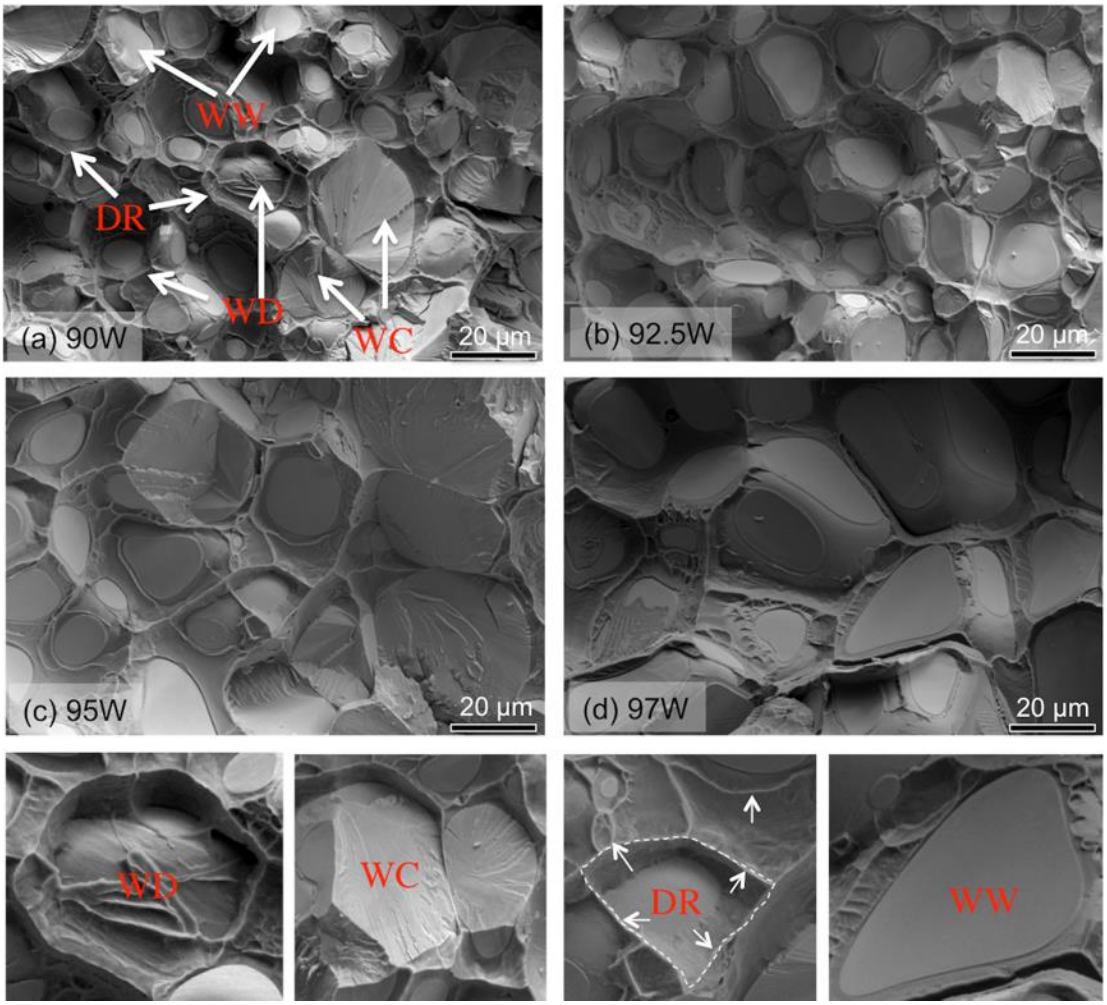

Figure 2.3.4 SEM RT tensile test fractographs for: (a) 90W, (b) 92.5W, (c) 95W, and (d) 97W showing the four basic fracture modes: WD - W particle-NiWFe ductile phase interface decohesion; WC - W particle cleavage; DR - NiWFe ductile phase rupture; and, WW – W-W intergranular fracture. Magnified views of these various processes are shown in the bottom row of figures.

While at RT more WC fracture correlates with higher ductility, at lower temperatures the fracture surfaces shown in Fig. 2.3.5 indicate the opposite trend, with increasing amount of WC fracture leading to decreasing ductility. The increase in WC with decreasing temperature is due to the corresponding decrease in the cleavage fracture toughness of the W particles. The strength and ductility of the ductile NiWFe phase is much less sensitive to temperature than the W-particle fracture stress [33]. For example, the 90W alloy shows increasing amount of WC fracture at -100ºC coupled with a lower ε_t ≈ 8% compared to 21% at RT, and an ε_t ≈ 0% at -196°C, where almost 100% WC is observed. In general, the fraction of WC increases with increasing W% and decreasing temperature, leading to lower or no ductility below RT.

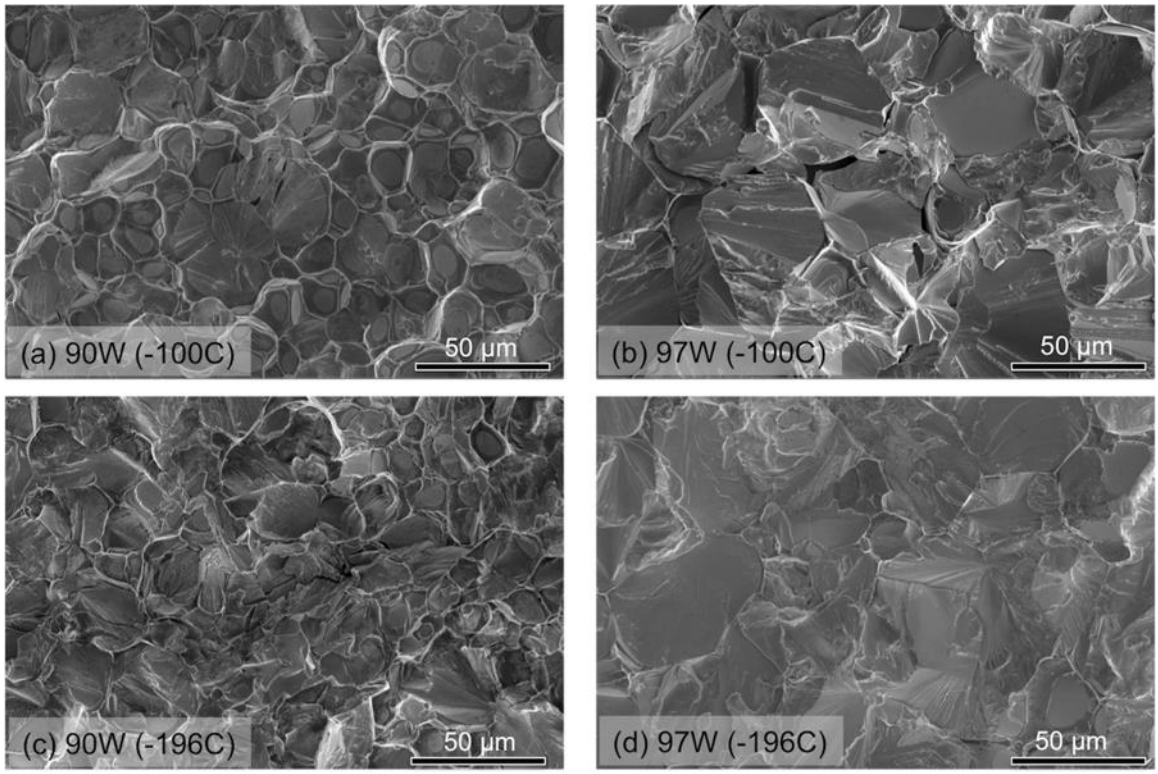

Figure 2.3.5 SEM fractographs showing the fracture surfaces for the 90W (left) and 97W (right) for tensile tests at -100ºC (a-b) and -196ºC (c-d).

2.3.3 Room Temperature Fracture Toughness Tests

RT fracture toughness tests were conducted on the 16 x 3.3 x 1.65 mm (nominal dimensions) single-edge notched fatigue pre-cracked bend bars using both 4PB and 3PB test fixtures. The fatigue cracks tend to mainly propagate through the NiWFe DP, irrespective of alloy compositions, as shown by the white arrows in Fig. 2.3.6a. In situ measurement of crack growth during the test (e.g. optically and by digital image correlation) proved to be difficult due to the large plastic zone and lateral contraction (the black arrows in Fig. 2.3.6b and c) near the blunting crack tip. Further, crack wake bridging precludes the use of standard unloading compliance methods to measure da. Thus K_{Jm} was defined at the maximum load (P_m) based on the ASTM E1921 standard practice method of estimating the elastic-plastic J-integral J_m, as $K_{Jm} = \sqrt{\{J_m E/(1-\nu^2)\}}$, where E is the elastic modulus (≈ 400 GPa) and ν is Poisson's ratio (≈ 0.28) [53,55]. The ASTM E1921 validity limit for the specimen dimension is given by $K_{Jlim} = [Eb_o\sigma_y/30(1-\nu^2)]^{0.5}$, where b_o is the unbroken ligament (1.65 to 2.00 mm), and σ_y is the yield stress at test temperature (≈ 600 MPa at 23ºC). Thus, K_{lim} is ≈ 120 to 132 MPa$\sqrt{m}$. This K_{lim} is larger than all of the measured maximum load RT initiation toughness, K_{Jm} (≈ 93 ± 19 MPa$\sqrt{m}$, see Table 2.3.3). Hence the data are, in this sense, valid since cleavage could have occurred if the lower toughness ductile tearing processes had not intervened. Note, in steels, cleavage still occurs at $K_{Jm} > K_{lim}$, sometimes beyond the validity limit and after a small amount of ductile tearing, but this did not happen in the small W-NiFe WHA specimens. Further, it was found that small subsequent decreases of P below P_m remained on the blunting line, without significant crack growth. The decrease in P is mainly due to microcracking in the process zone (Fig. 2.3.6d). Here, the microcracking is primarily transgranular W cleavage (WC), shown by the thick-red arrows in Fig. 2.3.6d.

Continued loading beyond P = $P_{0.8}$ leads to initiation of extension and stable growth of cracks in the 4PB P-d tests that were continued to very large displacements (d). Stable crack

growth is reflected in the normalized load-displacement (P_n-d) curves shown in Fig. 2.3.7a. The normalization involves adjusting the measured P for various a/W to a common P for a/W = 0.5, based on the limit load ratio, $P_n = 0.25P/(1-a/W)_2$ [55]. The peak loads are similar except for the 95W alloy where the normalized P_m is somewhat higher for this particular test (see Fig. 2.3.7b). The P-d curves have an elastic loading region, followed by a plastic yielding deviation from linearity. The subsequent increasing P is due to the growth of the plastic zone and strain hardening. The much larger decreases in P following P_m reflect stable crack growth.

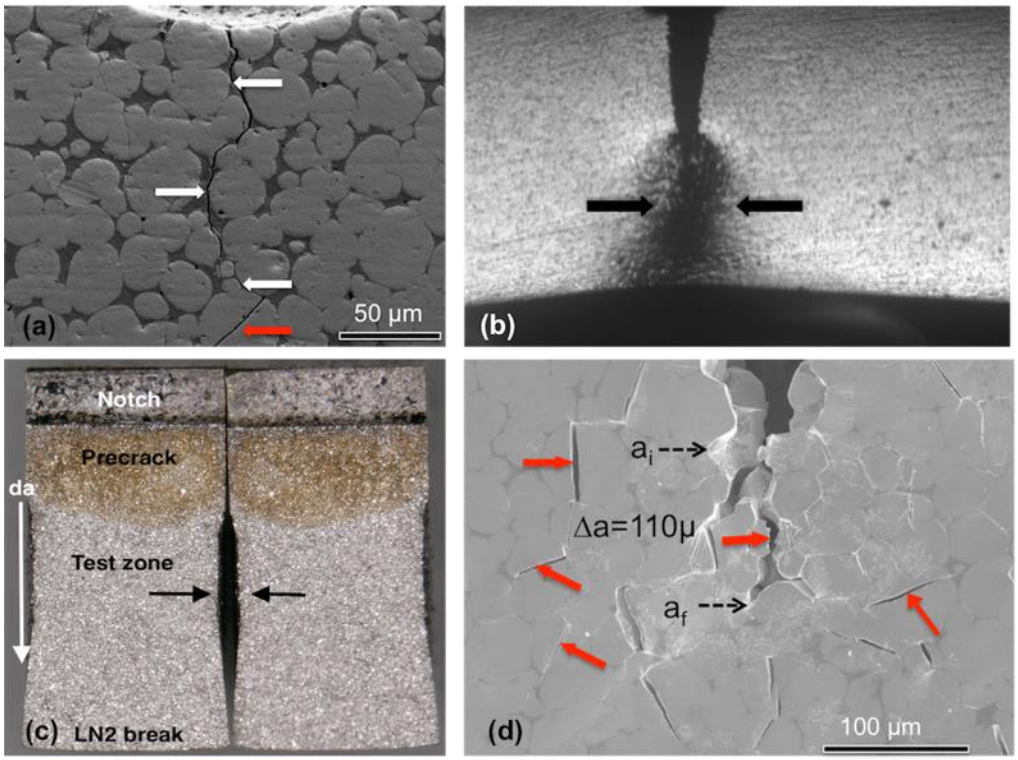

Figure 2.3.6 (a) A SEM image showing the fatigue cracks mainly propagate through the matrix phase (white arrows); (b, c) optical images showing lateral contraction at the plastic zone (black arrows); and, (d) transgranular (red arrows) cracks, a small amount of crack extension (Δa < 200μm) during loading, accompanied by extensive arrested microcracking.

Since 4PB tests show massive stable crack growth, additional tests were conducted on very finely ground (down to 1μ with diamond lapping paper) specimens in 3PB fixture, and a Questar long-distance (telescopic) optical microscope with 3-axis positioning was used to observe *in-situ* crack initiation and propagation at a frame rate of 6/min, as shown in Fig. 2.3.8. Here the black curve is the P-d for 97W. The numbers 1 to 5 correspond to the optical images at the loading points. The blue squares are the corresponding K_J for corresponding red-circled P-d points.

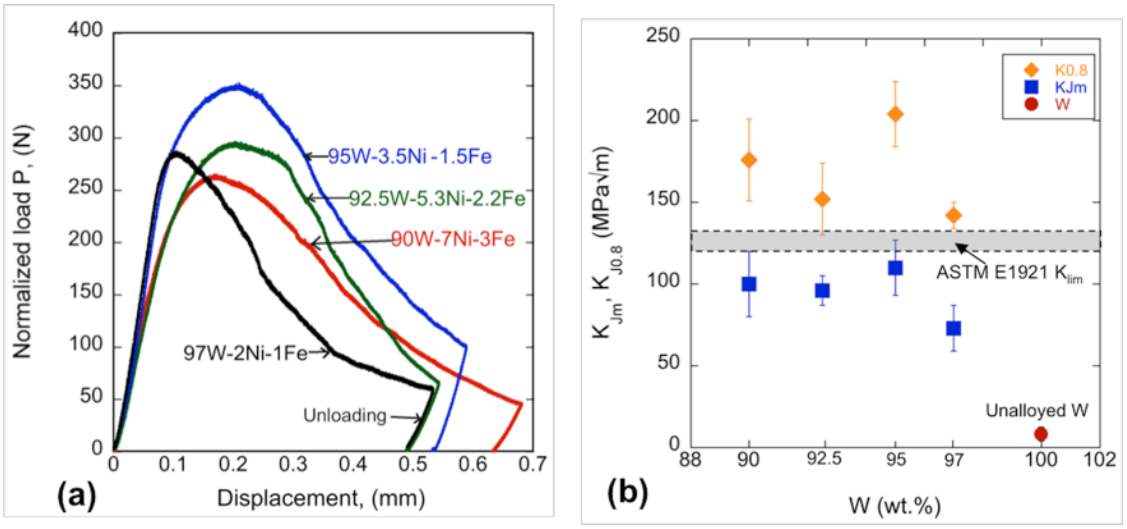

Figure 2.3.7 (a) RT P-d curves normalized to a/W=0.5 showing extensive stable crack growth; and, (b) the average K_{Jm} and $K_{J0.8m}$ of W-NiFe WHAs at P_m and $P/P_m \approx 0.8$. The ASTM E1921 K_{lim} (≈ 120-132 MPa√m) is also shown (gray rectangle). The actual crack extension is less than 200μm at $P/P_m \approx 0.8$.

The 3PB tests were stopped at a P/P_{max} from ≈ 0.77 to 0.92, since the lateral contraction and surface dimpling, indicated by the dark areas in Figs. 2.3.6b and 2.3.8, prevented imaging the crack tip. However, post-test optical and SEM images show that the crack extends by ≈ 130μm due to blunting at $P/P_m \approx 0.88$ with a corresponding blunting line toughness of $K_J \approx 139$ MPa√m, which is significantly higher than the maximum load $K_{Jm} \approx 90$ MPa√m (see insert of Fig. 2.3.8). Pre-and post-test SEM micrographs for all the RT 3PB tests show very little crack growth (da <

200 μm) when the loading was stopped (see Fig. 2.3.6d, for example). Thus, the K_J at $P/P_m \approx 0.8$ ($K_{J0.8}$) is plotted along with K_{Jm} in Fig. 2.3.7b. These results show that the $K_{J0.8}$ is ≈ 60-85% higher than K_{Jm} for the 90W to 95W alloys and ≈ 95% higher at 97W.

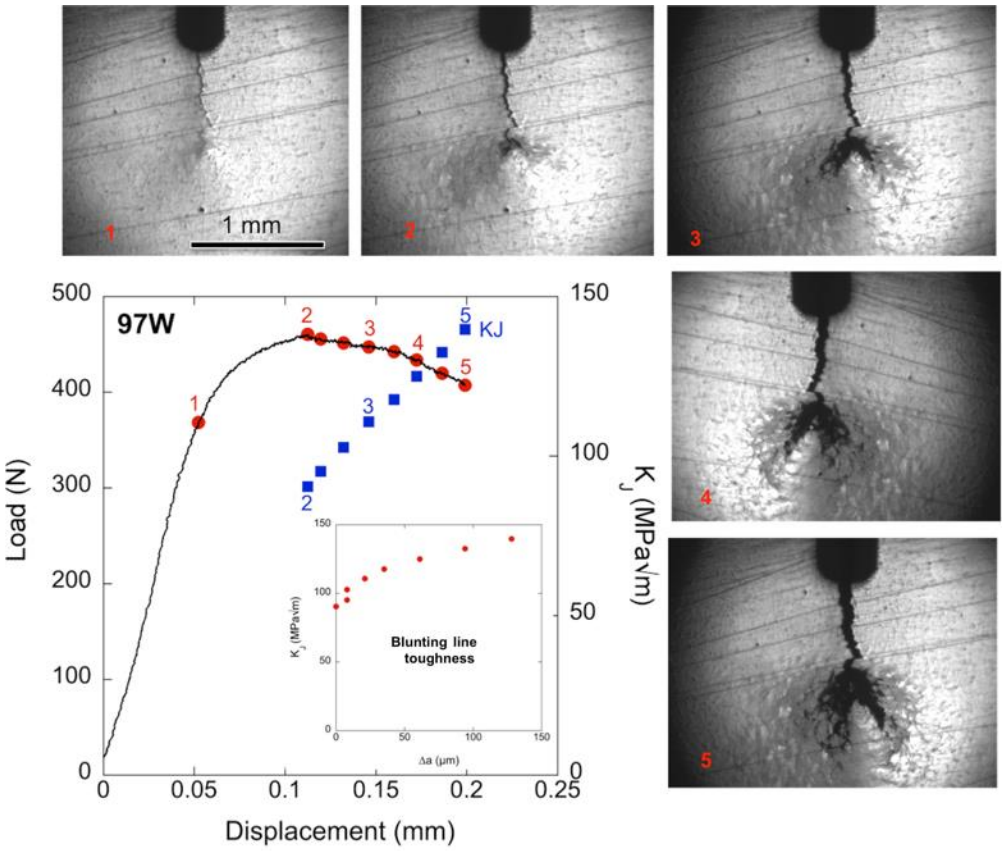

Figure 2.3.8 RT 97W WHA P-d curve with in-situ optical images showing the formation of a plastic zone indicated by the dark area, in front of the crack tip, that is out of focus due to lateral contraction. The red circles are P-d points and blue squares are their corresponding K_J values.The insert shows J-Δa based on optical and SEM image analysis. Note that the total crack extension is ≈ 130μ, corresponding to a blunting line toughness of ≈ 139 MPa√m.

The RT tensile results for the W-NiFe alloys show a systematic decrease in ultimate strength and ductility with an increasing W fraction. In contrast, the RT K_{Jm} are essentially the same up to 95W,

averaging 100 ± 15 MPa√m, in spite of the contiguity increase (see Tables 2.1 and 2.4). The K_{Jm} decreases to between 95W and 97W, where K_{Jm} = 69 ± 12 MPa√m. In this case, the K_{Jm} toughness is still ≈ 9x higher than that for typical monolithic W with K_{Ic} ≈ 8 ± 4 MPa√m; the corresponding $K_{J0.8}$ = 142 ± 8 MPa√m is ≈ 18x higher. The massive toughening provided by a relatively small addition of ≈ 5 vol.% (≈ 3 wt.%) of the ductile phase is remarkable. From a practical engineering perspective, crack initiation followed by extremely stable crack growth provides very high effective cracked body ductility in all cases.

Table 2.3.3 The K_{Jm} and $K_{J0.8}$ for the W-NiFe WHAs

Temp (ºC)	K_{Jm} or K_{Ic} (MPa√m)			
	90W	92.5W	95W	97W
23	97 ± 17	96 ± 12	107 ± 14	69 ± 12
-50	-	59 ± 9	65 ± 4	40 ± 2
-100	73 ± 4	48 ± 5	35 ± 4	32 ± 0.1
-150	50 ± 1	-	-	-
-196	36 ± 3	30 ± 3	27 ± 5	25 ± 2
23ºC ($K_{J0.8}$)	176 ± 25	152 ± 22	204 ± 20	142 ± 8

Post-test SEM studies of the sides of the 3PB bars, shown in Figure 2.3.9, demonstrate some of the multiple interacting toughening mechanisms: (i) crack wake bridging; (ii) process zone microcrack and microcrack bridging; and, (iii) as indicated by slip lines (and the grain shape changes, white dashed circles, as noted previously), plastic deformation of otherwise brittle W particles encapsulated by the DP. These mechanisms lead to the ductilization of the entire W-NiFe dual phase microstructure resulting in large crack tip CTOD ductility and the corresponding

development of large semi-classical plasticity zones. That is, on a macro scale, the RT fracture of the small W-NiFe WHA bend bars is entirely ductile.

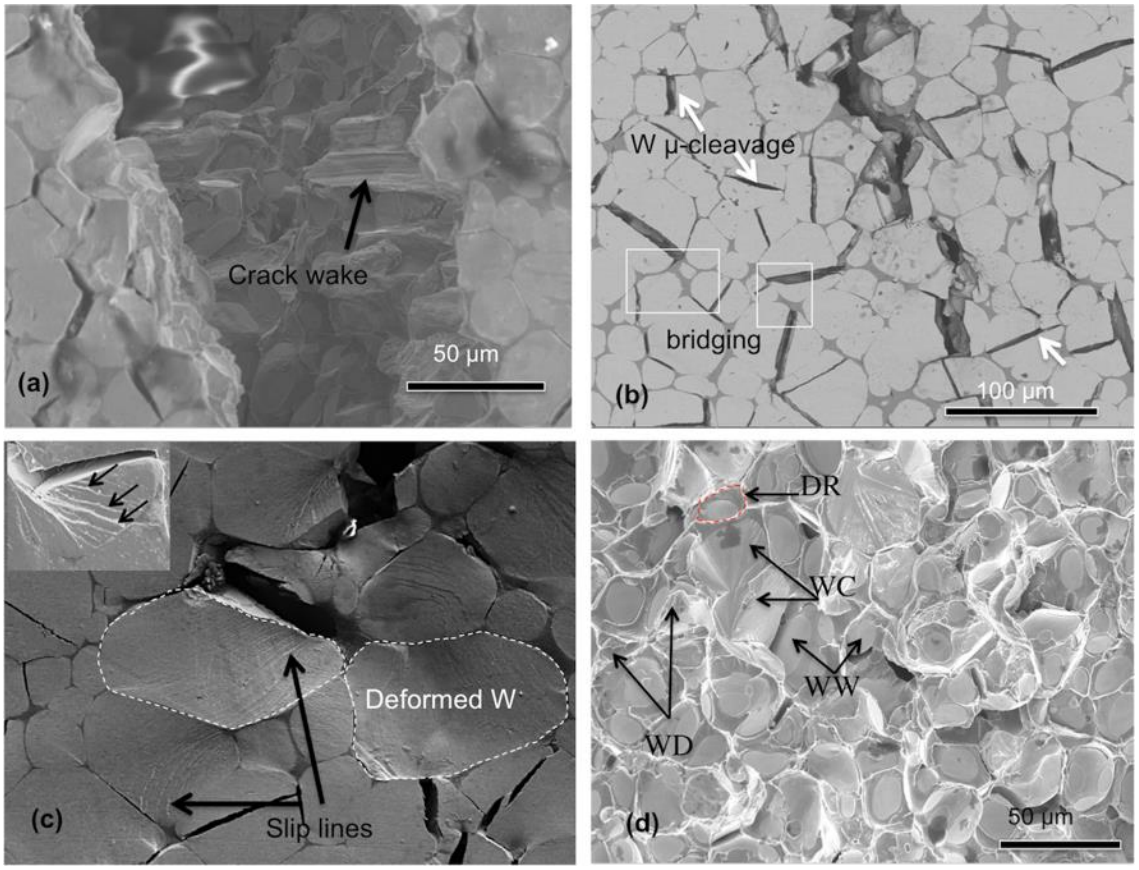

Figure 2.3.9 SEM images illustrating: (a) crack wake bridging; (b) stable microcracks and bridging; (c) slip lines in the deformed W-particles; and, (d) various local fracture modes.

The local fracture modes for the RT tensile tests previously reported in the literature [19,29,37,39] are similar to the results of this RT toughness study and report all four types of local fracture modes, (WC, WD, WW, DR) as seen in Fig. 2.3.9d. As shown in Table 2.3.4 below, the fraction of WW increases and WD decreases systematically with increasing W%, and the two modes account for ≈ 80% of the total local fracture. However, side surface observations (Figs. 2.3.6d,

and 2.3.9b) clearly show that there are large numbers of WC microcracks in the process zone that blunt and open under increasing load, thus producing large dilatational shielding effects.

Table 2.3.4 The percentage of local fracture modes from toughness fractographs.

T (ºC)	Alloys	WW	WC	WD	DR
23	90W	31.7	12.0	44.1	12.2
	92.5W	37.1	10.9	40.5	11.5 /17.9
	95W	42.6	13.5	32.8	11.1
	97W	67.2	17.6	10.8	4.4
-100	90W	35.6	12.5	42.4	9.5
	92.5W	15.3	68.2	13.9	2.6
	95W	2.5	91.5	5.1	0.8
	97W	4	96	0	0
-196	90W	2.6	95.6	0	1.8
	92.5W	3.7	96.3	0	0
	95W	2.7	97.3	0	0
	97W	3.5	96.5	0	0

2.3.4 Lower Temperature Fracture Toughness

Precracked 3PB were carried out on the W-NiFe WHAs at -50, -100, -150 and -196°C. The objective of these tests was to probe the effects of lower W toughness, associated with a higher $\sigma_y(T)$, to at least partly emulate the effects of irradiation hardening. Figure 2.3.10 shows representative normalized load-displacement (P-d) curves for all four W-NiFe WHAs from 23°C

to -196 ºC. Table 2.3.3 summarizes the corresponding K_{Jm}. Three to four tests were conducted for each condition (all the normalized P-d curves can be found in [56]). Note that, with only a few exceptions, the normalized peak loads for the redundant tests are similar. Unlike at RT, with substantial plastic yielding, the lower temperature P-d curves have a distinctly different shape. They either show a sharp peak followed by stable crack growth at a rapidly decreasing P, or elastic fracture associated with a large pop-in event. The overall average P_m at lower temperature decreases somewhat with increasing W. At -196°C elastic fracture occurs in all cases.

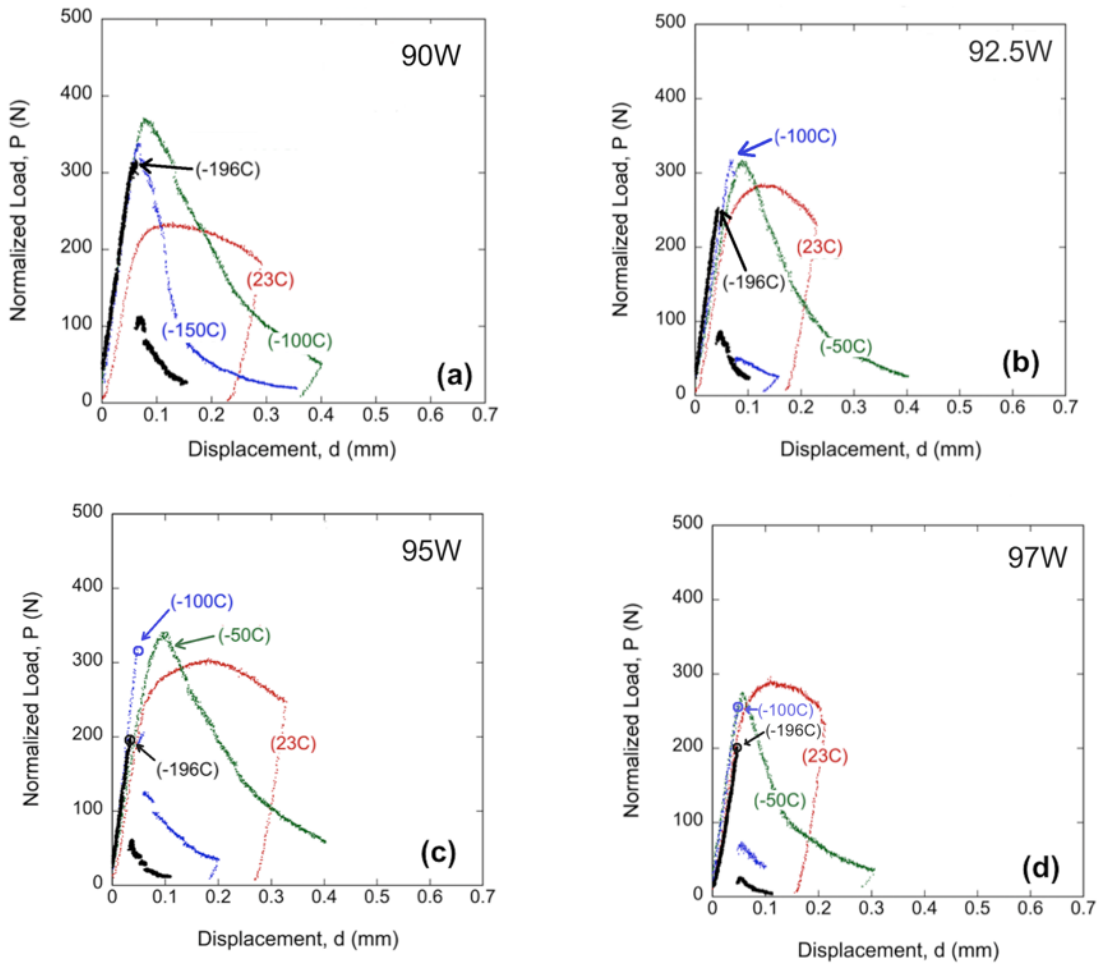

Figure 2.3.10 Precracked 3PB P-d curves for the 4 test temperatures normalized to a/W=0.5 for: (a) 90W; (b) 92.5W; (c) 95W; and, (d) 97W.

As shown in Fig. 2.3.10a, all the 90W WHA experience stable crack growth down to -100ºC. One of three tested 90W WHA fails elastically at -150°C. Thus, the elastic transition for the 90W WHA is estimated to be ≈ -150ºC, at an average K_{Jm} ≈ 50 ± 10 MPa√m. All the 92.5W specimens tested at -50ºC show stable ductile tearing with K_{Jm} averaging ≈ 59 ± 9 MPa√m (see Table 2.3.3 and Fig. 2.3.10b). However, only one of three 92.5W WHA tested at -100ºC experienced stable ductile tearing, while the others fracture elastically. Thus, the estimated elastic transition for the 92.5W WHA is ≈ -100ºC, with an average K_{Jm} value ≈ 48 ± 5 MPa√m. Similar to 92.5W alloy, 95W alloy also shows stable crack growth at -50ºC (see Fig. 2.3.10c). However, all the specimens tested at -100ºC and -196ºC show only elastic fracture. Thus, the corresponding BDT temperature of 95W WHA is estimated to be -75ºC with K_{Jm} ≈ 50 ± 15 MPa√m. Only one 97W WHA test showed stable crack growth at -50ºC, while others at -50ºC and lower temperatures experience elastic fracture (Fig. 2.3.10d). Therefore, a reasonable estimate of the BDT for 97W indexed at K_{Jm} = 50 MPa√m is ≈ -25ºC.

The corresponding K_{Jm} values are plotted in Fig. 2.3.11 and summarized in Table 2.3.3, respectively. The RT K_{Jm} is nearly constant up to 95W, but lower temperature K_{Jm} shows a noticeable decrease with increasing W and decreasing temperature. All the WHAs tested at -196°C fracture elastically with similar K_{Jm} = K_{Ic} ≈ 31 ± 6 MPa√m. Note there is no difference between K_{Jm} and K_{Ic} for fully elastic fracture. However, the average WHA K_{Ic} at -196°C is still much higher than that at RT for monolithic W with a K_{Ic} ≈ 8 ± 4 MPa√m, as shown in Fig. 2.3.11a. In general, in contrast to tensile strength, the K_{Jm} and K_{Ic} decrease with decreasing temperature and increasing tensile strength.

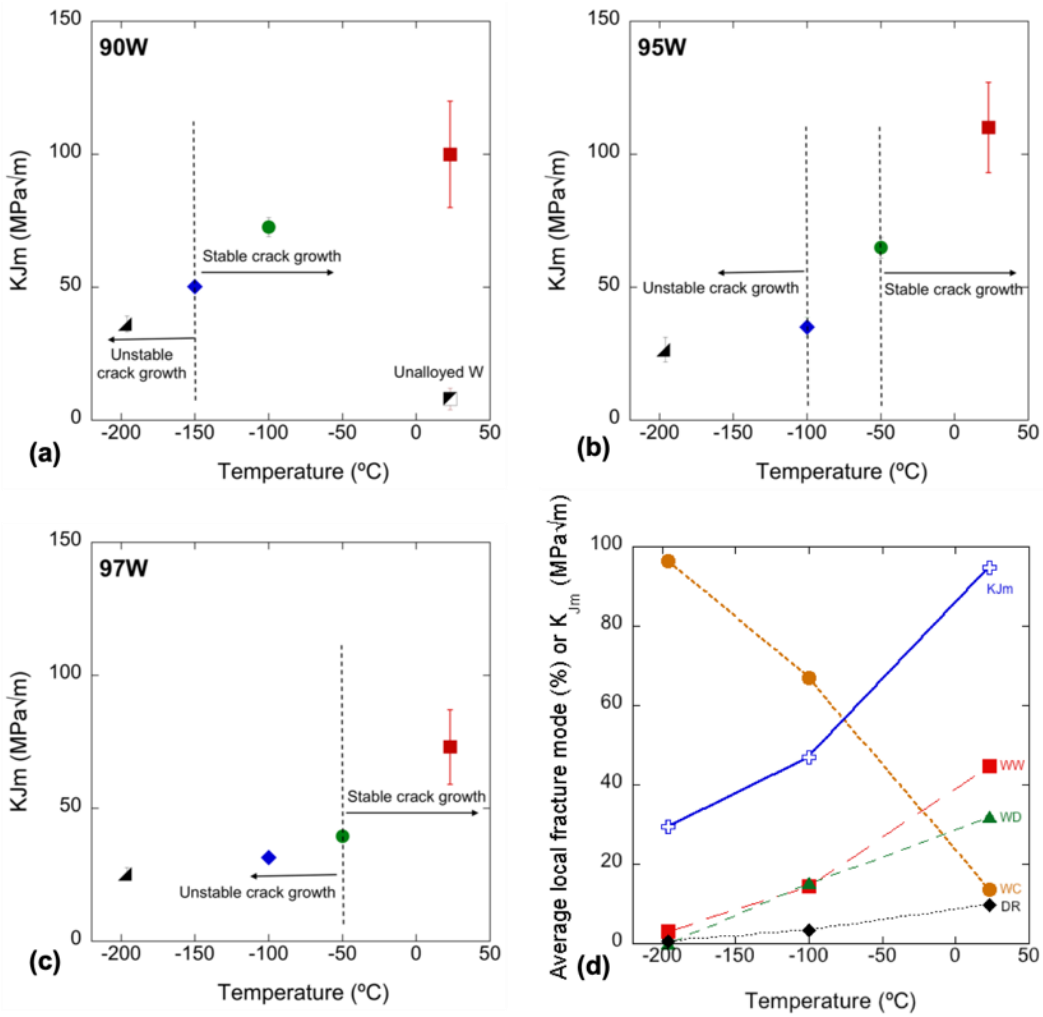

Figure 2.3.11 Maximum load K_{Jm}: (a) 90W; (b) 95W; (c) 97W alloys as a function of temperature; and, (d) the average local fracture mode percentages as a function of temperature, along with the corresponding average K_{Jm} or K_{Ic} for all the 4 WHAs for small specimens.

The plastic zone sizes at P_m decrease with decreasing temperature reflecting the higher σ_y. Representative SEM fractographs for 90W and 97W at varying test temperatures are shown in Fig. 2.3.12a and b, respectively. The percentages of the various local fracture modes are summarized in Table 2.3.4 and the averages as a function of temperature are shown in Fig. 2.3.11d along with the average K_{Jm}. The LIM analysis shows that the fracture surface at RT is

dominated by tungsten-tungsten interparticle boundary separation (WW) and tungsten-NiWFe ductile phase decohesion (WD), with relatively small percentage of W-cleavage (WC), or NiWFe ductile ligament rupture (DR). Since the W K_{Ic} deceases at lower temperature, the fraction of WC increases with increasing W and decreasing temperature. The local fracture mode is ≈100% WC at -196°C in all the WHAs. In general, WC increases with increasing W, decreasing temperature (except for the 90W WHA at -100ºC, which experiences a roughly equal frequency of the 4 local fracture modes at RT) and toughness.

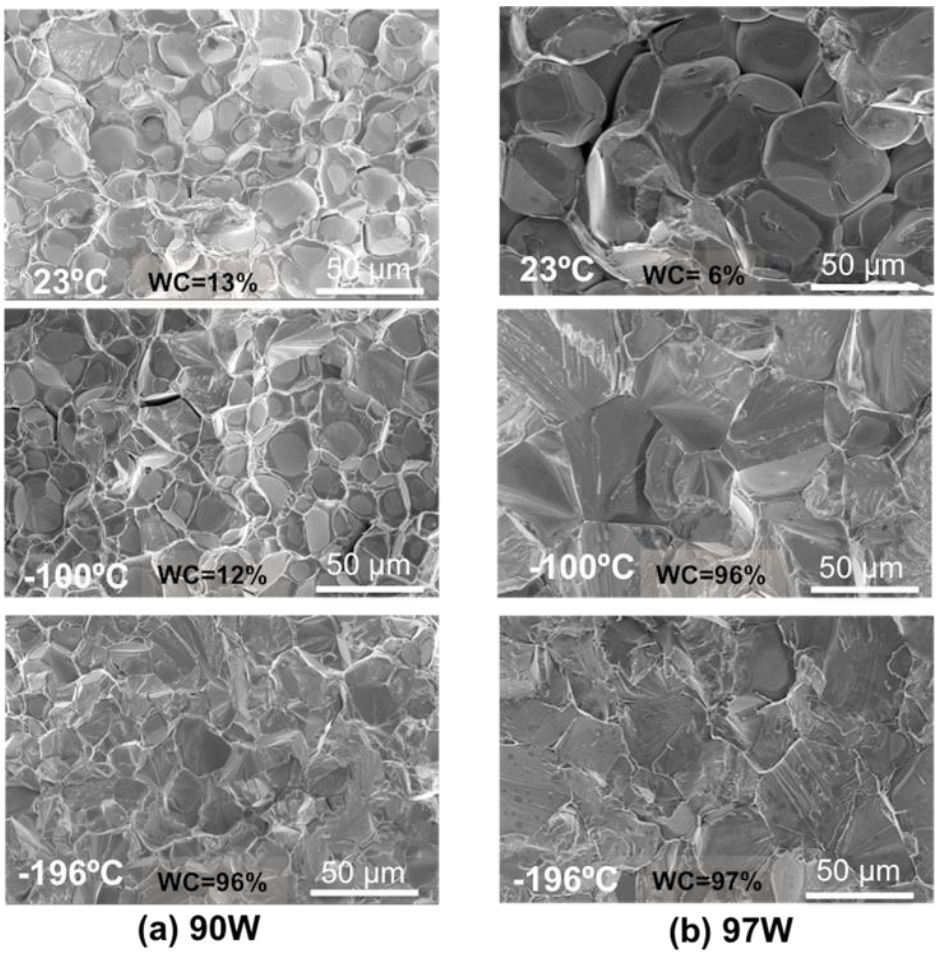

Figure 2.3.12 SEM fractographs for the: (a) 90W, and (b) 97W bend bars along with corresponding WC fraction (%) as a function of test temperature.

2.4. DAMAGE DEVELOPMENT

2.4.1 Tensile Test Damage Development

Side surface SEM observations of a 90W RT tensile specimen near the necked and fractured zone in Fig. 2.4.1a show debonding between W particles and NiWFe ductile phase (WD, white circles). This is consistent with a FEM analysis reported by Gong *et al.* [29] that shows the maximum stresses occur at the W-ductile phase (DP) interface, assuming W particles only elastically deform while the DP is subjected to isotropic hardening under a near-hydrostatic stress state during plastic deformation. Note, however, while they are strong, the W particles can also deform plastically and elongate in the loading direction when surrounded by the softer DP, as shown in Fig. 2.4.1a for the 90W WHA, and also reported in [34]. The average deformed W particle aspect ratio (PAR) along the loading direction (parallel to the marker bar, Fig. 2.4.1) increases to ≈ 1.6 ± 0.4 from a randomly oriented value of 1.1 ± 0.2 for undeformed W. Small pores, that form at the W-NiWFe interface, increase in size with loading (small and large white circles in Fig. 2.4.1a). Larger DP ligaments remain intact and arrest the microcracks (red box in Fig. 2.4.1a, also see bottom row images). WW cleavage cracks are also arrested by the DP ligaments. Isolated W particle-sized cleavage cracks are oriented over a range of angles with respect to the loading direction, presumably due to the combination of the result of Mode-I stress and the cleavage planes. Limited WW interface fracture is also observed (dashed arrows in Fig. 2.4.1a). Higher W% decreases the fraction of W particles that are completely surrounded by the DP, hence, they are less deformed (PAR ≈ 1.25 ± 0.2), as shown in Fig. 2.4.1b for the 97W WHA. W particle-sized WC microcracks, that interconnect to span several particles and WW interface fracture increase with W especially at 97W. This damage is responsible for the lower RT ductility in the higher W WHAs. Most previous studies reported that more frequent WC microcracks increase tensile ductility [30,34]. However, WC decreases ductility at high W due to the linking of

particle-sized microcracks to form a larger, unstably growing crack. In contrast to the sharp WC microcracks at 97W, (Fig. 2.4.1b, $\varepsilon_t \approx 4\%$), widely dispersed, particle-sized and highly blunted WC microcracks increase tensile ductility (Fig. 2.4.1a, $\varepsilon_t \approx 21\%$).

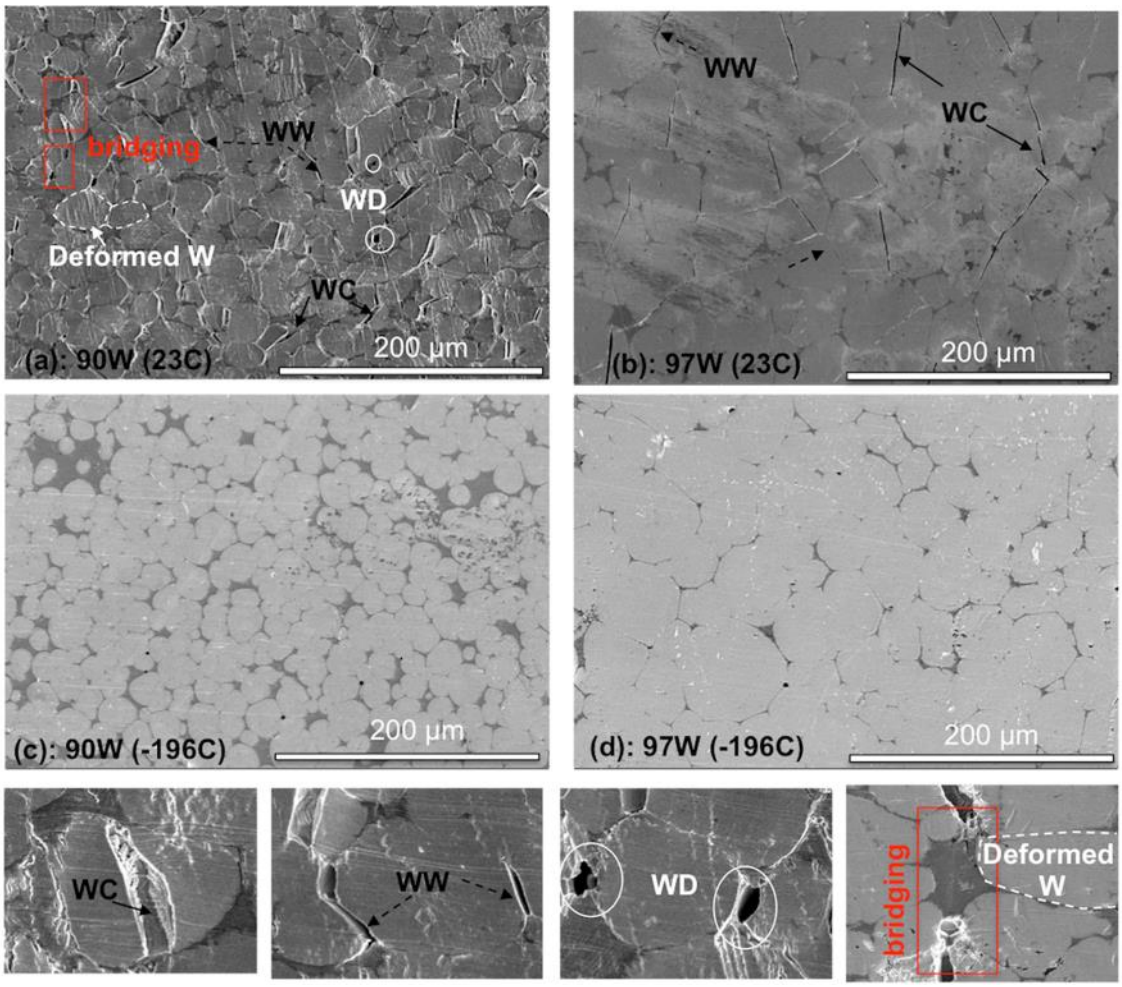

Figure 2.4.1 *SEM RT tensile specimen side views showing: (a) stable WC, WW, WD microcracking and microcrack arrest and blunting, as well as W-particle deformation near the fracture surface of the 90W alloy; (b) numerous WC and WW microcracks for 97W WHA that are less blunted; and, (c and d) largely undeformed, crack-free W-particles for 90W and 97W, respectively, tested at -196ºC that failed by elastic fracture. The bottom row of images show side-surface images of the deformation and local fracture mechanisms.*

The W particles that are far from the fracture zone deform only slightly at RT in the 90W WHA and do not deform at 97W WHA. Corresponding fractographs for the low temperature tensile tests show no arrested-blunted microcracks in all the WHA tested at -196 ºC (Fig. 2.4.1c,d) and in all the WHA with > 90W at -100ºC. Again, this is due to the rapid propagation of larger, interconnected, unarrested and largely unblunted microcracks following initiation in one grain and linking with other microcracks in adjacent grains. While WC is more frequent at lower temperatures, the propagation of the initial sharp, multi-particle crack leaves behind a population of sharp, single particle microcracks, and reduces the tensile ductility, in the limit leading to elastic fracture.

2.4.2 Fracture Test Damage Development

Side surface observations for all room temperature toughness specimens show large numbers of particle-sized WC blunted microcracks in the process-zone with a density of ≈ 556 (90W) to 231 (97W) per mm_2 (see Table 2.4.1 and Fig. 2.4.2 a,b). Some WW interface fracture and W-NiWFe interfacial debonding (WD) events are also observed. The WC microcracks might have initiated at small pores in the as-received WHA. The microcracks are arrested by the NiWFe DP and blunt under increased loading. The mid-crack opening displacements range from 0.3 to 15μm, averaging from 1.7 to 3.3μm (see Table 2.4.1). However, a few microcracks are linked up to 2 to 3 particle diameters, especially in the 97W WHA due to low amount of DP. Like in the tensile tests, both cleaved and unbroken W particles also deform along the principal stress direction. The strain in W particles normal to the loading direction, including the blunted microcracks, is again higher in the 90W WHA (≈ 0.18) compared to that in 97W WHA (≈ 0.11) (see Table 2.4.1). The small boxed areas in Fig. 2.4.3a and b show the undeformed and deformed regions at the crack tips (arrows), respectively, for the same location in a 95W WHA. The NiWFe honeycomb web is also strained normal to the loading direction (≈ 0.18 - 0.27) in all cases (DP strain in Table 2.4.1).

The WHA crack tip region also undergoes lateral contraction in the thickness (Z) direction. The ΔZ/Z was measured on the broken specimens (see Fig 2.3.6(c), for example), and verified by 3D tomography using a Keyence VHX-5000 Microscope, as shown in the insert in Figure 2.4.3(c); ΔZ/Z ≈ 0.044 ± 0.004 for 90-95W and ≈ 0.023 for 97W (Table 2.4.1). Fig. 2.4.3(d) schematically illustrates the deformation and dilatational damage mechanisms in the crack tip process zone.

Table 2.4.1 Process zone damage statistics of WHAs

WHA	Crack mouth opening (μm), Range (μm)	Crack length (μm)	Crack density (mm^{-2})	Process zone W strain (μm/μm)	DP strain (μm/μm)	ΔZ/Z	ΔV/V
90W (RT)	2.53 ± 1.82 (0.415 – 12.12)	15 ± 8	556	0.18	0.20	0.048	0.10
92.5W (RT)	1.66 ± 1.29 (0.270-7.431)	14 ± 6	387	0.17	0.23	0.044	0.09
95W (RT)	3.26 ± 2.63 (0.401 – 14.66)	33 ± 15	339	0.13	0.27	0.041	0.13
97W (RT)	2.28 ± 1.96 (3.47 – 11.69)	45 ± 19	231	0.11	0.18	0.023	0.05
90W (-100C)	1.42 ± 0.86 (0.270-5.763)	16 ± 9	376	0.09	0.17	0.039	0.07
97W (-100C)	0.27	49	4	0.00	0.01	0.00	0.00

ΔZ/Z = change in thickness/initial thickness, ΔV/V = change in volume/initial volume.

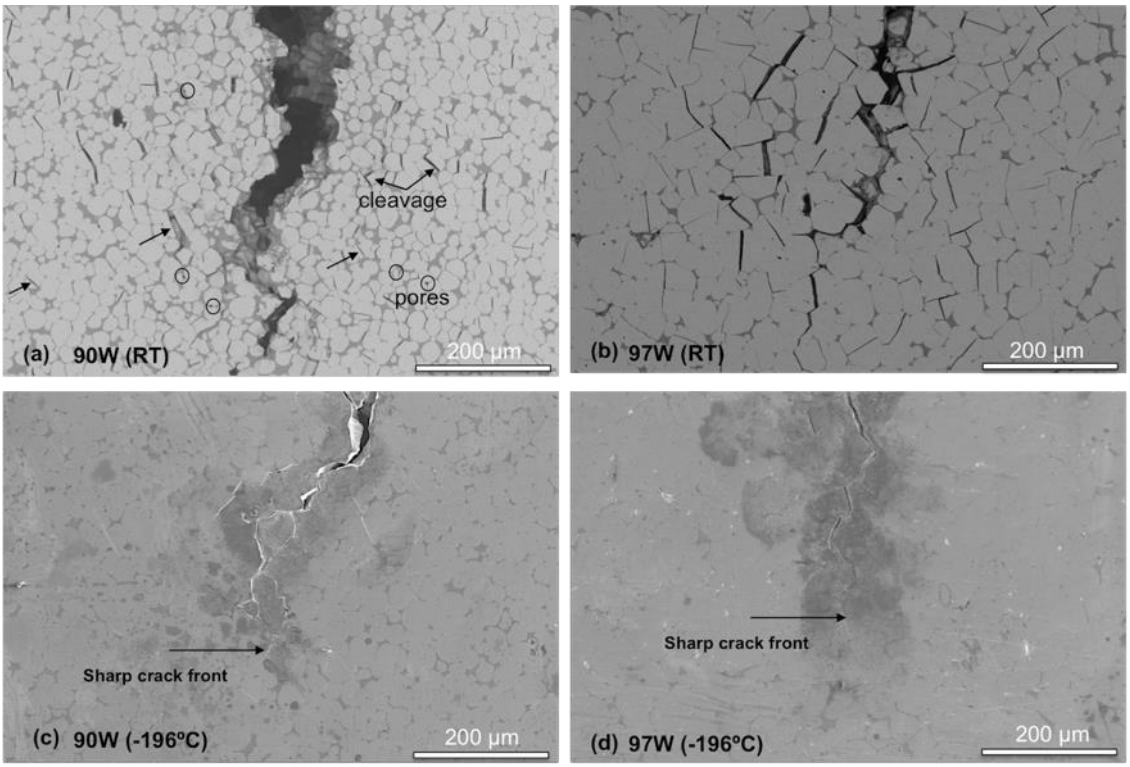

Figure 2.4.2 SEM side surface views for the: (a) 90, and (b) 97W at room temperature; and, (c) 90W, and (d) 97W at -196ºC. RT test shows numerous micro-cleavage cracks and pores, while the -196ºC test shows propagation of the macrocrack before a population of microcracks form (note, the dark region around the propagating cracks are alcohol stains).

Unlike room temperature cracks that are more frequently aligned ~ 45º to the loading direction, the lower temperature cracks are narrow and sharp and primarily aligned perpendicular to the loading direction. In this case, once initiated, adjacent microcracks link and propagate at a much lower toughness (see Table 2.3.3 and Fig. 2.4.2 c, d). In summary, the WC and WW microcracks are arrested by DP and blunt with increasing loading. The blunting dilatation decreases with increasing W and decreasing temperature.

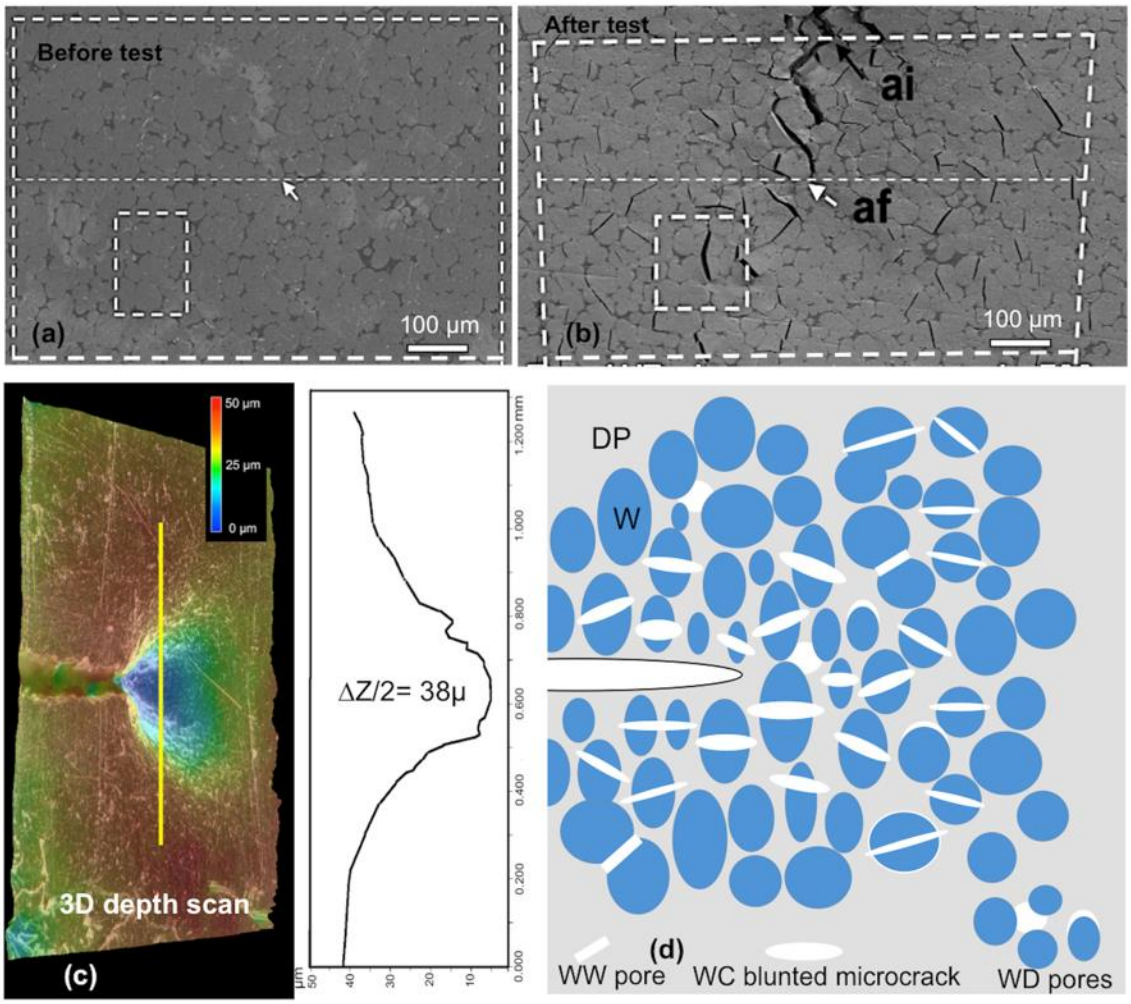

Figure 2.4.3 (a and b) Side surface views of an identical location in a 95W alloy before and after deformation, respectively, showing a large number of arrested microcracks; (c) a 3D depth scan showing the lateral contraction in a 90W alloy near the crack tip; and (d) schematic illustrating the toughening mechanisms.

2.5. DISCUSSION

The microcrack arrest and blunting mechanisms, that derive from only small amounts of the ductile NiWFe phase, lead to a remarkable W-NiFe WHA ductilization and toughening. Briefly, however, as a result of the requisite 3-dimensional flow geometry of the NiWFe honeycomb web surrounding a large volume fraction of harder W particles, deformation results in a highly triaxial

stress state in the DP and large W-NiWFe interface stresses. However, the NiWFe interface is strong, and WD local fracture modes are rare. The predominant local fracture modes are WC and WW, that produce small, particle-sized, microcracks. The small microcracks are arrested and subsequently blunted by the NiWFe DP honeycomb web (Figs. 2.3.1, 2.3.9b, 2.4.2, and 2.4.3). The web also bridges multiple coplanar microcracks that ultimately form. Thus the key ductile phase toughening (DPT) mechanism is shifted from the classical macrocrack bridging and deflection, to process zone microcrack arrest, blunting and bridging. Under these conditions, large scale bridging effects and arrest mechanisms stabilize the microcracks against propagation (see Fig. 2.3.9), in part due to the small dimensions of the W-particles and the corresponding initial microcracks (15 to 45 μ, averaging ≈ 27 ± 15 μm, see Table 2.4.1). Further, while the W particles remain encased in the DP, they can plastically deform under high stresses. However, there are limits to toughening by microcrack bridging that emerge in tests below RT and at high W, particularly in larger specimens. The primary effect of lower temperature, and these other factors, appears to be the increase in WC, leading to decreasing K_{Jm} or K_{Ic} with decreasing temperature, as illustrated in Figures 2.3.11d and 2.3.12. Here, Fig. 2.3.11(d), the average of the local fracture mode percentages for all 4 W-NiFe WHAs are plotted as a function of temperature, along with the corresponding average K_{Jm}.

It appears that the decrease in fracture toughness and transition to elastic fracture is associated with the increased brittleness of W at lower temperature leading to more initial WC microcracks, which are not as isolated in fewer and more widely-spaced W particles. The larger number of proximate co-planar microcracks link to form larger mesocracks that, in the limit, unstably propagate as an elastic fracture event. However, plastic rupture of the linked microcrack bridging ligaments still contributes to a higher WHA fracture toughness compared to monolithic W. At the lowest temperature of -196°C, co-planer microcracks quickly link to form an unstable macrocrack, thus WC in more distant W particles.

The most important consequence of this combination of micromechanisms is the large dissipation of plastic energy, partly due to the dilatational strains from the blunting microcracks, also shield the crack tip fields, greatly reducing the local stress concentrations. Thus, the process zone deformation leading to crack growth resembles, in some ways, classical microvoid nucleation (initial microcracking), growth (microcrack blunting and opening) and coaleasce (microcrack linking and unstable growth), typical of highly ductile metals and alloys, such as low alloy RPV steels.

A simple dimensional ductile fracture cohesive zone plain strain model rationalizes the observed RT WHA toughness in terms of the tensile flow stress (σ_{fl} ≈ 750 MPa), elastic modulus and Poisson's ratio (E ≈ 400 GPa and ν ≈ 0.28) and the typical critical CTOD (δ_c ≈ 35 μm) observed at crack growth initiation as [55]:

$$K_{Jc} \approx \sqrt{[2\sigma_{fl}E\delta_c/(1-\nu_2)]} \approx 151 \text{ MPa}\sqrt{m}$$

Note K_{Jc} has a contribution from the process zone dilatation, as reflected in the δ_c.

The tests at low temperature on small specimens were aimed at assessing the effects of decreases in the W-particle K_{Ic}, associated with a corresponding increases in σ_y, as well as higher crack tip stress fields. While not fully representative, the low temperature tests may partially emulate irradiation hardening at higher service temperatures. Figure 2.5.1 shows the K_{Jm} or K_{Ic} versus σ_y (T) for the 4 WHAs. K_{Jm} systematically decreases in toughness with increasing σ_y. Again, however, the WHAs are much tougher than monolithic W at RT. Assuming lower temperature is an approximate surrogate for neutron irradiation hardening, $\Delta\sigma_y$ up to 750 MPa may be tolerable in WHA plasma facing components. However, only the 90W WHA is able to avoid elastic fracture at $\Delta\sigma_y$ ≈ 550 MPa. At higher W, the corresponding hardening limit to avoid elastic fracture is $\Delta\sigma_y$ < ≈ 200 MPa.

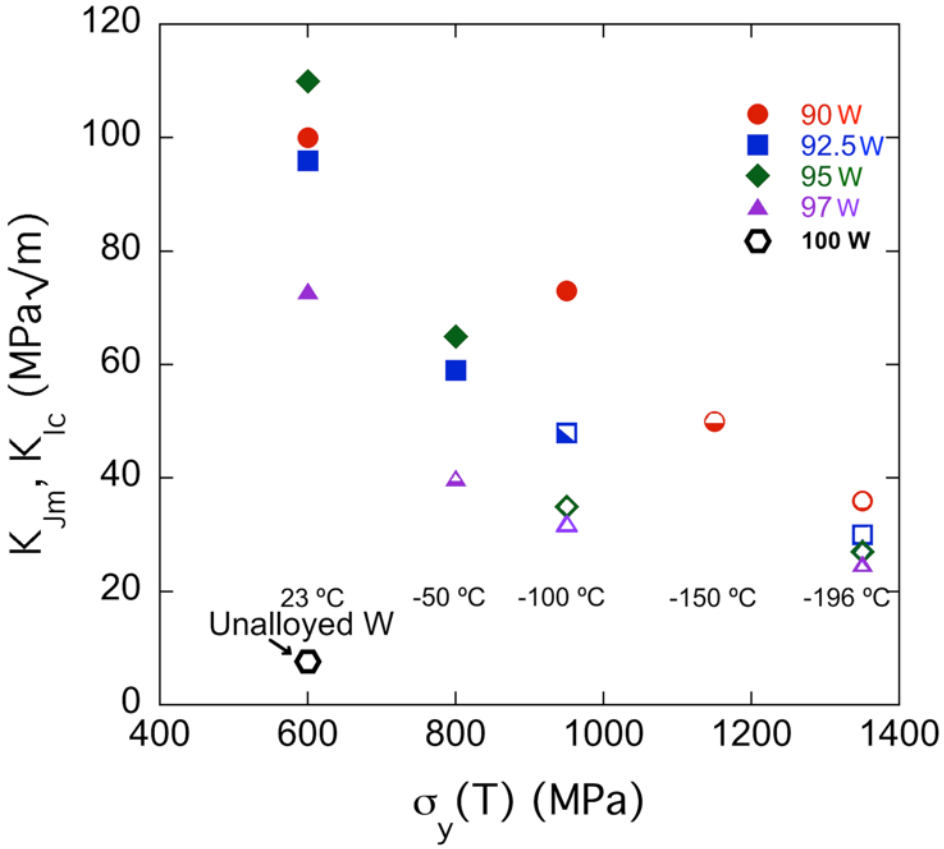

Figure 2.5.1 Toughness (K_{Jm} or K_{Ic}) versus the estimated W yield strength (σ_y) for the various WNiFe WHAs. The filled and unfilled symbols represent stable crack growth and elastic (unstable) fracture, respectively, while the half-filled symbols represent mixed stable and unstable crack growth. The K_{Ic} for monolithic (unalloyed) W is also shown.

There are numerous open questions regarding the use of W-NiFe WHA for fusion divertor applications. First and perhaps foremost, Ni is not a low activation element allowed in the class of normal reduced activation ferritic-martensitic steels. Thus the system level tolerance for limited amounts of Ni should be assessed. Further, these alloys will almost certainly be part of hybrid materials components, perhaps serving an intermediate crack arrest function like in a monolithic W:W-NiFe:ODS steel:Cu multilayer. The opportunities for using graded systems and additive manufacturing techniques for component fabrication are obvious. Other issues include

temperature limits, phase stability, irradiation effects, DP and interface strength at higher temperature including in the creep regime, and integrated thermal-mechanical durability in the presence of high temperatures and time-varying very intense heat fluxes.

2.6 CONCLUSIONS

Comprehensive mechanical property characterization tests, including microhardness, tensile and fracture toughness, were conducted on a series of W-NiFe WHAs from 23°C down to -196°C. The key results and conclusions can be summarized as follows:

- Following LPS, roughly spherical W particles are surrounded by a honeycomb web of a 50Ni30W20Fe (wt.%) solid solution DP. The reacted W particle size increases from ~17μm to ~ 38 μm and DP area percentage decreases from ~16% to ~6% between 90W and 97W with local inhomogeneity. The NiWFe DP thickness, t ≈ 4.9 ± 4.6 μm, is similar in all cases. The frequency of W-W bonded particles increases with increasing W.
- The average microhardness (H_v) at RT only slightly increases with increasing W fraction from 321 ± 9 kg/mm^2 for 90W to 344 ± 9 kg/mm^2 for 97W. The corresponding H_v almost doubles at -196°C, increasing from 507 ± 7 to 609 ± 21 kg/mm^2 between 90W and 97W.
- The RT σ_y does not vary significantly with increasing W. However, σ_u as well as the uniform and total elongations ($\varepsilon_u \approx \varepsilon_t$) systematically decrease with higher W%. The σ_y and σ_u increase and ε_t decrease with decreasing temperature. Elastic fracture ($\varepsilon_t = 0\%$) occurs at -100ºC for alloys with ≥ 95W and in all the W-NiFe WHAs at -196 ºC.
- The RT fracture toughness for small specimens of 90 to 95W WHA alloys averages $K_{Jm} \approx$ 100 ± 15 MPa√m, and decreases to 69 ± 12 MPa√m at 97W. However, this is still ≈ 9x higher than that of typical monolithic W, with a nominal $K_{Ic} \approx 8 \pm 4$ MPa√m. Extensive stable crack growth occurs in all the small specimen alloys tested at RT.

- While there are multiple toughening mechanisms, the dominant effects of the DP is plasticizing the crack tip process zone including deformation of the normally brittle W particles, and dilatational energy dissipation and shielding, both due to stable arrested microcrack blunting.
- Low-temperature fracture toughness tests on small specimens were carried out down to -196 °C, to partly emulate irradiation hardening. K_{Jm} systematically decreases with decreasing temperature and increasing W. Transitions from stable crack growth to linear elastic fracture are approximately -150ºC, -100ºC, -75ºC and -25ºC for 90W, 92.5W, 95W and 97W, respectively. The K_{Jm} at this transition averages ≈ 50 ± 5 MPa√m which is much higher that the elastic K_{Ic} ≈ 8 MPa√m
- Even at 97W, the WHA is fully ductilized at RT for tensile and small fracture specimens.
- Much more work is needed to model the micromechanics of fracture in WHA.
- Additional experimental and modeling research effects of size and geometry on the fracture of WHA is needed, but are beyond the scope of this paper.
- There are many outstanding issues regarding the use of W-NiFe WHA in divertor applications. While these topics are beyond the scope of this paper, the database and insights developed here provide the foundation for future progress.

REFERENCES

[1] M. Rieth, S.L. Dudarev, S.M. Gonzalez De Vicente et al, Recent progress in research on tungsten materials for nuclear fusion applications in Europe, J. Nucl. Mater. 432 (2013) 482–500.

[2] P. Norajitra, R. Giniyatulin, W. Krauss, V. Kuznetsov, I. Mazul, I. Ovchinnikov, J. Reiser, M. Rieth, V. Widak, Current status of He-cooled divertor development for DEMO, Fusion Eng. Des. 84 (2009) 1429–1433.

[3] V. Philipps, Tungsten as material for plasma-facing components in fusion devices, J. Nucl. Mater. 415 (2011) S2–S9.

[4] J. Davis, V. Barabash, A. Makhankov, L. Plöchl, K. Slattery, Assessment of tungsten for use in the ITER plasma facing components, J. Nucl. Mater. 258–263 (1998) 308–312.

[5] C. Henager Jr, W. Setyawan, T. Roosendaal, N. Overman, B. Borlaug, E. Stevens, K. Wagner, R. Kurtz, G.R. Odette, B. Nguyen, K. Cunningham, Ductile-phase toughened tungsten for plasma-facing materials in fusion reactors, Int. J. Powder Metall. 53 (2017) 53–69.

[6] J. Reiser, J. Hoffmann, U. Jäntsch, M. Klimenkov, S. Bonk, C. Bonnekoh, M. Rieth, A. Hoffmann, T. Mrotzek, Ductilisation of tungsten (W): On the shift of the brittle-to-ductile transition (BDT) to lower temperatures through cold rolling, Int. J. Refract. Met. Hard Mater. 54 (2016) 351–369.

[7] B. Gludovatz, S. Wurster, A. Hoffmann, R. Pippan, Fracture toughness of polycrystalline tungsten alloys, Int. J. Refract. Met. Hard Mater. 28 (2010) 674–678.

[8] A.A.N. Németh, J. Reiser, D.E.J. Armstrong, M. Rieth, The nature of the brittle-to-ductile transition of ultra fine grained tungsten (W) foil, Int. J. Refract. Met. Hard Mater. 50 (2015) 9–15.

[9] L. Veleva, Contribution to the production and characterization of W-Y , W-Y2O3 and W-TiC materials for fusion reactors, PhD Thesis, Ec. Polytech. Fed. Lausanne, Switzarl. 4995 (2011).

[10] M. Battabyal, R. Schäublin, P. Spätig, M. Walter, M. Rieth, N. Baluc, Microstructure and mechanical properties of a W – 2wt .% Y2O3 composite produced by sintering and hot forging, J. Nucl. Mater. 442 (2013) S225–S228.

[11] J. Riesch, Y. Han, J. Almanstötter, J.W. Coenen, T. Höschen, B. Jasper, P. Zhao, C. Linsmeier, R. Neu, Development of tungsten fibre-reinforced tungsten composites towards their use in DEMO - Potassium doped tungsten wire, Phys. Scr. T167 (2016) 14006.

[12] A. Luo, D.L. Jacobson, K.S. Shin, Solution softening mechanism of iridium and rhenium in tungsten at room temperature, Refract. Met. Hard Mater. 10 (1991) 107–114.

[13] P.L. Raffo, Yielding and fracture in tungsten and tungsten-rhenium alloys, J. Less-Common Met. 17 (1969) 133–149.

[14] L. Romaner, C. Ambrosch-Draxl, R. Pippan, Effect of rhenium on the dislocation core structure in tungsten, Phys. Rev. Lett. 104 (2010) 1–4.

[15] W.D. Klopp, Review of ductilizing of Group VIA elements by rhenium and other solutes, 1968.

[16] W.D. Klopp, A review of chromium, molybdenum, and tungsten alloys, J. Less-Common Met. 42 (1975) 261–278.

[17] E. Tejado, P.A. Carvalho, A. Munoz, M. Dias, J.B. Correia, U. V. Mardolcar, J.Y. Pastor, The effects of tantalum addition on the microtexture and mechanical behaviour of tungsten for ITER applications, J. Nucl. Mater. 467 (2015) 949–955.

[18] P. Krautwasser, H. Derz, Influence of fast neutron fluence on the DBTT of tungsten , Austria, 1995.

[19] J. Reiser, S. Wurster, J. Hoffmann, S. Bonk, C. Bonnekoh, D. Kiener, R. Pippan, A. Hoffmann, M. Rieth, Ductilisation of tungsten (W) through cold-rolling: R-curve behaviour, Int. J. Refract. Met. Hard Mater. 58 (2016) 22–33.

[20] K.T. Venkateswara Rao, G.R. Odette, R.O. Ritchie, Ductile-reinforcement toughening in γ-TiAl intermetallic-matrix composites: Effects on fracture toughness and fatigue-crack propagation resistance, Acta Metall. Mater. 42 (1994) 893–911.

[21] G.R. Odette, B.L. Chao, J.W. Sheckherd, G.E. Lucas, Ductile phase toughening mechanisms in a TiAl-TiNb laminate composite, Acta Metall. Mater. 40 (1992) 2381–2389.

[22] M.G. Mendiratta, J.J. Lewandowski, D.M. Dimiduk, Strength and ductile-phase toughening in the two-phase Nb/Nb5Si3 alloys, Metall. Trans. A. 22 (1991) 1573–1583.

[23] L.S. Sigl, P.A. Mataga, B.J. Dalgleish, R.M. McMeeking, A.G. Evans, On the toughness of brittle materials reinforced with a ductile phase, Acta Metall. 36 (1988) 945–953.

[24] D. V. Edmonds, P.N. Jones, Interfacial embrittlement in liquid-phase sintered tungsten heavy alloys, Metall. Trans. A. 10 (1979) 289–295.

[25] B.C. Muddle, Interphase boundary precipitation in liquid phase sintered W-Ni-Fe and W-Ni-Cu alloys, Metall. Trans. A. 15 (1984) 1089–1098.

[26] A. Mondal, D. Agrawal, A. Upadhyaya, Microwave sintering of refractory metals / alloys : Microwave Sintering of Refractory Metals / alloys : W , Mo , Re , W-Cu , W-Ni-Cu and W-Ni-Fe Alloys, J. Microw. Power Electromagn. Energy. 44 (2010) 28–44.

[27] Z.A. Hamid, S.F. Moustafa, W.M. Daoush, F.A. Mouez, M. Hassan, Fabrication and characterization of tungsten heavy alloys using chemical reduction and mechanical alloying methods, Open J. Appl. Sci. 03 (2013) 15–27.

[28] M. Scapin, Mechanical characterization and modeling of the heavy tungsten alloy IT180, Int. J. Refract. Met. Hard Mater. 50 (2015) 258–268.

[29] X. Gong, J. Fan, F. Ding, Tensile mechanical properties and fracture behavior of tungsten heavy alloys at 25-1100 °C, Mater. Sci. Eng. A. 646 (2015) 315–321.

[30] K. Hu, X. Li, X. Ai, S. Qu, Y. Li, Fabrication, characterization, and mechanical properties of 93W-4.9Ni-2.1Fe/95W-2.8Ni-1.2Fe/95W-2.8Ni-1.2Fe-1Al2O3 heavy alloy composites, Mater. Sci. Eng. A. 636 (2015) 452–458.

[31] U.R. Kiran, A. Panchal, M. Sankaranarayana, G.V.S.N. Rao, T.K. Nandy, Effect of alloying addition and microstructural parameters on mechanical properties of 93% tungsten heavy alloys, Mater. Sci. Eng. A. 640 (2015) 82–90.

[32] M.B. Shongwe, S. Diouf, M.O. Durowoju, P.A. Olubambi, M.M. Ramakokovhu, B.A. Obadele, A comparative study of spark plasma sintering and hybrid spark plasma sintering of 93W-4.9Ni-2.1Fe heavy alloy, Int. J. Refract. Met. Hard Mater. 55 (2016) 16–

23.

[33] R. German, J. Hanafee, S. DiGiallonardo, Toughness variation with test temperature and cooling rate for liquid phase sintered W-3.5Ni-1.5Fe, Metall. Trans. A. 15 (1984) 121–128.

[34] K.S. Churn, R.M. German, Fracture behavior of W-Ni-Fe heavy alloys, Metall. Trans. A, Phys. Metall. Mater. Sci. 15 A (1984) 331–338.

[35] D. V Edmonds, Structure/property relationships in sintering heavy alloys, Refract. Met. Hard Mater. 10 (1991) 15–26.

[36] R.M. German, A. Bose, S.S. Mani, Sintering time and atmosphere influences on the microstructure and mechanical properties of tungsten heavy alloys, Metall. Trans. A. 23 (1992) 211–219.

[37] K.M.O. Zamora, J.G. Sevillano, M.F. Perez, Fracture toughness of W heavy metal alloys, Mater. Sci. Eng. A. 157 (1992) 151–160.

[38] A. Upadhyaya, Processing strategy for consolidating tungsten heavy alloys for ordnance applications, Mater. Chem. Phys. 67 (2001) 101–110.

[39] Z.H. Zhang, F.C. Wang, S.K. Li, L. Wang, Deformation characteristics of the 93W-4.9Ni-2.1Fe tungsten heavy alloy deformed by hydrostatic extrusion, Mater. Sci. Eng. A. 435–436 (2006) 632–637.

[40] S. Islam, X. Qu, X. He, Investigation of composition and microstructure effect on fracture behaviour of tungsten heavy alloys, Powder Metall. 50 (2007) 11–13.

[41] Y. Şahin, Recent progress in processing of tungsten heavy alloys, J. Powder Technol. 2014 (2014) 1–22.

[42] R. Neu, H. Maier, M. Balden, S. Elgeti, H. Gietl, H. Greuner, A. Herrmann, A. Houben, V. Rohde, B. Sieglin, I. Zammuto, Investigations on tungsten heavy alloys for use as plasma facing material, Fusion Eng. Des. 124 (2017) 450–454.

[43] R. Neu, H. Maier, M. Balden, R. Dux, S. Elgeti, H. Gietl, H. Greuner, A. Herrmann, T. Höschen, M. Li, V. Rohde, D. Ruprecht, B. Sieglin, I. Zammuto, Results on the use of tungsten heavy alloys in the divertor of ASDEX Upgrade, J. Nucl. Mater. 511 (2018) 567–573.

[44] G. V Raynor, V.G. Rivlin, Phase equilibria in iron ternary alloys: Critical evaluation of constitutions of certain ternary alloys containing iron , tungsten , and a third metal, Int. Met. Rev. 26 (1981) 213–249.

[45] J.H. You, Design feasibility study of a divertor component reinforced with fibrous metal matrix composite laminate, J. Nucl. Mater. 336 (2005) 97–109.

[46] A.G. Evans, R.M. Cannon, Toughening of b rittle solids by martensitic transformations, Acta Metall. 34 (1986) 761–800.

[47] J.W. Hutchinson, Non-linear fracture mechanics, Tech. Univ. of Denmark, 1979.

[48] M. Rühle, A.G. Evans, R.M. McMeeking, P.G. Charalambides, J.W. Hutchinson, Microcrack toughening in alumina/zirconia, Acta Metall. 35 (1987) 2701–2710.

[49] A.G. Evans, Z.B. Ahmad, D.G. Gilbert, P.W.R. Beaumont, Mechanisms of toughening in rubber toughened polymers, Acta Metall. 34 (1986) 79–87.

[50] M.E. Alam, S. Pal, K. Fields, S.A. Maloy, D.T. Hoelzer, G.R. Odette, Tensile deformation and fracture properties of a 14YWT nanostructured ferritic alloy, Mater. Sci. Eng. A. 675 (2016) 437–448.

[51] ASTM E8M-15a, ASTM E8/E8M - 15a: Standard test methods for tension testing of metallic materials, in: Annu. B. ASTM Stand., ASTM International, 100 Barr Harbor Drive, PO Box C700, West Conshohocken, PA 19428-2959, United States, 2015.

[52] M.E. Alam, S. Pal, S.A. Maloy, G.R. Odette, On delamination toughening of a 14YWT nanostructured ferritic alloy, Acta Mater. 136 (2017) 61–73.

[53] ASTM E1921-03, Standard Test Method for Determination of Reference Temperature , To , for Ferritic Steels in the Transition Range, in: Annu. B. ASTM Stand., ASTM International, 100 Barr Harbor Drive, PO Box C700, West Conshohocken, PA 19428-2959, United States, 2012: pp. 1–25.

[54] ASTM C1421-16, Standard Test Methods for Determination of Fracture Toughness of Advanced Ceramics at Ambient Temperature, in: Annu. B. ASTM Stand., ASTM International, 100 Barr Harbor Drive, PO Box C700, West Conshohocken, PA 19428-2959. United States, 2016: pp. 1–33.

[55] T.L. Anderson, Fracture Mechanics: Fundamentals and Applications, 3rd ed., Taylor & Francis Group, FL, USA, 2005.

[56] M.E. Alam, S. Pal, K. Fields, G.R. Odette, Mechanical properties characterization of 90-97wt% WNiFe heavy alloys, DOE Fusion React. Mater. Progr. Semiannu. Prog. Report, 61. DOE/ER-031 (2016) 73–82.

[57] ASTM, Standard Test Method for Measurement of Fracture Toughness, ASTM Standard E1820-13, ASTM B. Stand. (2013) 1–54.

CHAPTER 3

INFLUENCE OF SPECIMEN SIZE, GEOMETRY AND LARGE IMPURITY INCLUSIONS ON THE FRACTURE TOUGHNESS OF TUNGSTEN HEAVY METAL ALLOYS

ABSTRACT

The tensile strength and fracture toughness properties of four ductile phase toughened (DPT) commercially available tungsten (W)-based heavy metal alloy composites (WNiFe), reinforced with 3 to 10 (wt.%) of a NiFe phase, were previously thoroughly characterized from room to liquid nitrogen (LN_2) temperatures. The brittle-to-ductile transition temperature (BDTT) ranged from -25ºC to -150 ºC, depending on DP content. Above this temperature the specimens fail by stable crack growth, while at lower temperature elastic fracture occurs. However, in all cases the WHA had much higher $K_{Jm/Ic}$ than monolithic W. Here we study specimen size and geometry effects on $K_{Jm/Ic}$. We find a general trend that larger specimen sizes and less compliant geometries have lower $K_{Jm/Ic}$, depending on the amount of DP. RT fracture toughness was also conducted on a 95W-3.5Ni-1.5Cu alloys to understand the effect of the ductile phase properties (Cu vs. Fe) on toughness.

3.1 INTRODUCTION

Due to high melting temperature, good conductivity, low sputtering rate and high-temperature strength, tungsten (W), and its alloys, are currently considered the most promising candidates for plasma facing component for future fusion reactor divertor applications [1-4]. This application requires that structural W-based alloys and structures have sufficient fracture toughness to withstand the severe thermal-mechanical environment of a divertor. It is likely that monolithic W is intrinsically too brittle for this task. Previously a series of WNiFe (90, 92.5, 95 and

97 wt.% W with 7:3 = Ni:Fe) heavy metal alloys were shown to have much higher room temperature toughness (> 9x) and much lower BDTT temperatures (-150 to -25 ºC) than monolithic W (several hundred °C), depending on their ductile phase NiFe content [5-6]. However, these results are for relatively small specimens (thickness, B= 1.65 mm; W= 2B; S= 4W). Though these results are largely consistent with the ASTM E-1921 standard validity criteria due to the high yield strength and elastic moduli of the WHA, however, due to the complex physics of process-zone microcracking toughening, we have conducted toughness test on different size specimens, 3x to 8x larger and thicker than the base/small specimen at room temperature. Ductile phase (DP) area % was measured from the tested specimens and this along with DP ligament thickness were correlated to $K_{Jm/Ic}$. RT fracture toughness test on compact specimen (CT) for the 95W alloy were also performed to investigate the effect of specimen geometry. Further, we have repeated RT 3PB tests on a new alloy composition that contains 1.5Cu, instead of 1.5Fe for 95W WHA, to understand the effect of the ductile phase properties. Microstructural characterization, microhardness and tensile tests, all were also performed on this Cu-reinforced 95WNiCu WHA alloy.

3.2 EXPERIMENTAL PROCEDURES

Five commercial (Mi-Tech Metals, Indianapolis, IN, USA) liquid-phase sintered (LPS) tungsten heavy metal alloys (WHA) were received in the form of plates. Out of five, four of the WHAs contained 90, 92.5, 95 and 97 wt. % W with a balance of an initially 70% Ni and 30 %Fe phase, while the other one is 95W-3.5Ni-1.5Cu (wt.%). As discussed in Chapter-2 for small specimens (B= 1.65mm), the E1921 testing validity limit of K_{Jlim} ranged from 120 to 132 MPa$\sqrt{m}$, which is larger than any of the K_{Jm} values. The implication is that cleavage initiation in these specimens is possible, but ductile tearing occurred at an even lower K_{Jc} due to the ductile phase toughening mechanisms operating in the crack tip process zone. However, size effects are: i)

manifested by different mechanisms, including statistical effects; ii) the E1921 constraint loss limits may be too permissive (unconservative); and, iii) the physics of process zone fracture in WHA may differ from that in steels. Therefore, here, we have tested a limited number of 3PB specimens up to 8 times larger (B ≈ 12.7 mm, W = 2B) than the small baseline bend bars. Other than the difference in size for 3PB bend bars, all the specimen preparations, characterization tools and analyzing procedures are same and can be found in Ref. [5-6]. The CT specimens were prepared from the broken 6x larger 3PB bars of 95W. The dimensions of CT specimen are shown in Fig. 3.2.1. Like 3PB specimens, the CT specimens are also precracked to a/W ≈ 0.4- 0.5, and tested and analyzed as per ASTM standard E-1921 [7].

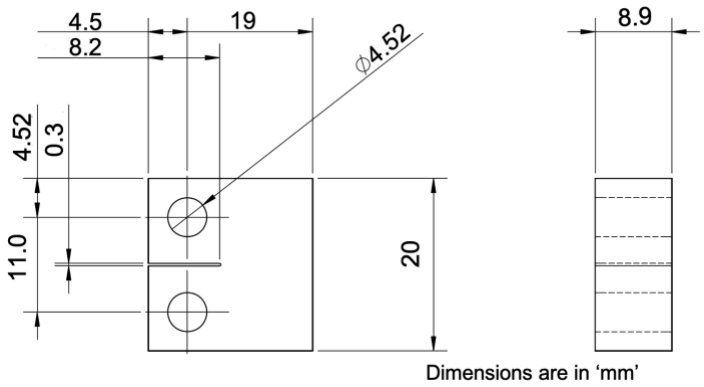

Figure 3.2.1 The compact tension (CT) specimen dimensions.

3.3 RESULTS AND DISCUSSION

3.3.1 Specimen Size Effect on Room Temperature Fracture Toughness

We have previously reported microstructural, tensile and fracture toughness (K_{Jm}) properties of small specimens from room temperature (RT) to liquid nitrogen (LN_2) temperature, and can be found elsewhere [5-6]. The RT K_{Jm} tests using to dimensions of 16x3.3x1.65 mm are nominally valid per ASTM E-1921. However, for reasons described previously, we also tested a limited number of specimens that are approximately 3, 6 and 8 times larger, which we describe

as medium (M = 45x10x5mm), large (L = 90x20x10mm), and extra-large (XL = 115x25.4x12.7 mm, or 0.5T ASTM standard size) specimens, respectively. Note, like the small specimens, these were also fatigue precracked to a nominal a/W = 0.45-0.5. Four specimens were tested for all conditions at RT. Normalized to a/W= 0.5 for load, P_n = 0.25P/{(1-a/W)$_2$}, the RT load-displacement (P_n-d) curves for 3x larger specimens are shown in Fig. 3.3.1. However, representative normalized load-displacement (P_n-d_n) curves for all specimens are shown in Fig. 3.3.2a. In this case, load is normalized following ASTM E-1820-A15 [8], by applying P_n = P/{WB(1-a/W)$_2$} which is valid up to maximum load point (P_m), as a/W increase after P_m; while the displacement is normalized simply diving their corresponding load-line displacement by the factor of specimen thickness (i.e. 1 for small, 3 for medium specimens and so on). Note, all the P_n-d_n curves, shown in Fig. 3.3.2a, for different sized specimens are only for comparison purpose, and not for calculating R-curves. Their corresponding K_{Jm} values are plotted in Fig. 3.3.2b, and also summarized in Table 3.3.1.

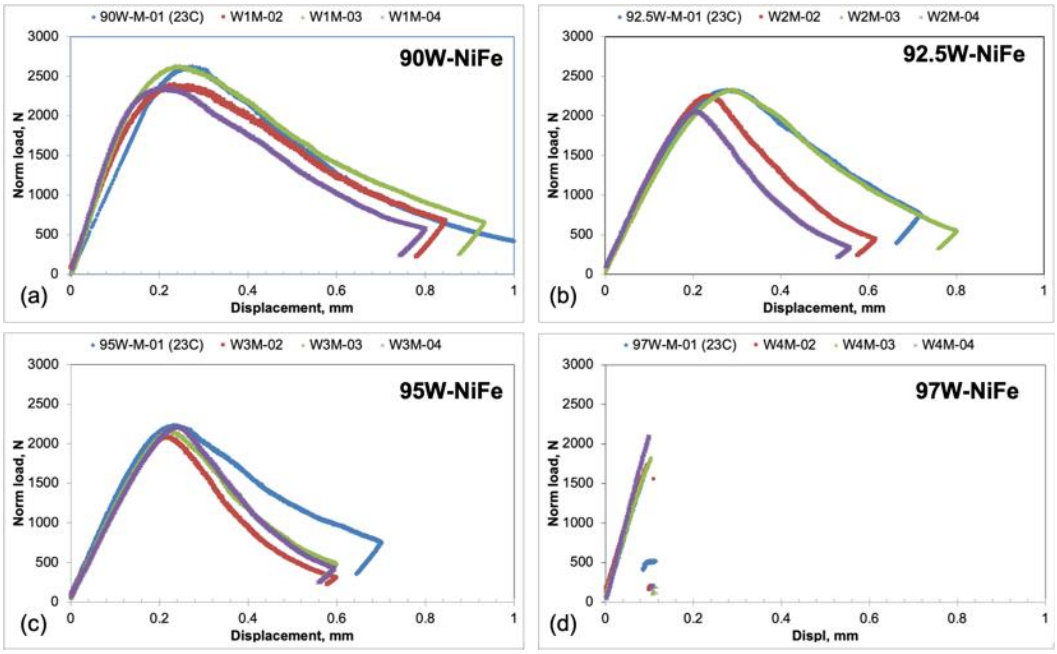

Figure 3.3.1 Normalized for a/W = 0.5, RT load-displacement (P-d) curves for medium-sized WNiFe WHA alloys of: (a) 90W; (b) 92.5W; (c) 95W; and, (d) 97W, respectively.

All the medium-sized (B= 5mm) specimens, except 97W, show stable crack growth (see Fig. 3.3.1). The K_{Jm}, slightly decreases with increasing B and W loading up to 95W; and noticeably decreases for 97W with an average $K_{Ic} \approx (38 \pm 4\ MPa\sqrt{m})$. Note, the differences between the small and medium specimen K_{Jm} is larger at 95W, but this is primarily due to the deviation of the small specimen K_{Jm}, which is large due to local microstructural inhomogeneity (see Fig. 2.3.2 of Chapter 2).

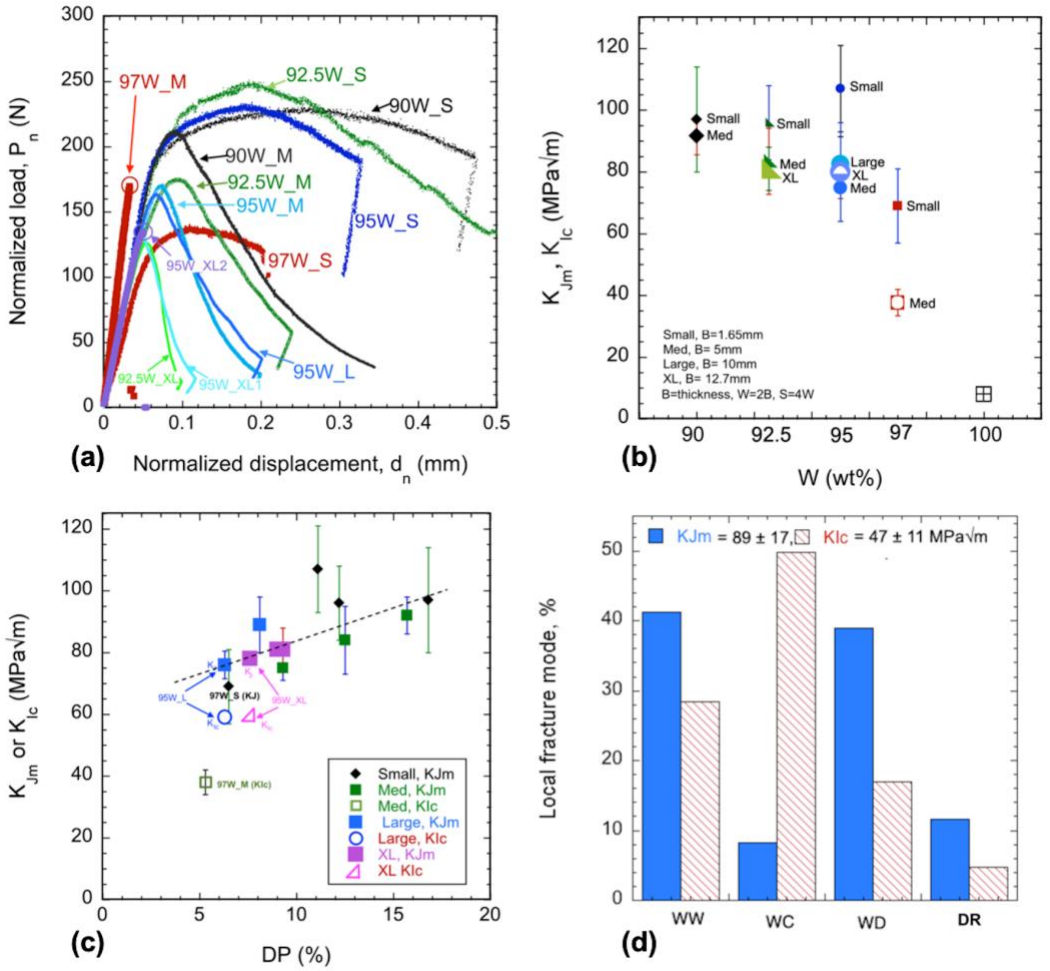

Figure 3.3.2 Room temperature: (a) normalized P_n-d_n curves showing stable crack growth all alloys and sizes except 97W_med and one of 95W_XL specimens; (b) K_{Jm} or K_{Ic} values as a function of W% and specimen sizes; (c) fracture toughness as a function of DP%; and (d) local fracture modes for stable vs unstable crack growth.

Table 3.3.1 The room temperature K_{Jm} for the (90-97)W-NiFe and 95W-NiCu WHAs

Specimen size	K_{Jm} or K_{Ic} (MPa√m)				
	90W	92.5W	95W-NiFe	95W-NiCu	97W
Small	97 ± 17	96 ± 12	107 ± 14	-	73 ± 13
Med	92 ± 6	84 ± 11	75 ± 4	50 ± 6	38 ± 4
Large	-	-	82 ± 9	45 ± 1	-
XL	-	81 ± 7	80 ± 3	-	-
CT-0.35T	-	-	63 ± 8	-	-

*small: B= 1.65mm; med: B = 5mm; large: B= 10mm; XL: B= 12.7mm. W= 2B; S= 4W; Length =4.5W.

As shown in Table 3.3.2, the variation in average local fracture modes is minimal for the different size specimens for up to 95W. Unlike small 90-97W specimens (or medium specimens up to 95W), all the medium 97W specimens experience elastic fracture. The fractions of local fracture modes are also found different for the medium 97W specimens (see Table 3.3.2 and Fig. 3.3.3). In this case, the WC local fracture mode jumps from ≈ 18% to almost 60%.

Table 3.3.2 The percentage of local fracture modes from RT toughness fractographs

WHA's	**Specimen Size**	**WW**	**WC**	**WD**	**DR**
90W	Small	31.7	12.0	44.1	12.2
	Medium	45.1	3.4	36.2	15.3
92.5W	Small	37.1	10.9	40.5	11.5
	Medium	41.2	4.1	42.4	12.3
	XL	32.5	2.4	47.2	17.9

95W	Small	42.6	13.5	32.8	11.1
	Medium	48.4	8.6	34.0	9.0
	Large	33.3	6.5	46.9	13.3
	XL	33.4	3.7	53.7	9.2
97W	Small	67.2	17.6	10.8	4.4
	Medium	33.4	57.1	8.7	0.8

WW = W-W separation, WC= W-cleavage, WD= W-DP interface decohesion, DR= ductile rupture.

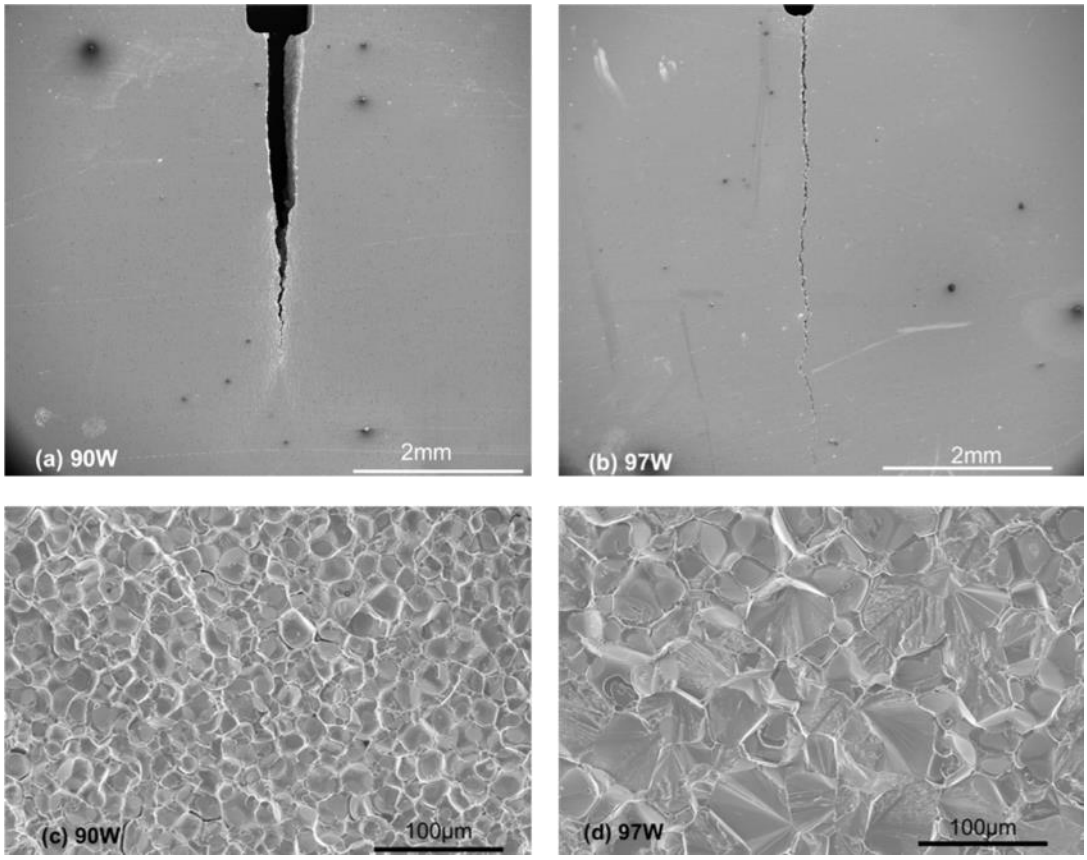

Figure 3.3.3 Low magnification SEM images showing stable and unstable crack propagation for the medium size RT toughness specimens of: (a) 90W, and (b) 97W alloys, respectively. (c) and (d) are showing their respective higher magnification SEM images that reveals mix of all local fracture modes for 90W, and WC dominating facture for 97W.

Most literature results, based on tensile test data, claim that the higher WC fractions are associated with larger tensile ductility. However, in the case of fracture toughness test, we find an opposite trend, that for larger WC associated with lower K_{Jm}. Note, WC fraction is also somewhat higher for smaller 97W compares to the other WHA alloys (see Table 3.3.2). This observation is also consistent with the lower temperature K_{Jm}/K_{Ic}, discussed in Chapter 2.

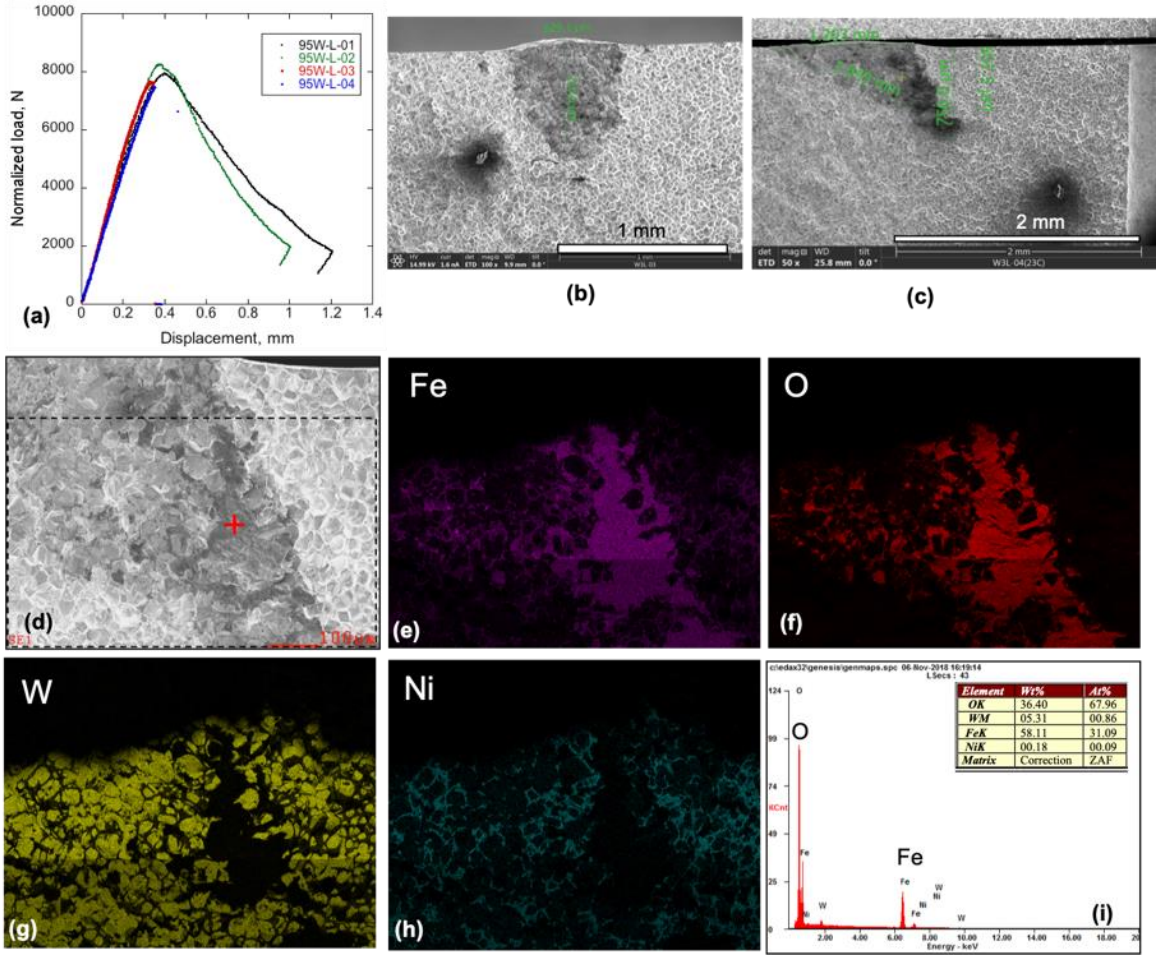

Figure 3.3.4 Images showing: (a) RT P-d curves for large 95W (B=10mm) specimens, normalized to a/W=0.5. Two of them show stable and other two show elastic fracture; (b-c) fractured surfaces with oxide inclusions (~1000μmx750μm) at the crack tip for the two elastically fractured specimens; and, (d-i) EDX mapping and point scan confirm oxide inclusions.

We have also tested 6x and 8x large specimens. Out of four RT tests, two of the 6x large (B ≈ 10mm) 95W specimens show ductile tearing, but other two fractured unstably at yielding (see Figure 3.3.4a). Big oxide inclusions (~1mm x 0.7mm) near the pre-crack tip were found in both brittle specimens, and are likely the cause for the unstable crack propagation (see Fig. 3.3.4). However, the DP area% from the side surface of these large 95W alloys are found ≈ 8% (for stable) and ≈ 6% (for unstable fracture), that are lower than the average DP% ≈ 11% for the same plate (see Table 3.3.3), might be another reason for unstable crack propagation. In spite of elastic fracture in these 2 specimens, all four specimens show reasonably similar toughness that averaged ≈ 82 ± 9 MPa√m, that fell within the standard deviation range between the small and medium 95W K_{Jm}. Note, the local fracture modes for 95W RT tests showing ductile tearing are nearly similar, only slightly decreases WC% and increases WD% with increasing specimen size (see Table 3.3.2).

Table 3.3.3 Relationship among the specimen size, DP area percentage, toughness and crack propagation modes of all tested WHA alloys

WHA alloy/ specimen size	**DP %**	**K_{Jm}, MPa√m**	**K_{Ic}, MPa√m**	**Crack propagation mode**
90W_S	16.8	97		stable
92.5W_S	12.2	96		stable
95W_S	11.1	107		Stable
97W_S	6.5	69		stable
90W_M	15.7	92		stable
92.5W_M	12.5	84		stable
95W_M	9.3	75		stable
97W_M	5.3	-	38	unstable

95W_L	8.1	89		stable
95W_L	6.3	76	59	unstable
92.5W_XL	9.3	81		stable
95W_XL	9.0	82		stable
95W_XL	7.6	78	60	unstable

Due to the materials limitation and fabrication cost, only 2 XL size (≈ 8x, ASTM standard 0.5T) specimens from each of 92.5W and 95W WHA were fabricated, precracked, and tested at RT using 3PB frame. While both the 92.5W XL specimens shows stable crack growth; however, one of the 95W XL fails unstably, and the other one shows stable crack propagation (see Fig. 3.3.2a). Note, these specimens were fabricated from second batch of plate which shows lower average DP% than their respective first batch, for example, DP% for 95W is ≈ 11 and ≈ 9%, for 1_{st} and 2_{nd} batch, respectively. Due to the microstructural variation for specimens to specimen, DP area% has been calculated from the tested specimens and its correlation with toughness has been plotted in Fig. 3.3.2.c (also tabulated in Table 3.3.3). The average local fracture modes, irrespective of specimen size or alloy compositions, have also been calculated based on stable versus unstable crack propagation and plotted in Fig. 3.3.2d. Since 8x large 92.5W specimens show stable and 3x large 97W specimens show unstable crack propagation, therefore, further tests after 3x large specimens has not been conducted for 90W and 97W for obvious results.

3.3.2 Damage Mechanisms

Like the smaller RT specimens, all the 3x, 6x and 8x larger size specimens, except 3x larger 97W and one of 8x elastically fractured 95W specimens, show fairly similar side surface toughening mechanisms (see Figure 3.3.5) as for room temperature small specimens (see Fig. 2.4.2 of Chapter 2).

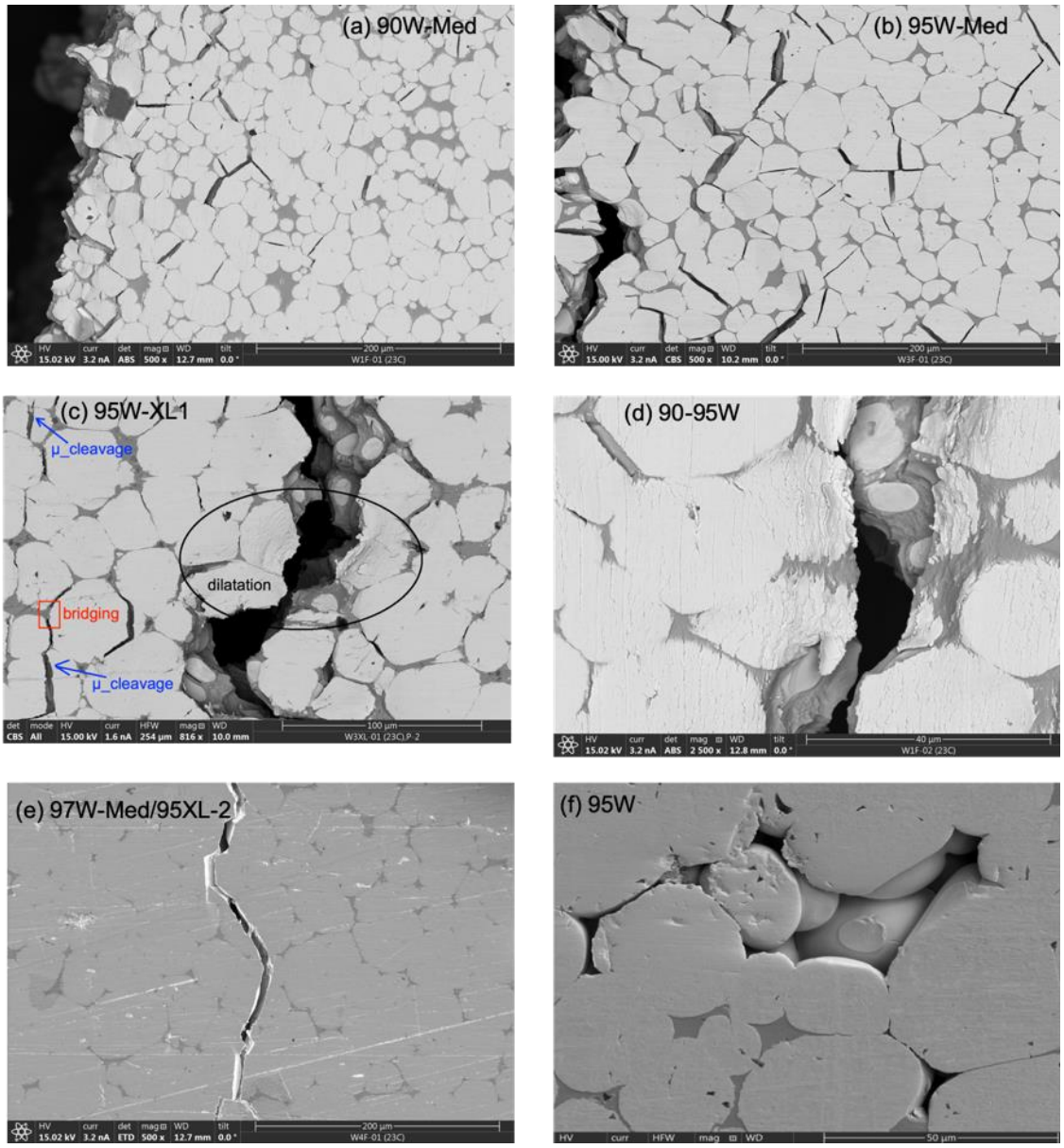

Figure 3.3.5 SEM images showing side-surface damage mechanisms for the: (a) 90W_medium; (b) 95W_medium; and (c) 95W_XL size specimens revealing micro-cleaved W-particles observed in the side surface that are arrested and blunted by the DP phase. (d) showing numerous amounts of slip lines in the W-particles, aligned perpendicular to the principal stress direction, helps to dissipate strain energy by dilatating particles and DP phase for the 90 to 95W alloys; and, (e) shows very sharp crack propagation for medium size 97W specimens or one of 95W_XL size specimen, without affecting the nearby W-particles, like -196ºC tests for smaller specimens. Fig (f) shows weak or no bonding between W and DP phase observed for some 95W undeformed plate.

W-particles are cleaved remotely, arrested and blunted by the DP at the process zone for up to 95W (Fig. 3.3.5a-c). Many individual W particles are highly strained (see parallel slip lines on W particles) in the principal stress directions prior to fracture (see Fig. 3.3.5d). However, more WC linkage occurs in the larger versus the smaller specimens, and increases with higher W up to 95W (see Figs. 3.3.5 and 2.4.2 of Chapter 2). In contrast, there is no distributed process-zone microcracking in the medium sized 97W or one of elastically fractured extra-large 95W specimens (see Fig. 3.3.5e). In this case, a single crack propagates, linking with co-planar microcracks resulting in immediate elastic fracture. Along with lower DP%, weak or no interfacial bonding between W-particles and DP phases were also observed in some cases, especially for some 95W alloy plate, before deformation, that might also cause for the elastic fracture of larger specimens (Fig. 3.3.5f).

3.3.3 Specimen Geometry Effect

Modified 0.35CT (or thickness ≈ 9 mm, see Fig. 3.1) specimens were fabricated from the tested large 3PB bars halves to ensure maximum utilization of materials. The P-d curves for CT specimens show most of the specimens developed unstable crack propagation after reaching maximum load (Fig. 3.3.6a). The average K_{Jm} or K_{Ic} is lower than the other 95W specimens tested in 3 or 4PB bending. Only limited process-zone microcracking was observed (Fig. 3.3.6b), and the overall plastic process zone is much smaller than for the ductile tearing 95W. SEM image from the fractured surfaces also reveals that the W-W particle separation and W-DP decohesion dominate the local fracture modes (Fig. 3.3.6c). A lower amount of DP%, combined with weak, or no, W-DP interfacial bonding (Fig. 3.3.6c,d) might be affecting the P-d behavior. System compliance might play a role for stable vs unstable crack propagation for 3PB large vs, CT specimens. Note, there was less tungsten cleavage (WC) in these CT specimens, which is normally a dominating factor for unstable crack propagation.

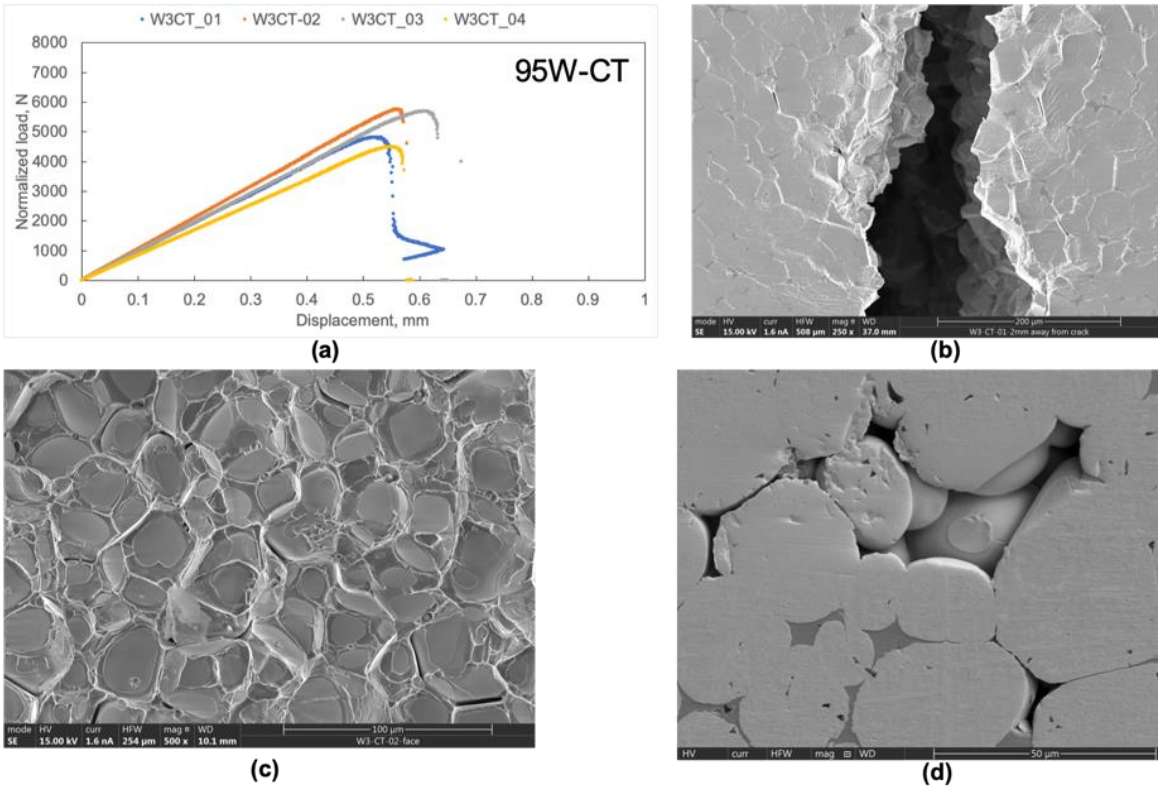

Figure 3.3.6 (a) Normalized load for a/W ≈0.5, the P-d curves for the room temperature CT specimens; (b) side surface shows limited plastic process zone; (c) SEM fractograph shows WW and WD dominations; and (d) absence of DP between W particles, and at the surface that might be scruff off during mechanical polishing (due to weak interfacial bonding). Note, the image is from the unloaded sample, and not chemically etched.

3.3.4 Larger Impurity Inclusion Effects on the Microstructural and Mechanical Properties

Like WNiFe WHAs, WNiCu are widely used for similar applications. Therefore, we have conducted room temperature fracture toughness test on medium and large specimens on a 95W-3.5Fe-1.5Cu (wt.%) WHA following ASTM standard E-1921. We have also conducted basic microstructural, along with hardness and room temperature tensile tests. For the simplicity, unless otherwise stated, we now will address these 95W-3.5Ni-1.5Fe and 95W-3.5Ni-1.5Cu alloys as NiFe and NiCu WHA, respectively.

3.3.4.1 Microstructure

The SEM micrographs of the polished and etched 95W-NiFe and 95W-NiCu plates shown in Fig. 3.3.7 reveal roughly spheroidal W particles (particle aspect ratio (PAR): 1.1 ± 0.2 for NiFe and 1.3 ± 0.3 for NiCu) surrounded by the interconnected honeycomb web structure of the ductile NiWFe and NiWCu phases, respectively. Multiple energy dispersive X-ray spectroscopy (EDS) scans show that the particles are close to 100% W in both plates. However, while the NiWFe ductile phase (DP) is approximately 50%Ni, 30%W and 20%Fe (wt.%), the NiWCu DP is ~50%Ni, 40%W and 10% Cu (see Table 3.3.4 and Fig. 3.3.8).

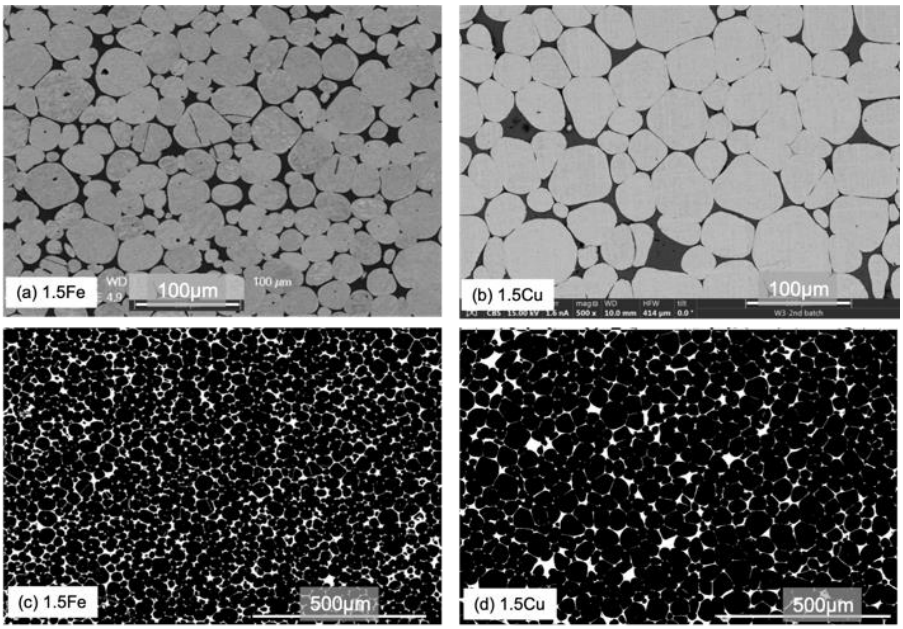

Figure 3.3.7 The SEM images of the W particles (gray) and the ductile NiWFe phase (dark) for: (a) NiFe 95W; and (b) NiCu 95W WHA, respectively. The binary black (W) and white (DP) images of: (c) NiFe, and (d) NiCu highlight the NiWFe and NiWCu honeycomb web, respectively. Note, W particles are smaller and relatively uniformly dispersed in the NiWFe DP (Fig. c), however, they are relatively larger and form W clusters (minimal/ no white DP between W-particles) and pools of NiWCu DP phases (larger white area) for NiCu WHA (Fig. d).

Fig. 3.3.7 and Table 3.3.3 also show that the W–particles are larger for NiCu WHA than the NiFe WHA (38µm vs 27µm). W-W contiguity also increases for NiCu WHA, while NiWCu DP area

fraction; DP web thickness, t; and t/d; all decreases compared to the NiFe WHA (Table 3.3.3). It is also very interesting to note that, while the smaller W-particles (black particles in Fig. 3.3.7c) are relatively well dispersed in the NiWFe DP phase (white in Fig. 3.3.7c) in the NiFe WHA, relatively larger W-particles for NiCu WHA are arranged in a cluster-like fashion (minimal white space between W-particles), and forms pools of DP-phases (larger white area in Fig. 3.3.7d). That is, there is a heterogeneous distribution of W in DP phase.

Table 3.3.4 The size and contiguity of W-particles, and the composition and morphology of the DP honeycomb web structure for 95W-NiFe and 95W-NiCu alloys

WHA	W particle size, µm	W-W Contiguity, C_w	Ni/W/(Fe or Cu), Wt.%	DP area fraction, %	thicknes s, t, µm	t/d, (µm/µm)
NiFe	27 ± 11	23.3	49/32/19	12.3	5.2	0.14
NiCu	38 ± 16	32.7	51/39/10	8.9	4.1	0.09

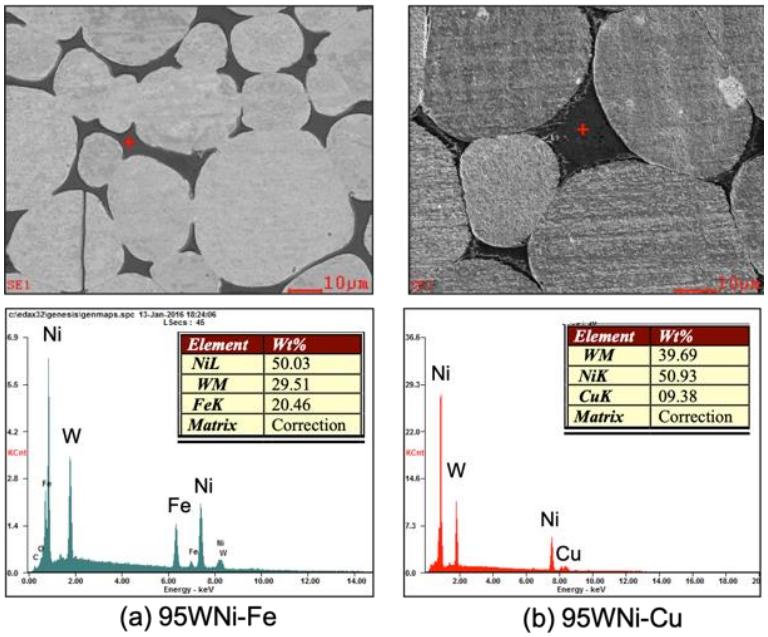

Figure 3.3.8 EDS point scans showing Ni-rich: (a) ~50Ni-30W-20Fe; and, (b) ~ 50Ni-40W-10Cu ductile phase (DP) for NiFe and NiCu 95W WHA, respectively.

3.3.4.2 Microhardness

Room temperature Vicker's microhardness (H_v) test on both the NiFe and NiCu WHA plates show that there is no to little variation of hardness between them (349 ± 7 kg_f/mm^2 for Fe vs 352 ± 10 kg_f/mm^2 for Cu), even though the particle size is different. Lower area fraction of softer DP phase for NiCu WHA might help to retain hardness level same as NiFe WHA (see Tables 3.3.4 and 3.3.5).

3.3.4.3 Room Temperature Tensile Tests

Room temperature engineering tensile stress-strain (s-e) curves are shown in Fig. 3.3.9a-b for 95W-NiFe and 95W-NiCu WHA, respectively, and the results are summarized in Table 3.3.5. While the 0.2% yield strength (s_y) is relatively similar; however, the ultimate tensile strength (s_u); uniform (e_u); and total elongation (e_t) are much inferior for NiCu 95W than the NiFe 95 WHA (Table 3.3.5). Fracture, in all cases, takes place almost immediately after reaching ultimate tensile stress, at low e_u and e_t with virtually no necking.

Table 3.3.5 Room temperature mechanical properties of 95W-NiFe and 95W-NiCu WHA

Alloy	Microhardness, H_v, (kg_f/mm^2)	s_y (MPa)	s_u, (MPa)	e_u (%)	e_t (%)	K_{Jm} (MPa√m)
95W-NiFe	352 ± 10	600 ± 15	818 ± 10	7.3 ± 1	8 ± 1	89 ± 19
95W-NiCu	349 ± 7	620 ± 14	642 ± 25	1.0 ± 0.5	1.2 ± 0.5	47 ± 4

The SEM fractographs of room temperature tensile test on 95W-NiFe and 95W-NiCu WHA alloys are shown in Fig. 3.3.9c-f. Side-surface observation for NiFe WHA shows micro-cleavage on W particles, infer transfer of load to the neighboring particles via well-bonded W-DP interface (see Fig. 3.3.9c), whereas almost clean side surface for NiCu WHA indicates poor interfacial bonding

between W-particles and NiWCu DP phase (see Fig. 3.3.9d). These observations are further confirmed by the SEM images taken from the fractured face (Fig. 3.3.9e-f). SEM fractograph, shown in Fig. 3.3.9e for 95W-NiFe WHA, reveals continuous DP network with strong W/DP interface with virtually no pores. The WC, WW and WD, all the dominating local fracture modes are found for NiFe WHA, with fewer DR [5-6]. However, NiCu WHA tensile fractograph reveals discontinuous DP network with poor interfacial bonding between W and DP, leaving many pore-like empty spaces between W particles (see Fig. 3.3.9f).

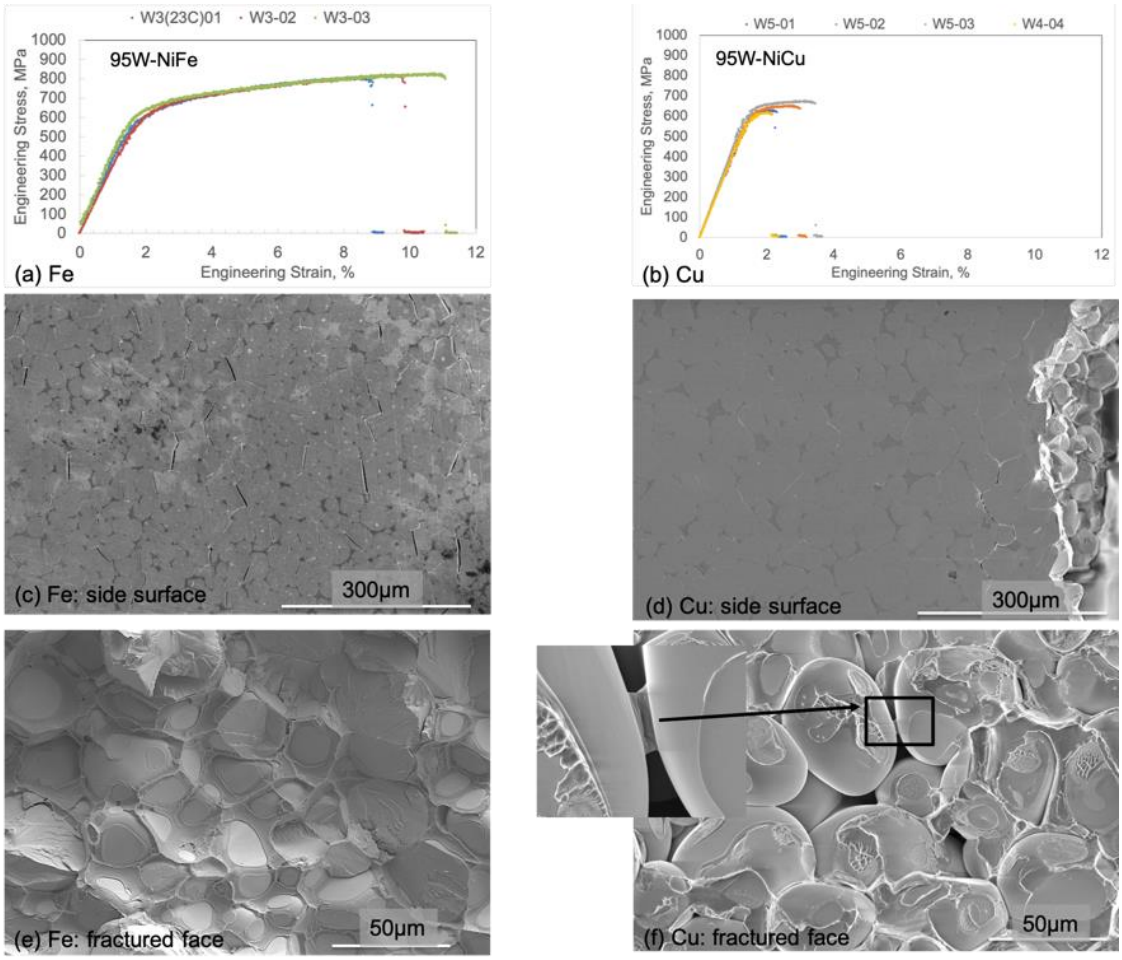

Figure 3.3.9 a) and b) Room temperature tensile s-e for 95W-NiFe (left) and 95W-NiCu (right) WHA, respectively; and, tensile loaded side (c, d) and fractured (e,f) are shown for NiFe (left); and NiCu (right) WHA's, respectively.

Local fracture modes are mostly dominated by WW, which is the weakest of all, with much lower WD, and others modes, responsible for lower ductility. These tensile results and fracture surface observations are quite consistent with the many other research groups results on NiCu WHA's [9-12]. However, our results additionally suggest following for reasons for the lower ductility NiCu WHA's: (i) larger W-particle size with lower DP area fraction; (ii) heterogeneous distribution of W-particles in the DP, forms more W-W particle clusters (higher C_w) and DP pools; (iii) poor interfacial bonding between W and NiWCu DP, confirmed by higher magnification (x50,000) SEM scan, not shown here; and, (iv) lower wettability of NiWCu DP, again confirmed by SEM scan (see insert of Fig. 3.3.9f) that shows a small amount of DP present in-between two closely-spaced W-particles.

3.3.4.4 Room Temperature Fracture Toughness

Room temperature fracture toughness tests on the medium and large NiCu 95W specimens have been conducted and their P-d curves are compared with NiFe 95W specimens, shown in Fig. 3.3.10a. Again, all are fatigue precracked and the shown P-d curves are normalized for a/W= 0.5 (Fig. 13.3.10a). It can be seen from Fig. 3.3.10a that, for both medium and large specimens, NiCu WHAs experience much lower load before yielding, and post-yield load drop is much sharper than for the NiFe WHA. However, all of them show some stable crack growth. The average RT K_{Jm} for size-specific (Table 3.1), and size-independent (Table 3.3.5) 95W-NiFe and 95W-NiCu specimens are also included. Table 3.3.5 shows that the K_{Jm} for NiCu WHA is ~ half to that of NiFe WHA. Fig. 3.3.10b shows the RT fracture toughness versus the tensile $\sqrt{e_t s_u}$ (scaling the energy needed to fracture tensile specimen) for the 95W-NiFe and NiCu WHA's follow a similar trend line.

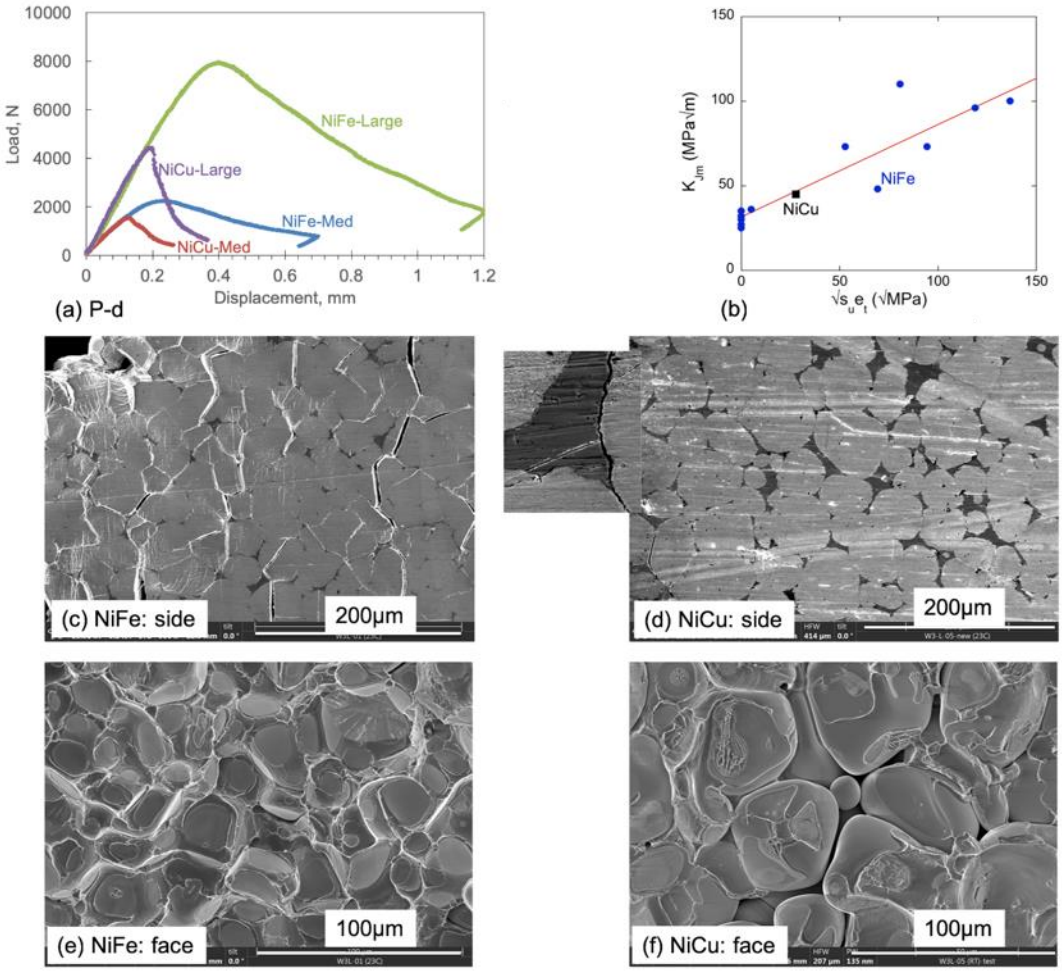

Figure 3.3.10 (a) Room temperature P-d curves for the NiFe and NiCu medium and large WHA specimens; (b) fracture toughness vs. $\sqrt{s_u e_u}$; (c) fractured side surface for 95W-NiFe large specimen showing micro-cleavage W particles along with slip lines for deformed W-particles; (d) loaded side surface for the 95W-NiCu large specimens with minimal micro-cleavage and predominant crack propagation through WW and W-DP interface (see insert); (e) presence of all four local fracture modes for NiFe WHA; and, (f) the absence of DP between many of the W-particles for a NiCu WHA, respectively.

The side (Fig. 3.3.10c,d) and face surface (Fig. 3.3.10e,f) SEM images for the RT toughness tested NiFe- (left column) and NiCu (right column) 95W WHAs are shown in Fig. 3.3.10c-f. Like RT tensile loaded fracture observation, fracture toughness specimens also reveal almost identical

features (see Figs. 3.3.9 and 3.3.10). Similar toughening mechanisms, as observed for the small and medium-size specimens, have also been observed for larger NiFe 95W specimens (i.e. micro-cleavage W particles that are arrested and blunted by DP; slip-lines on W-particles parallel to the crack propagation directions, helps to dissipate strain energy etc.), see details in Figs. 3.3.5b-c and 3.3.10c and Ref [6]. In contrast, irrespective of specimen size, NiCu WHA fails to show such strong dilatation toughening mechanism, and shows mostly WW particle separation with very few but sharp micro-cleaved W-particles (see Fig. 3.3.10d). Like tensile fracture surface, toughness fracture surface for NiCu 95W also shows poor interfacial strength (insert of Fig. 3.3.10d), pore-like features, lack of wettability/absence of DP between W-particles, discontinuous DP phase etc. (Fig. 3.3.10f), responsible for lower yield point, sharp load drops after yielding, and thus lower toughness. Nevertheless, they show somewhat stable crack propagation, even for the larger specimen, further convinced that the presence of ferrous-oxide impurity at the crack tip is only to blame for the unstable crack propagation observed for two of the large NiFe 95W specimens, and not to this 95W alloy composition or it's specimen size.

3.4 CONCLUSIONS AND FUTURE WORK

The room temperature toughness test on different size and geometry of the WHA specimens have been conducted. The summary of these findings are follows:

- The RT toughness test on 3-8x larger than the base-line (thickness, B=1.65mm; width, W= 2B), inelastically fractured specimens show similar toughening mechanisms like small specimens with slightly decreasing K_{Jm} with W loading up to 95W (92 ± 6 MPa√m for 90W and 79 ± 7 MPa√m for 95W). However, 3x larger 97W (K_{Ic} ≈ 38 ± 4 MPa√m) or two 6-8x larger 95W (K_{Ic} ≈ 60 ± 1 MPa√m) specimens fractured elastically, still 5 to 8 times higher than the monolithic W toughness.

- Even at 97W, the WHA is fully ductilized at RT for tensile and small fracture specimens. However, while K_{Ic} remains high in this case, the ductile tearing in small specimens gives way to elastic fracture in specimens 3x larger.
- Ductile tearing persists in WHA with up to 95W in specimens up to 8 times larger than the small bend bars.
- Size effects may emerge in even larger specimens, especially those linked to statistical weakest link effects.
- An exception is two 95W WHA that contained huge brittle oxide inclusions at the precrack, along with lower DP% and weakly bonded W-DP interface, that fractured elastically, but at a high K_{Ic}.
- 95W-NiCu alloy shows almost half the toughness of the 95W-NiFe alloys (47 ± 6 vs 89 ± 19 MPa$\sqrt{m}$). Lower solubility of Cu, bigger W particle size, and weak interfacial bonding between W and NiCu DP affects the lower toughness for NiCu-WHA.

- These WNiFe alloys will almost certainly be part of hybrid materials components, perhaps serving an intermediate crack arrest function like in a monolithic W:W-NiFe:ODS steel:Cu multilayer. Therefore, in future, these alloys will be joined with pure W using spark-plasma sintering (SPS) to synthesis hybrid composite and toughness test will be conducted.

REFERENCES

[1] M. Rieth, S. L. Dudarev et al., Recent progress in research on tungsten materials for nuclear fusion applications in Europe, J. Nucl. Mater. 432 (2013) 482-500.

[2] P. Norajitra, R. Giniyatulin, W. Krauss, V. Kuznetsov, I. Mazul, I. Ovchinnikov, J. Reiser, M. Rieth, V. Widak, Current status of He-cooled divertor development for DEMO, Fusion Eng. Des. 84 (2009) 1429–1433.

[3] V. Philipps, Tungsten as material for plasma-facing components in fusion devices, J. Nucl. Mater. 415 (2011) S2–S9.

[4] J. Davis, V. Barabash, A. Makhankov, L. Plöchl, K. Slattery, Assessment of tungsten for use in the ITER plasma facing components, J. Nucl. Mater. 258–263 (1998) 308–312.

[5] M.E. Alam, S. Pal, K. Fields, G.R. Odette, Mechanical properties characterization of 90-97wt% WNiFe heavy alloys, DOE Fusion Reactor Materials Program Semiannual Progress Report, DOE/ER-0313/61 (2016) 73-82.

[6] M.E. Alam, G. R. Odette, "On new and remarkably powerful toughening mechanisms in W-NiFe heavy alloys", DOE Fusion Reactor Materials Program Semiannual Progress Report, DOE/ER-0313/64 (2018) 69-80.

[7] ASTM E1921-13a, Standard Test Method for Determination of Reference Temperature, T_o, for Ferritic Steels in the Transition Range, ASTM International, West Conshohocken, PA, 2013.

[8] ASTM, Standard Test Method for Measurement of Fracture Toughness, ASTM Standard E1820-13, ASTM B. Stand. (2013) 1–54.

[9] D. V. Edmonds, P.N. Jones, Interfacial embrittlement in liquid-phase sintered tungsten heavy alloys, Metall. Trans. A. 10 (1979) 289–295.

[10] X. Gong, J. Fan, F. Ding, Tensile mechanical properties and fracture behavior of tungsten heavy alloys at 25-1100 °C, Mater. Sci. Eng. A. 646 (2015) 315–321.

[11] K. Hu, X. Li, X. Ai, S. Qu, Y. Li, Fabrication, characterization, and mechanical properties of 93W-4.9Ni-2.1Fe/95W-2.8Ni-1.2Fe/95W-2.8Ni-1.2Fe-1Al_2O_3 heavy alloy composites, Mater. Sci. Eng. A. 636 (2015) 452–458.

[12] J. Das, G. A. Rao, S.K. Pabi, Microstructure and mechanical properties of tungsten heavy alloys, Mater. Sci. Eng. A. 527 (2010) 7841-7847.

CHAPTER 4

ON THE FRACTURE BEHAVIOR OF WNiFe HEAVY METAL ALLOY HYBRIDS

ABSTRACT

The strength and fracture toughness properties of four ductile phase toughened (DPT) commercially available tungsten (W)-based heavy metal alloy composites (WNiFe), reinforced with 3 to 10 (wt.%) of a NiFe phase, were previously thoroughly characterized from room to liquid nitrogen (LN_2) temperatures. All the alloys manifested a sub-zero brittle-to-ductile transition temperature (BDTT) ranging from -50ºC to -150ºC, depending on the amount of the ductile NiFe phase. Specimen size, geometry and DP constituent effects on toughness were also characterized. In this study, pure W was coated on the WNiFe alloys by spark plasma sintering (SPS) at 1350ºC under a 50 MPa pressure load. Three-point bend (3PB) bars were fabricated and room temperature toughness tests were conducted to understand the crack formation and propagation mechanisms from the pure W coating up, to or into, the WNiFe alloy through or near the W:WNiFe interface. The results show that the pure W coating on the 90 and 92.5WNiFe alloy hybrid exhibits mode-I fracture and ductile phase toughening, while the 95 and 97WNiFe alloy hybrid exhibit a mode-II toughening mechanism, with deflected cracks at the W:WNiFe interface, possibly due to higher W-coating porosities in these cases.

4.1 INTRODUCTION

Due to high melting temperature, good conductivity, low sputtering rates and high-temperature strength, tungsten (W), and its alloys, are currently considered the most promising candidates for plasma facing component for future fusion reactor divertor applications [1-5]. This

application requires that structural W-based alloys and structures have sufficient fracture toughness to withstand the severe thermal-mechanical environment of a divertor. It is likely that monolithic W is intrinsically too brittle for this task. Previously a series of WNiFe (90, 92.5, 95 and 97 wt.% W with 7:3 = Ni:Fe) heavy metal alloys were shown to have much higher room temperature toughness (> 10x) and much lower BDTT temperatures (-150 to -50 ºC) than monolithic W (several hundred °C), depending on their ductile phase NiFe content [6-10]. In the work reported here, the fracture behavior of pure W:WNiFe alloy hybrid coupons, fabricated by SPS, were explored. Room temperature toughness tests were performed on the W:WNiFe hybrid coupons to: a) observe crack propagation paths after they initiate in the pure W coating; and, b) estimate the effective W:WNiFe hybrid coupon toughness.

4.2 EXPERIMENTAL PROCEDURES

Pure W powder (size: 4-6 µm, purity: 99.95%, Stanford Materials) was used to coat four commercially available (Mi-Tech Metals, Indianapolis, In, USA) liquid-phase sintered WNiFe heavy metal alloy composites containing 90, 92.5, 95 and 97 wt.% W and a 7:3 Ni:Fe ductile phase. The coating was fabricated by spark plasma sintering (SPS). First, 20mm diameter-2mm thick discs were cut from WNiFe alloys by electrical discharge machining (EDM). The discs were ground with 80µm to 1µm SiC paper to remove residual stresses and oxide layers formed during EDMing, and cleaned ultrasonically for 15 minutes in alcohol. Twenty mm diameter graphite and Nb foils were used to lubricate the SPS loading stack-up and to reduce tungsten carbide formation, respectively. The graphite shaft/ram and foils, Nb foils, W powder and the WNiFe alloy disc were stacked inside a 20.7mm inner diameter graphite die, as shown in Figure 4.2.1a. The stack-up consisted of elemental W powder, which was weighed inside an argon-filled glove box (containing less than 10 ppm oxygen) and poured on top of WNiFe disc, followed by the Nb and graphite foils and the graphite shaft. The W:WNiFe hybrid coupons were consolidated and bonded

in vacuum under a 50MPa compressive pressure at a sintering temperature of 1350ºC, with 10 min dwell time. The sintering temperature was restricted due to the lower melting temperatures of Ni (~1450ºC) and Fe (~1540ºC). Both the heating and cooling stages were performed at 50ºC/min. The amount of W powder was selected to produce a 2 mm thick coating after consolidation, resulting in ~20mm diameter-4mm thick W:WNiFe hybrid coupons (Fig. 4.2.1b).

EDM was then used to fabricate single-edged notch three-point bend (3PB) specimens with nominal dimensions of 16 mm length, 3.3 mm width and 1.67 mm thickness (Fig. 4.2.1c). Pre-cracking was not performed, and the notch depth of a/W ≈ 0.4 was selected to place the initial neutral axis in the WNiFe disc, in order to provide a driving force for the W-initiated crack to penetrate into the WNiFe alloy. In addition, a shallower a/W ≈ 0.15 notch, with the neutral axis in W side of the hybrid coupon, was used in some tests on the W:90WNiFe hybrid. A 810 MTS servo-hydraulic universal testing machine was used to load hybrid bend bars, and a Questar long-distance (telescopic) optical microscope with 3-axis positioning system was used to observe *in-situ* crack initiation and propagation at a frame rate of 6/min. The sides of the 3PB bars were sanded with a sequence of 2000 grit, 9µ, 3µ and 1µ paper to provide a better surface finish for crack imaging. The toughness tests were carried out at a crosshead speed of 0.04mm/min. While not fully applicable, ASTM E1921 type procedures were generally used to evaluate both the elastic and plastic components of fracture toughness of hybrid bend bars [11]. The plastic K_{Jc} were calculated at the maximum load (P_m) in the load-displacement (P-d) curve. Three to four specimens were tested for each WNiFe alloy ductile phase NiFe content.

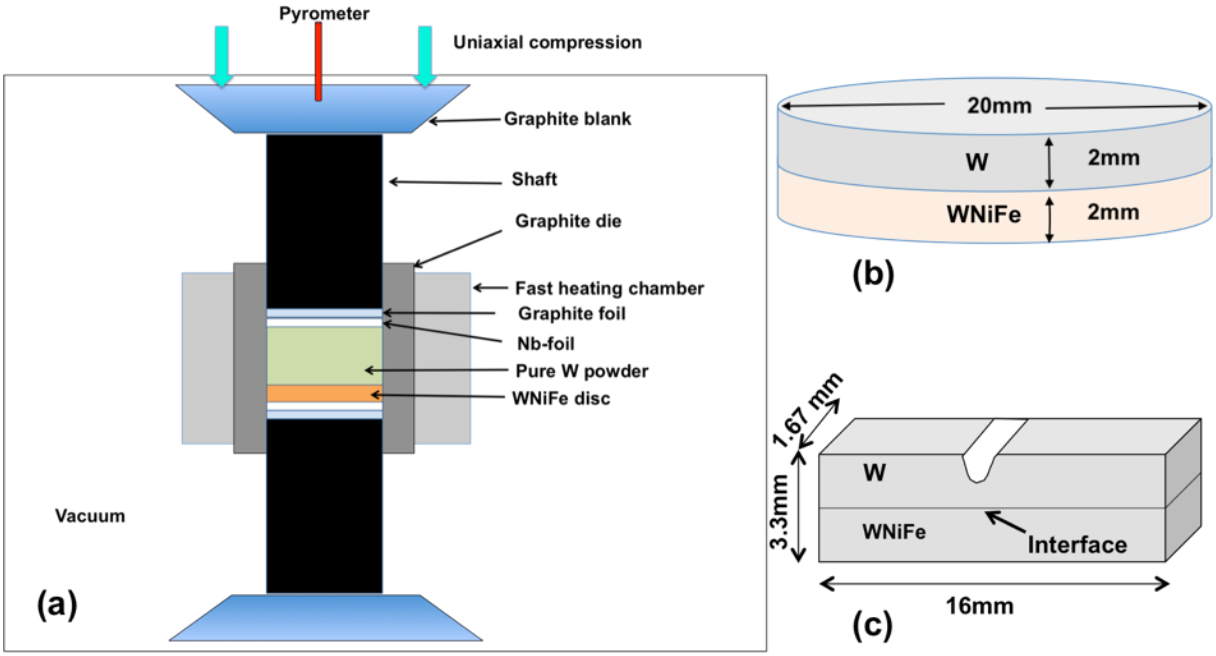

Figure 4.2.1 Schematic diagrams of: (a) SPS process set up; (b) a W-coated WNiFe hybrid disc; and, (c) the 3PB bar used for fracture testing.

4.3 RESULTS AND DISCUSSION

4.3.1 Microstructure

SEM micrographs of the polished W-coated-WNiFe alloy hybrids reveal roughly spheroidal W particles surrounded in the interconnected skeleton of a ductile NiFe phase in WNiFe alloy side (top part of Fig. 4.3.1a). Note the NiFe phase also contains about 30% W after liquid metal sintering. Note, there is a clean, and apparently well-bonded interface. A low volume fraction of pores in the W coating is also observed, especially in the 95 and 97WNiFe hybrids.

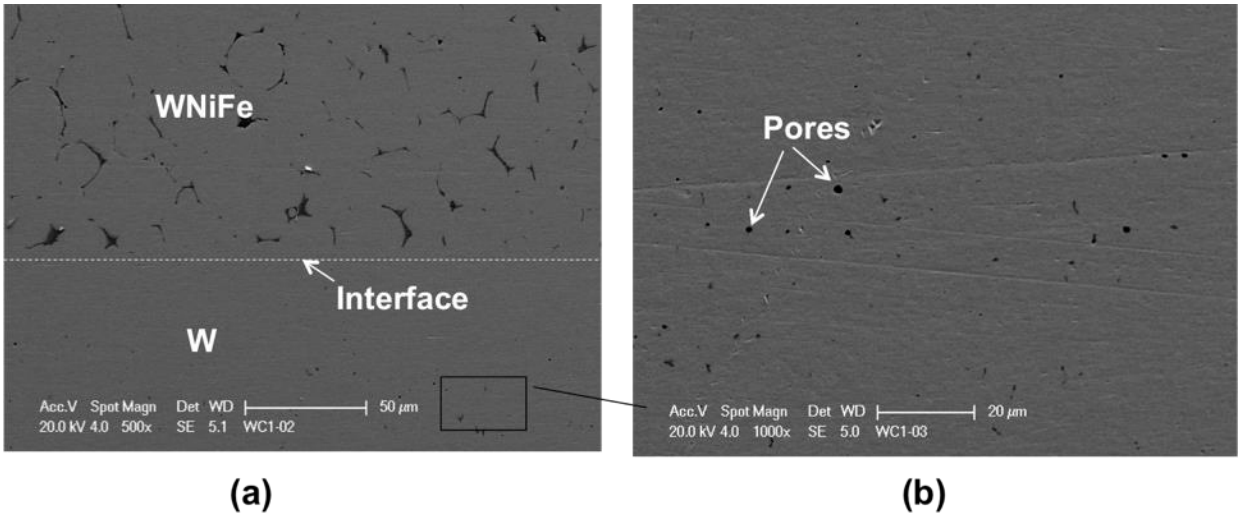

Figure 4.3.1 (a) The clean and well-bonded interface between W and WNiFe; and, (b) pores in the pure W coating.

4.3.2 Fracture Toughness

As reported previously, fracture toughness tests on 90-97WNiFe alloys were conducted from room temperature (RT) down to liquid nitrogen (LN_2) temperatures [6-10]. In summary, all alloys tested at RT show continuous load drop after the maximum load (P_m) with increasing displacement (d), indicating stable crack growth. The average maximum load K_{Jc} was ≈ 96 ± 20 MPa√m. The toughness generally decreases with deceases in the NiFe(W) ductile phase content, and is minimum at 97W. Stable ductile tearing is still observed in the 90WNiFe alloy at -100ºC, while somewhat mixed (stable + unstable) crack growth occurs at -150ºC [7,8]. Brittle fracture is observed at the LN_2 temperature in all cases. The corresponding transition temperatures for the other alloys were ≈ -100 ºC, -75 ºC, and -50 ºC for the 92.5, 95 and 97.5W alloys, respectively.

New RT fracture toughness tests were carried out on the hybrid 3PB bars. Figure 4.3.2 shows the result for a deeply notched (a/W ≈ 0.4) 3PB bar of the W:90WNiFe hybrid coupon, including the P-d curve (Fig. 4.3.2a) along with a profile view of the propagated crack (Fig. 4.3.2b), and a profile view showing the sequence of crack propagation (Fig. 4.3.2c). The load increases to Point-

1, associated with the brittle elastic fracture toughness of pure W, then suddenly drops, as crack growth initiates from W-notch, and propagates through W matrix to the W:90WNiFe interface, as a large pop-in event. The load then increases again until the arrested blunting crack penetrates into the 90WNiFe alloy. The load decreases thereafter under stable growth in the WNiFe alloy. The second a/W = 0.4 test behaved in a similar fashion.

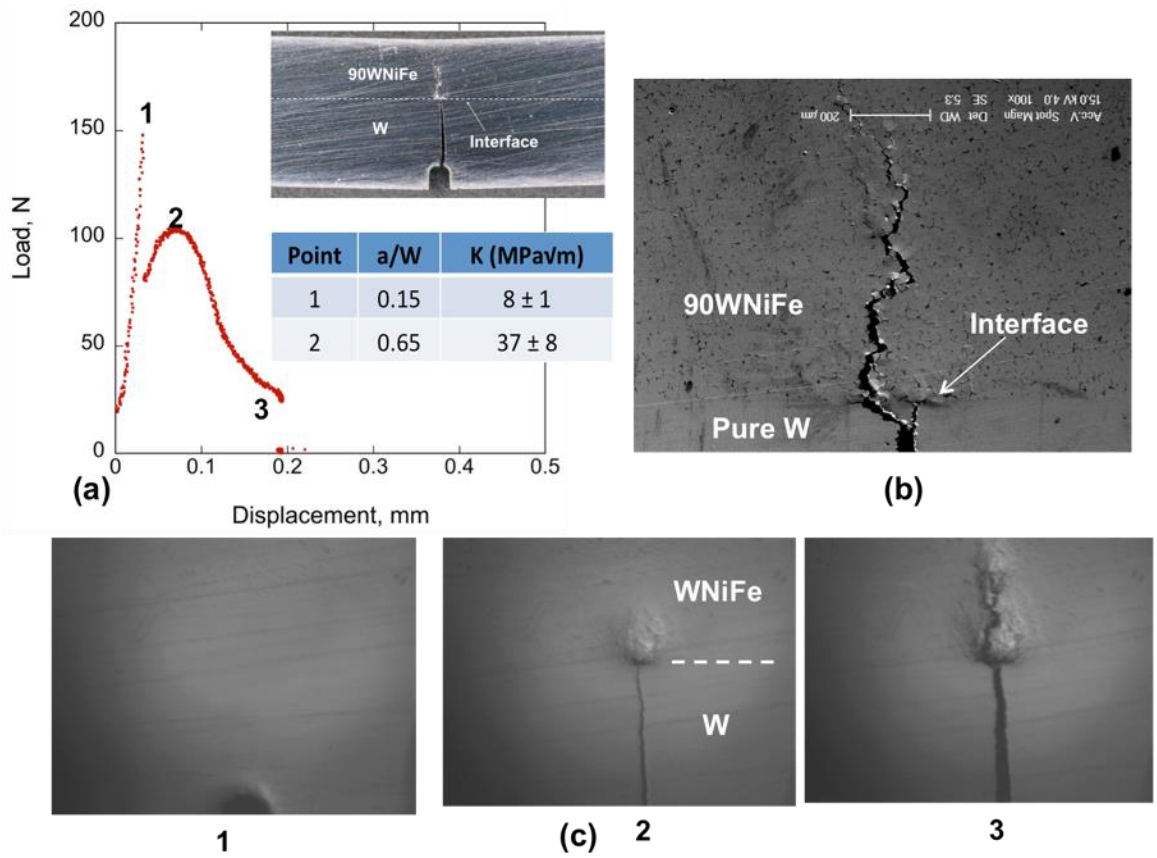

Figure 4.3.2 Characterization of cracking in the W:90WNiFe hybrid: (a) the load-displacement (P-d) curve with the W and peak load 90WNiFe alloy toughness values and a profile view of the tested specimen; (b) a SEM micrographs of propagated crack; and (c) in-situ optical micrographs associated with the numbered loading points.

Two other tests were conducted with smaller initial a/W ≈ 0.15, so that the initial neutral axis lies in W, rather than the 90WNiFe alloy side. The initiation toughness of pure W was same for all

tests that averaged K_{IC} ≈ 8 ± 1 MPa√m (see Table 4.3.1). Crack propagation was also similar to that described above. However, maximum load toughness of 90WNiFe is slightly higher for smaller notch specimens with K_{Jc} values of averaging ≈ 44 ± 4 MPa√m than deeper notched specimens at ≈ 32 ± 2 MPa√m (Table 4.3.1). Note these values are much lower than those for the as-received 90WNiFe alloy (95 ± 20 MPa√m) [8]. The lower maximum load toughness is probably due the effects of the W side of the interface on the crack blunting needed to initiate growth in the 90WNiFe alloy.

Table 4.3.1 Notch depth and toughness values of pure W and WNiFe hybrid composites

Hybrid composites	**Initial a/W, p-1**	**K_{IC}, MPa√m**	**a/W for WNiFe, p-2**	**K_{Jc}, MPa√m**
W/90WNiFe	0.404	8.8	0.651	30.0
	0.402	7.8	0.629	33.2
	0.154	6.7	0.612	47.3
	0.154	7.6	0.682	40.3
	Average	**7.7 ± 0.8**	**Average**	**37.7 ± 7.7**
W/92.5WNiFe	0.349	6.4	0.603	22.5
	0.356	11.4	0.61	22.0
	0.355	9.4	0.59	50.5
	Average	**9.3 ± 2.5**	**Average**	**31.7 ± 16.3**

The tests on the other alloy compositions were all made with 3PB bars with deep notches. Figure 4.3.3 shows a representative P-d curve for W:92.5WNiFe hybrid along with *in-situ* optical

micrographs and a SEM fractograph. Similar to W/90WNiFe hybrid, the W/92.5WNiFe load increased up to Point-1 marking the W toughness, followed by sudden load-drop due to crack propagation to arrest at the interface. The load then increased to Point-2 marking the blunting and re-initiation of stable crack growth in the 92.5WNiFe alloy. The W toughness was ≈ 9 ± 2 MPa√m, while the average 92.5WNiFe alloy toughness was slightly lower (32 ± 16 MPa√m) than that for 90WNiFe hybrid (37 ± 8 MPa√m, see Table 4.3.1). However, one of the W/92.5WNiFe shows higher K_{Jc} toughness as the crack slightly deflected at the interface, but later penetrated into and propagates through the WNiFe alloy.

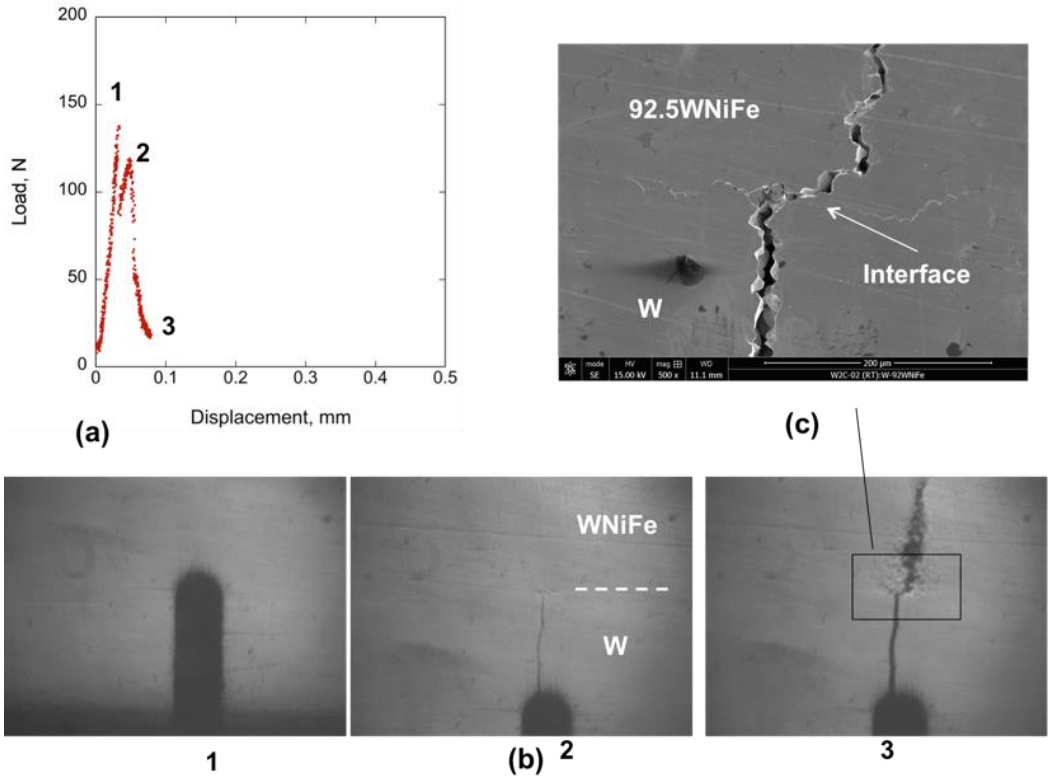

Figure 4.3.3 Characterization of cracking in the W:92.5WNiFe hybrid: (a) the load-displacement (P-d) curve; (b) in-situ optical micrographs associated with the numbered loading points; and, (c) a SEM micrograph of propagated crack.

Figures 4.3.4 and 4.3.5 show load-displacement curves along with micrographs for W-coated 95WNiFe and 97WNiFe hybrids, respectively. Unlike the W:90 and 92.5WNiFe hybrids, the load

continuously increases as cracks arrests and is deflected perpendicular to the loading direction, running along, or near, the interface. One possible reason for selection of the crack deflection path is the higher porosity observed on the W side for the 95 and 97WNiFe hybrids (Figs. 4.3.2c, 4.3.4c,f, and 4.3.5b). The pores may make the interface debonding an easier path for crack to propagate in these cases, rather than penetrating into and propagating through the 95 and 97.5WNiFe alloy. Crack deflection leads to a load displacement curve that continuously increases up to the end of the test. Thus, it is not formally possible to define a maximum-load toughness, but the effective toughness and resistance curve behavior is very high. Note, the W coating cracked internally under preloading condition, again possibly due to the larger amount of porosity in the W. Although the pores may improve the toughness of 95 and 97WNiFe hybrids, it may have detrimental effects on other properties (like strength), or the functionality of W components.

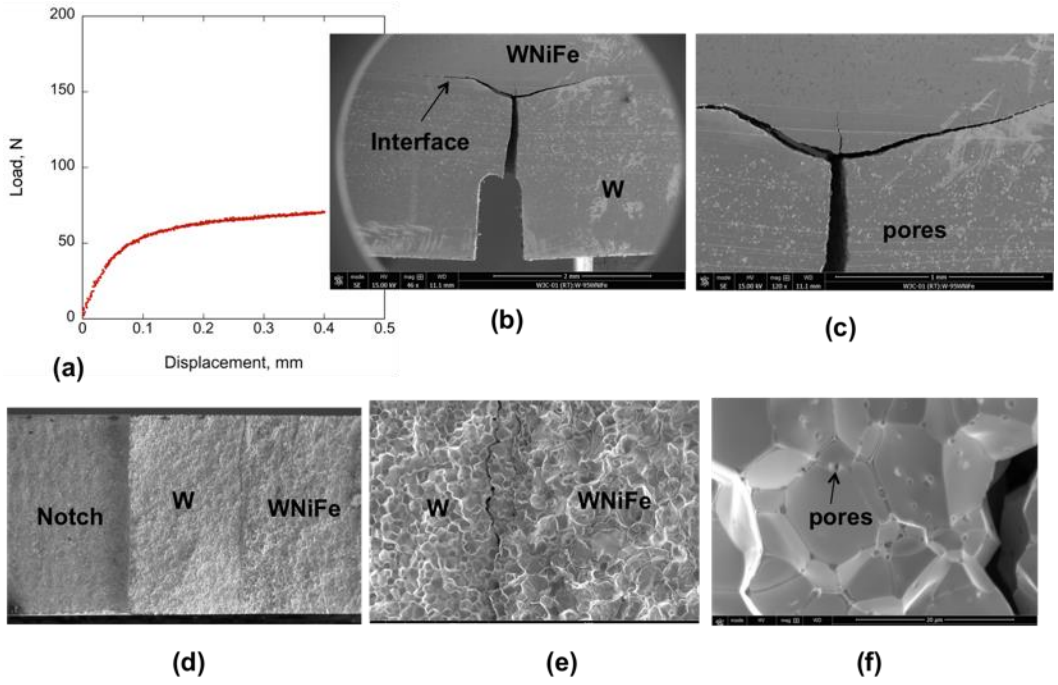

Figure 4.3.4 Characterization of cracking in the W:95WNiFe hybrid: (a) the load-displacement (P-d) curve; (b) and (c) profile images of the crack showing a 90° deflection and propagation along or near the W:95WNiFe hybrid interface; and, (d) to (f) micrographs of the fracture surfaces at increasing magnification.

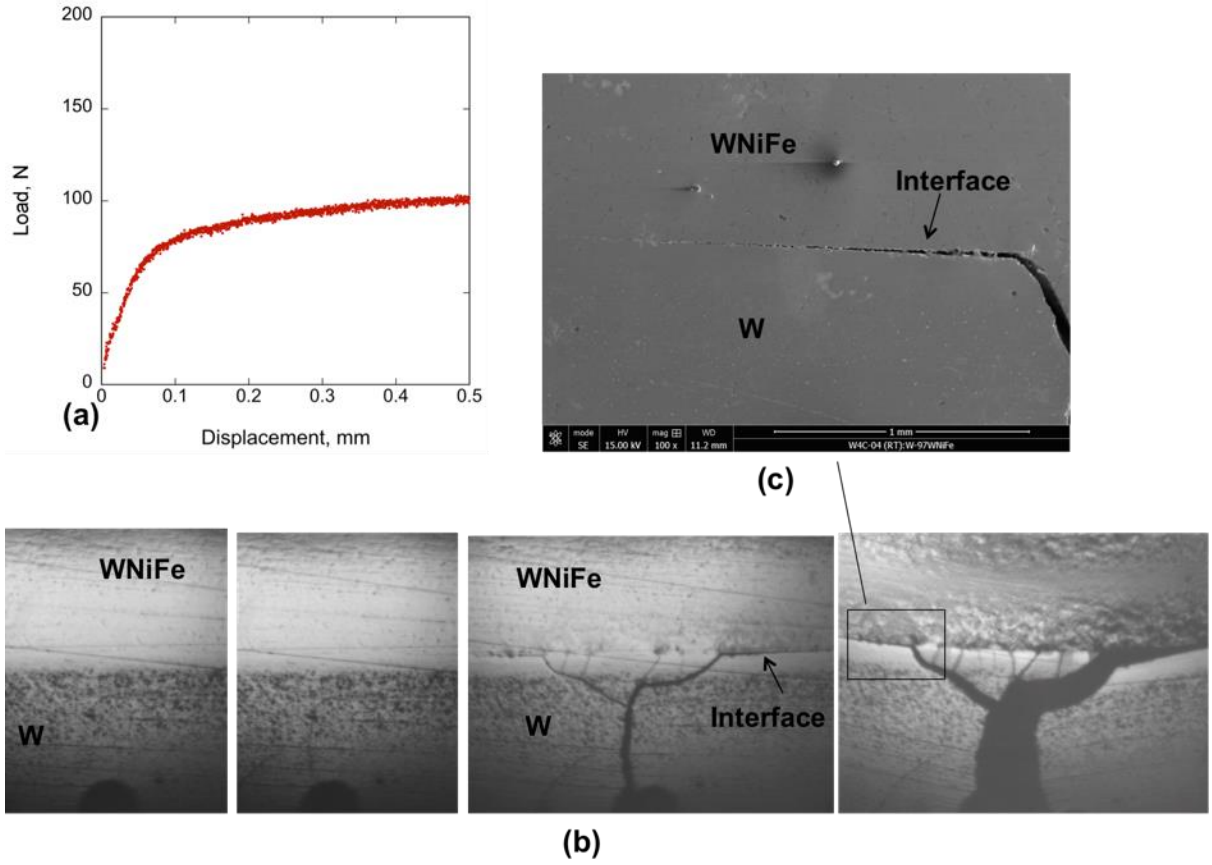

Figure 4.3.5 Characterization of cracking in the W:97WNiFe hybrid: (a) load-displacement (P-d) curve, (b) in-situ optical micrographs with crack propagation along the interface; and, (c) a SEM micrograph of the deflected crack at the interface.

4.4 CONCLUSIONS AND FUTURE WORK

- Tungsten powders were coated on WNiFe alloys to synthesis W-WNiFe alloy hybrid using spark plasma sintering.
- 90 and 92.5W-NiFe shows good and strong interfacial bonding between W and WNiFe interface. Cracks penetrate and propagate from pure W side into the WNiFe alloy side.

- However, 95 and 97W-NiFe alloys coated with pure W shows relatively poor bonding and higher pores in pure W sides. Crack deflects at the interface due to the poor bonding, even though load increases with displacement as the stress-field shifts.

- Much more work is needed to model the micromechanics of fracture in WHA.
- Thermal shock tests will be performed on these WNiFe alloy and hybrids.

- High temperature fracture toughness will be conducted on full-size half width Charpy specimens in controlled environment for all WHAs.

- Additional experimental and modeling research effects of size and geometry on the fracture of WHA is needed.
- There are many outstanding issues regarding the use of W-NiFe WHA in divertor applications. The database and insights developed this report provide the foundation for future progress.

REFERENCES

[1] M. Rieth, S.L. Dudarev, S.M. Gonzalez De Vicente et al, Recent progress in research on tungsten materials for nuclear fusion applications in Europe, J. Nucl. Mater. 432 (2013) 482–500.

[2] P. Norajitra, R. Giniyatulin, W. Krauss, V. Kuznetsov, I. Mazul, I. Ovchinnikov, J. Reiser, M. Rieth, V. Widak, Current status of He-cooled divertor development for DEMO, Fusion Eng. Des. 84 (2009) 1429–1433.

[3] V. Philipps, Tungsten as material for plasma-facing components in fusion devices, J. Nucl. Mater. 415 (2011) S2–S9.

[4] J. Davis, V. Barabash, A. Makhankov, L. Plöchl, K. Slattery, Assessment of tungsten for use in the ITER plasma facing components, J. Nucl. Mater. 258–263 (1998) 308–312.

[5] C. Henager Jr, W. Setyawan, T. Roosendaal, N. Overman, B. Borlaug, E. Stevens, K. Wagner, R. Kurtz, G.R. Odette, B. Nguyen, K. Cunningham, Ductile-phase toughened tungsten for plasma-facing materials in fusion reactors, Int. J. Powder Metall. 53 (2017) 53–69.

[6] M.E. Alam, S. Pal, K. Fields, G.R. Odette, Ductile phase toughening of 90-97wt% W-NiFe heavy metal alloys, DOE Fusion Reactor Materials Program Semiannual Progress Report, DOE/ER-0313/60 (2016) 93-102.

[7] M.E. Alam, S. Pal, K. Fields, G.R. Odette, Mechanical properties characterization of 90-97wt% WNiFe heavy alloys, DOE Fusion Reactor Materials Program Semiannual Progress Report, DOE/ER-0313/61 (2016) 73-82.

[8] M.E. Alam, G. R. Odette, “On new and remarkably powerful toughening mechanisms in W-NiFe heavy alloys”, DOE Fusion Reactor Materials Program Semiannual Progress Report, DOE/ER-0313/64 (2018) 69-80.

[9] M.E. Alam, G. R. Odette, “Influence of specimen size, ductile phase properties and large impurity inclusions on the fracture toughness of tungsten heavy metal alloys: WNiFe and WNiCu”, DOE Fusion Reactor Materials Program Semiannual Progress Report, DOE/ER-0313/65 (2018) 39-51.

[10] M.E. Alam, G. R. Odette, “On the effect of specimen size, geometry and ductile phase content on the fracture toughness of tungsten heavy metal alloys”, DOE Fusion Reactor Materials Program Semiannual Progress Report, DOE/ER-0313/66 (2019).

[11] ASTM E1921-13a, Standard Test Method for Determination of Reference Temperature, T_o, for Ferritic Steels in the Transition Range, ASTM International, West Conshohocken, PA, 2013.

Appendix

Experimental Data

W wire tensile testing: engineering stress vs. normalized displacement

15-μm wire

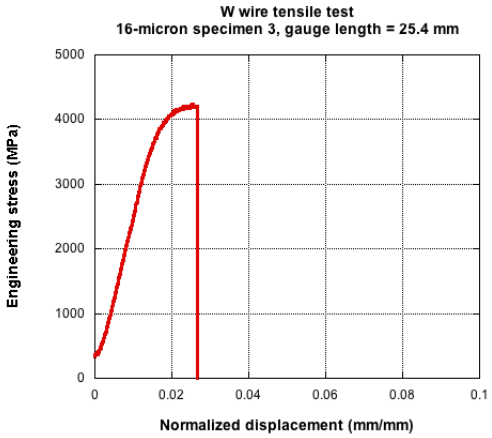

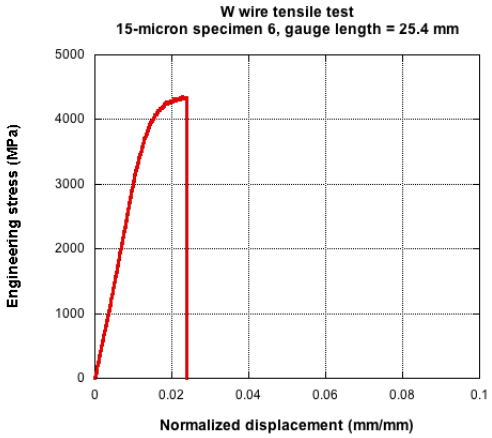

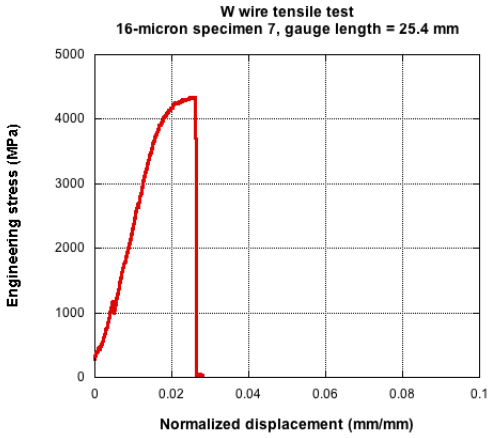

W wire tensile testing: engineering stress vs. normalized displacement

250-μm wire

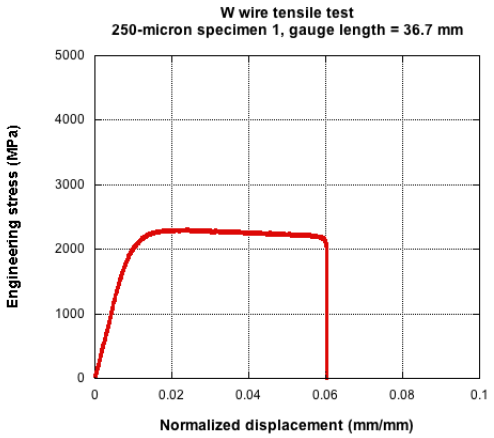

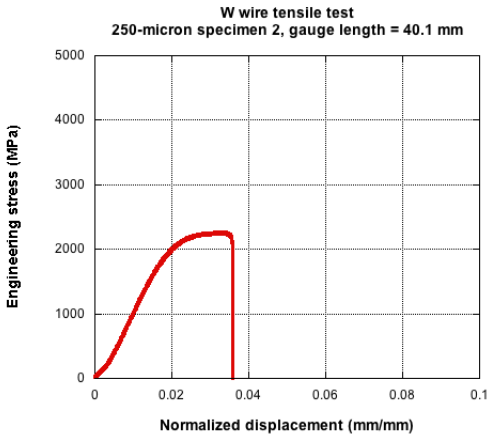

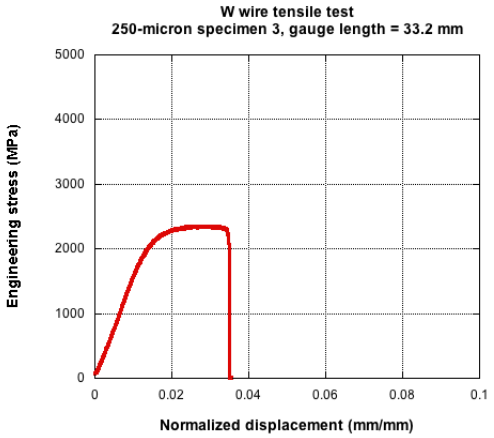

W wire tensile testing: engineering stress vs. normalized displacement

500-μm wire

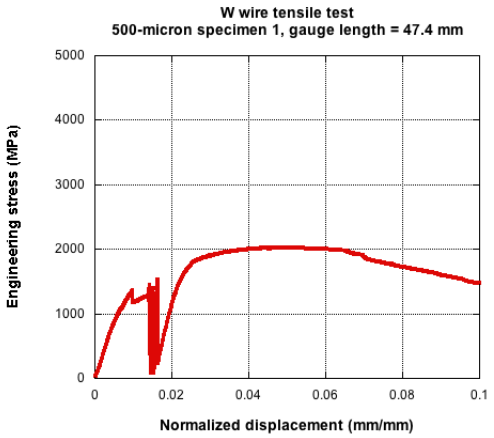

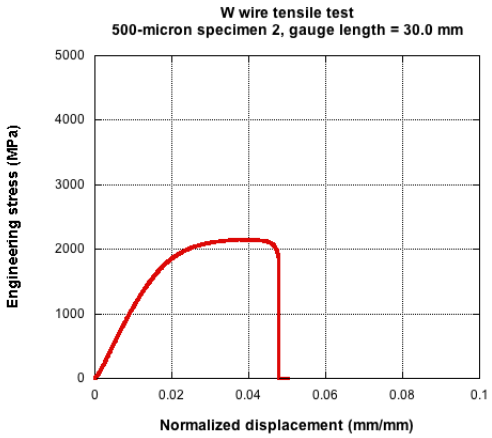

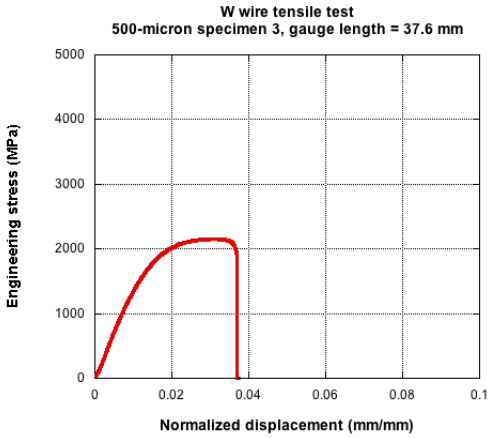

EBSD grain maps and pole figures for W wire

As-received W wire

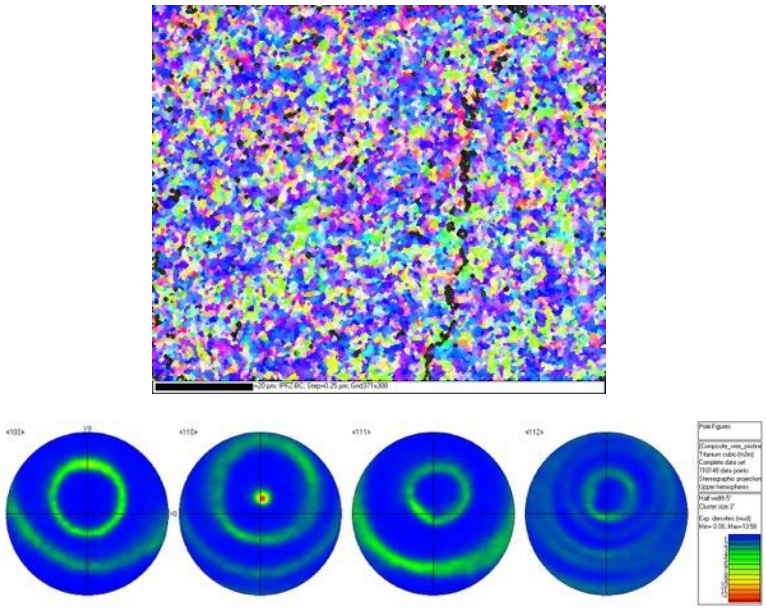

Post-processing W wire (Upper right: sintered W matrix; pole figures from wire area only)

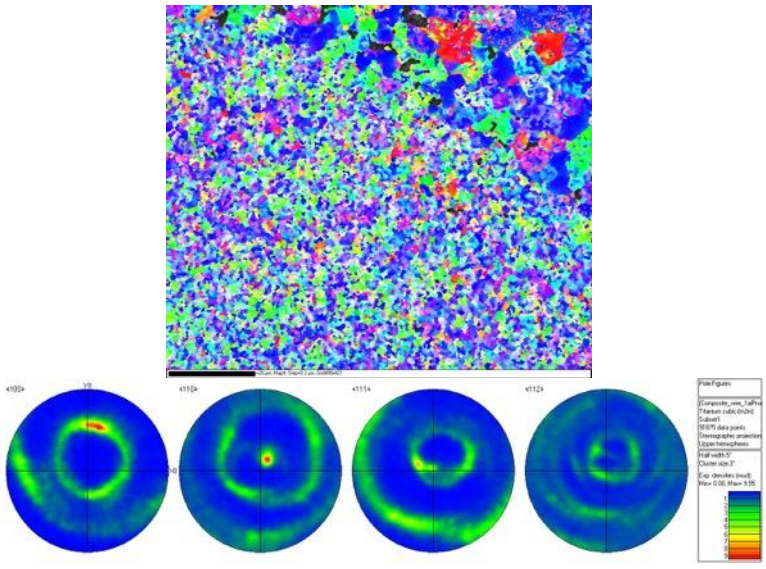

W and Cu foil tensile testing: engineering stress vs. engineering strain

W foil

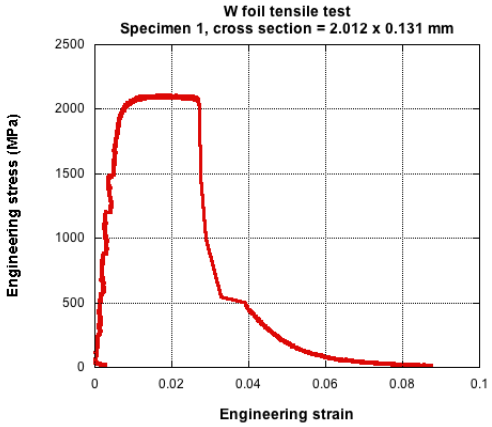

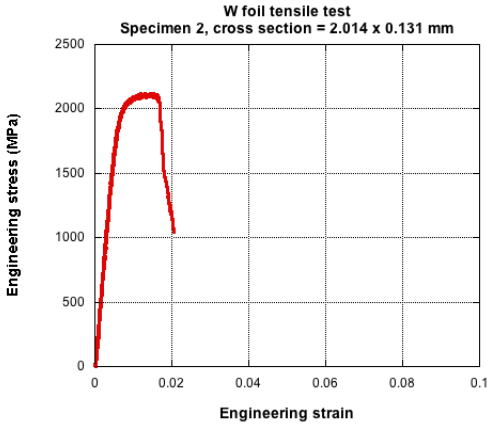

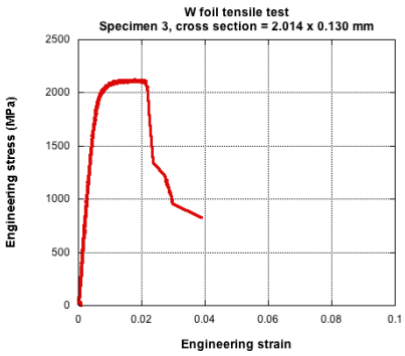

Cu foil

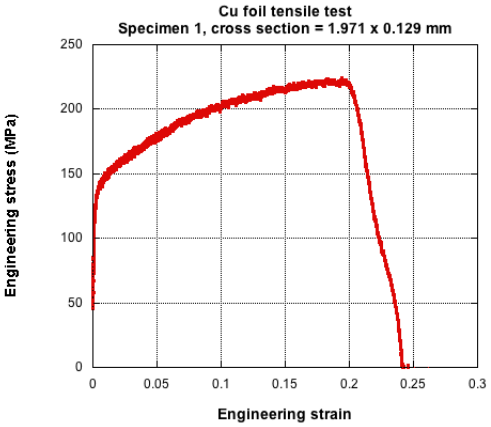

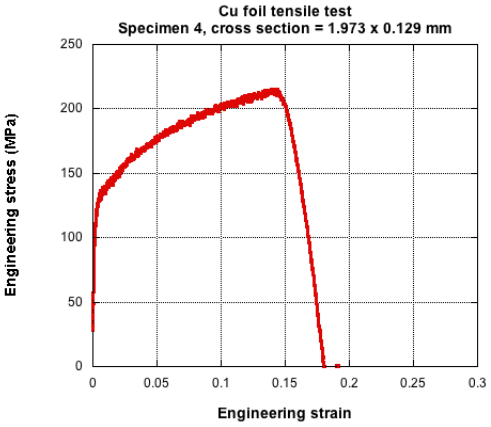

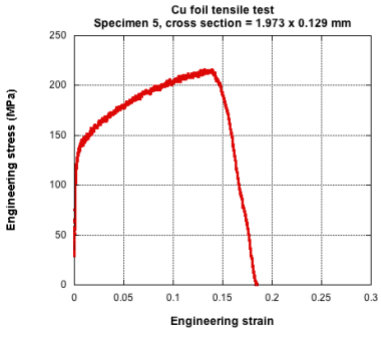

W plate fracture toughness testing: load vs. crosshead displacement

L orientation

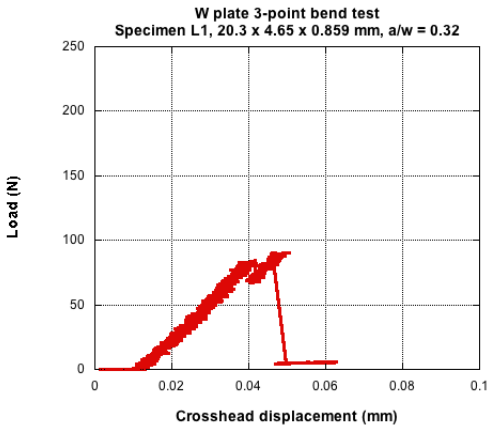

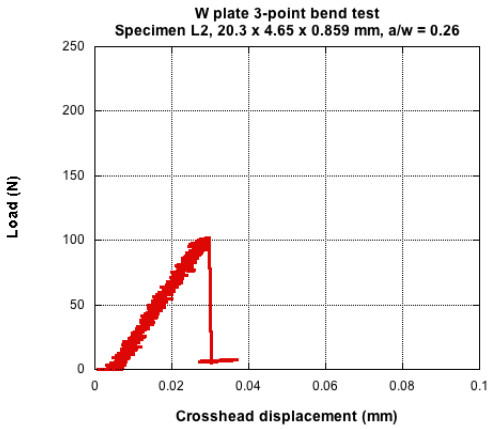

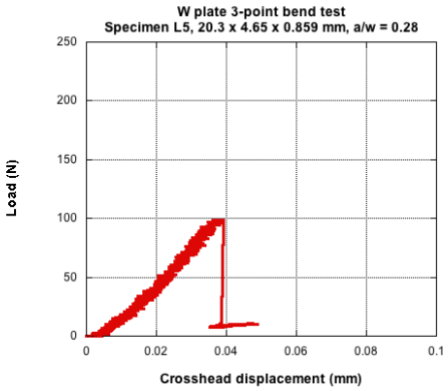

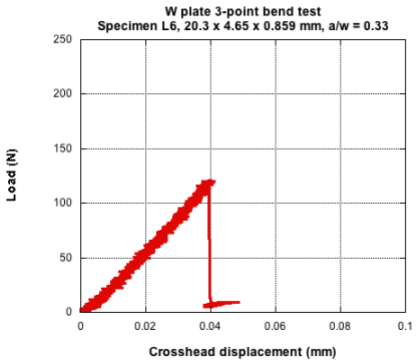

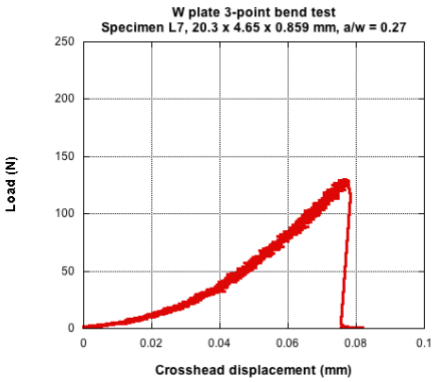

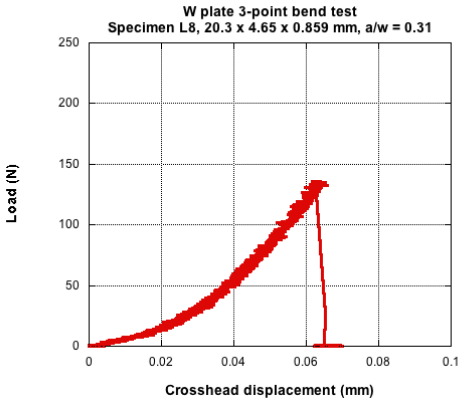

W plate fracture toughness testing: load vs. crosshead displacement

T orientation

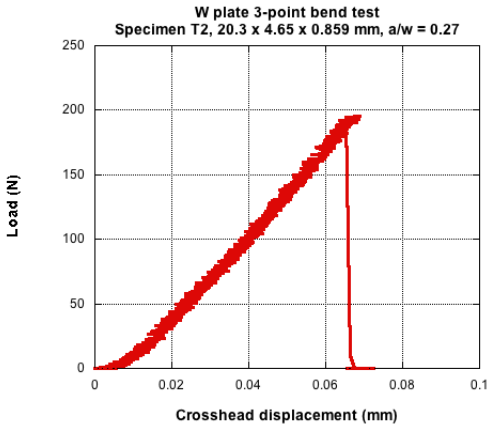

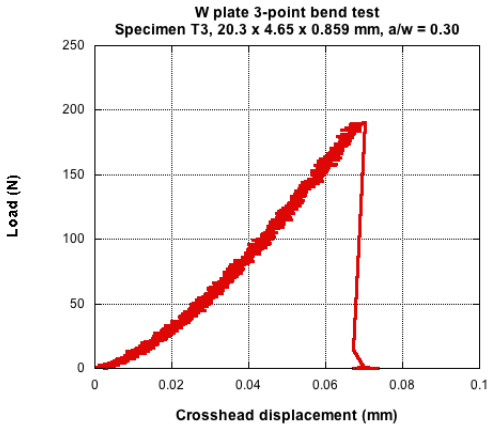

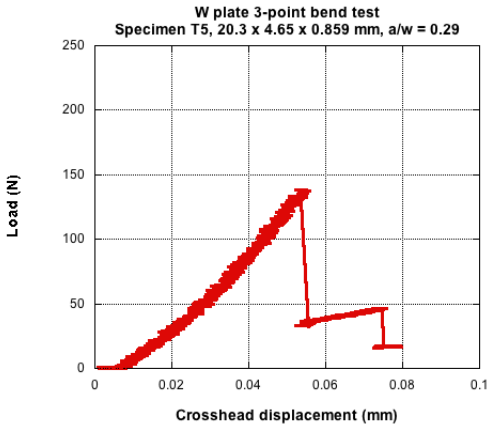

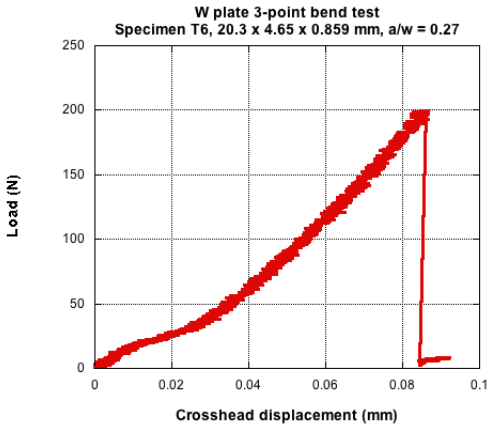

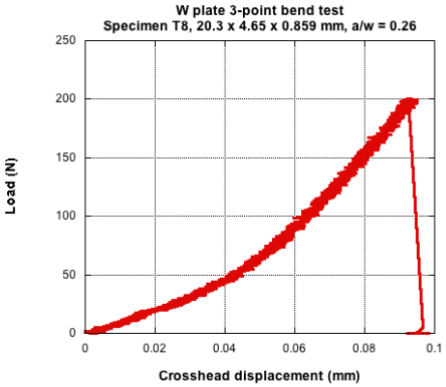

W-WC sintered composite 3-point bend testing: load vs. crosshead displacement

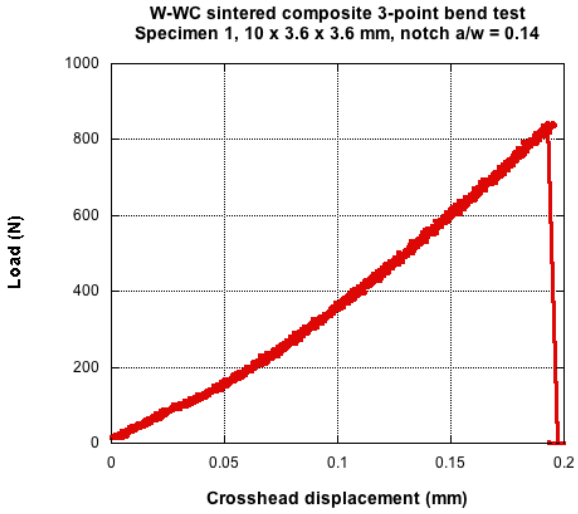

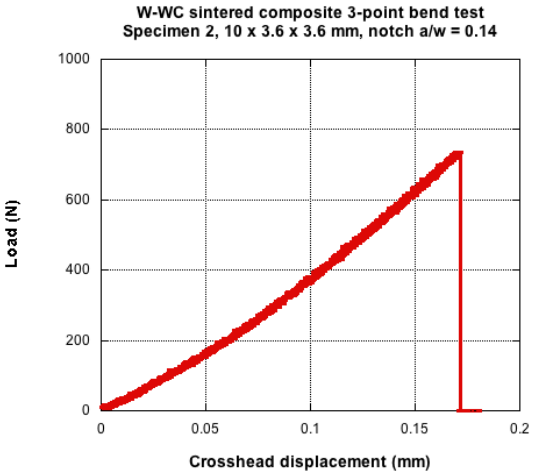

W-Cu hot-pressed laminate testing

Reinforcement tensile testing: engineering stress vs. crosshead displacement

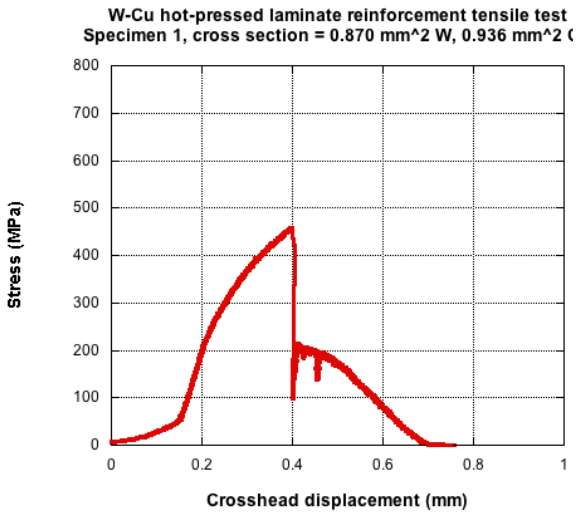

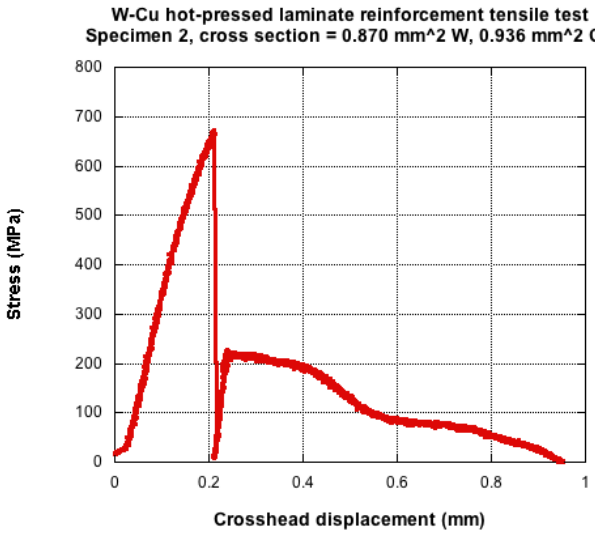

Laminate 3-point bend testing: load vs. crosshead displacement

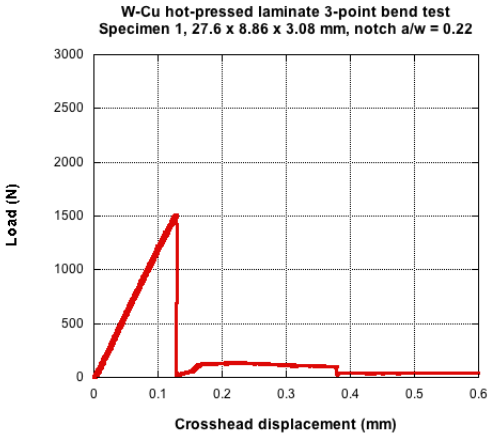

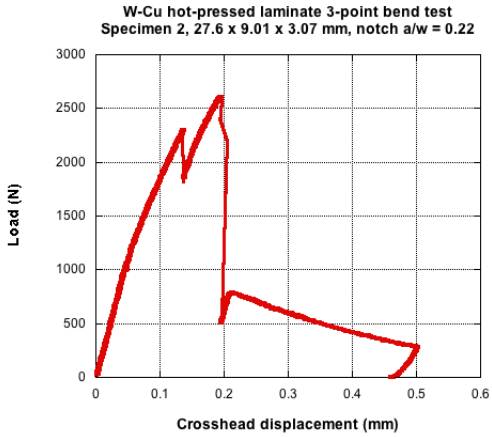

W-Cu brazed laminate: P-D curves and R-curves

L orientation specimens

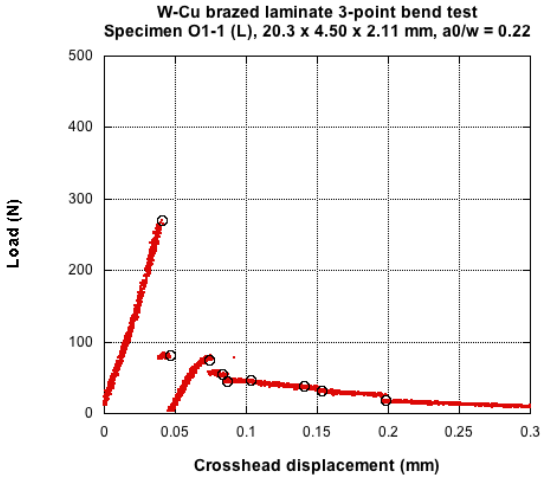

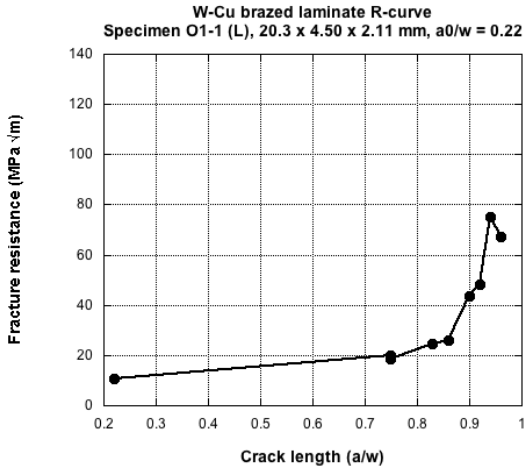

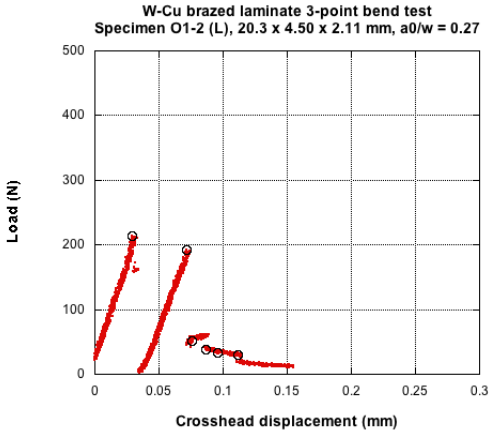
W-Cu brazed laminate 3-point bend test
Specimen O1-2 (L), 20.3 x 4.50 x 2.11 mm, a0/w = 0.27
Load (N)
Crosshead displacement (mm)

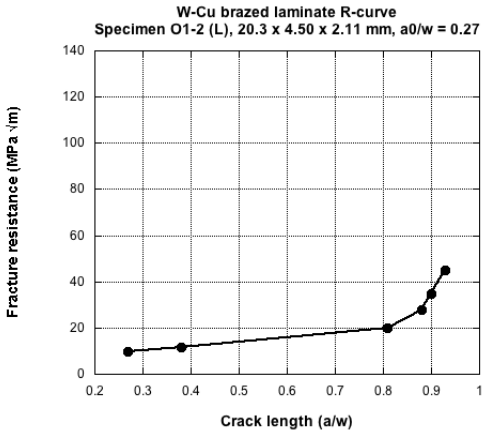
W-Cu brazed laminate R-curve
Specimen O1-2 (L), 20.3 x 4.50 x 2.11 mm, a0/w = 0.27
Fracture resistance (MPa √m)
Crack length (a/w)

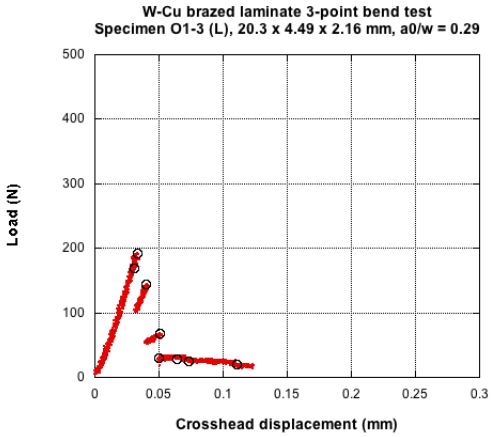
W-Cu brazed laminate 3-point bend test
Specimen O1-3 (L), 20.3 x 4.49 x 2.16 mm, a0/w = 0.29
Load (N)
Crosshead displacement (mm)

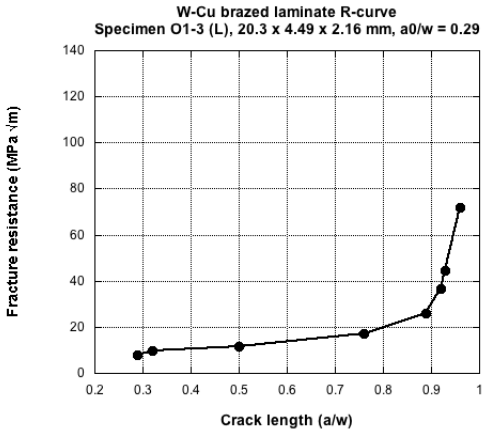
W-Cu brazed laminate R-curve
Specimen O1-3 (L), 20.3 x 4.49 x 2.16 mm, a0/w = 0.29
Fracture resistance (MPa √m)
Crack length (a/w)

W-Cu brazed laminate: P-D curves and R-curves

T orientation specimens

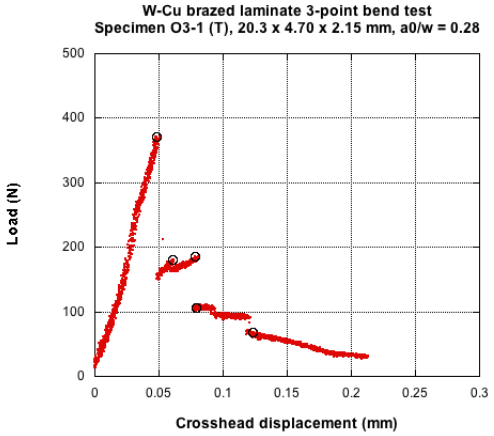

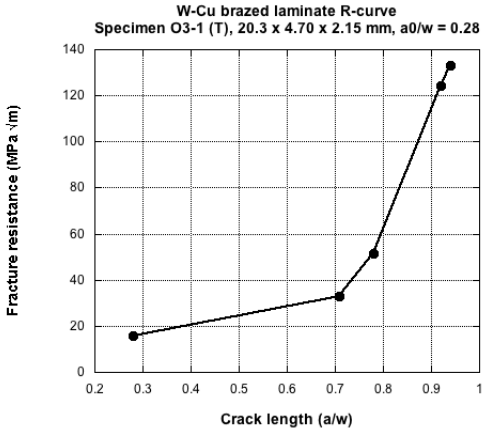

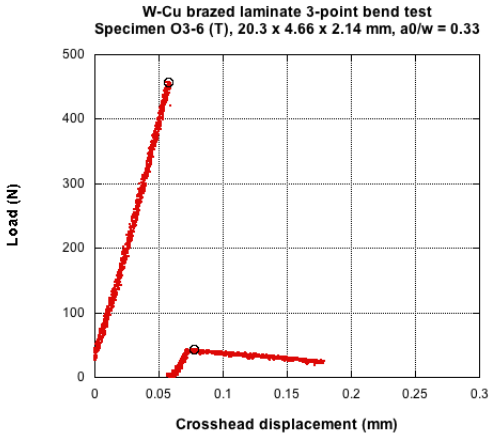

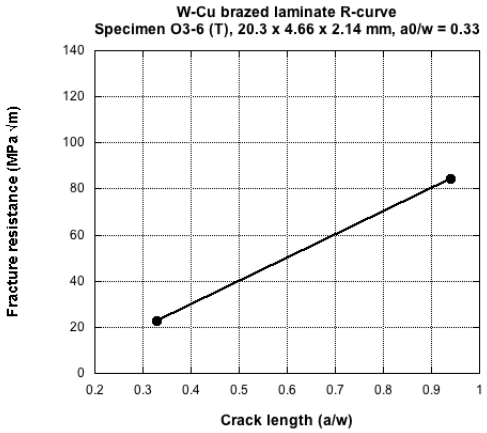

W-Cu brazed laminate: P-D curves and R-curves

Mixed orientation specimens

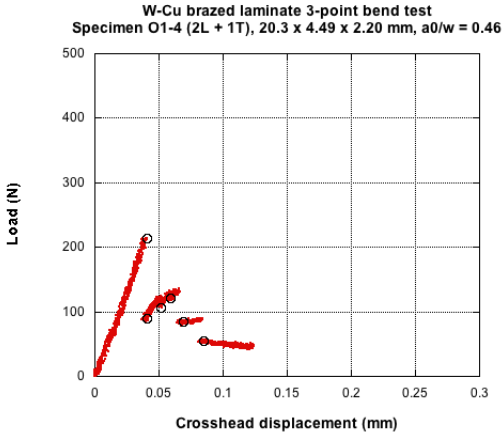

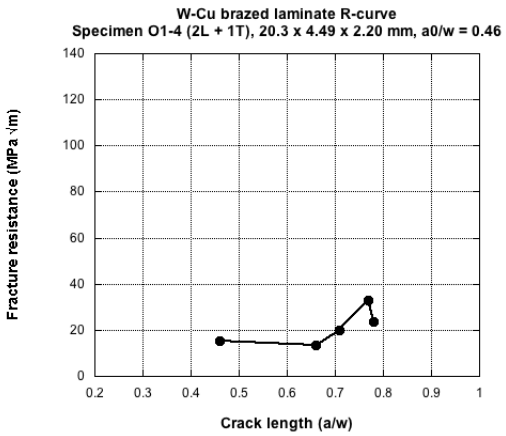

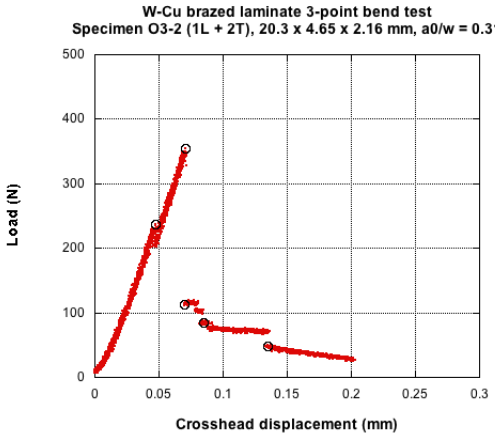

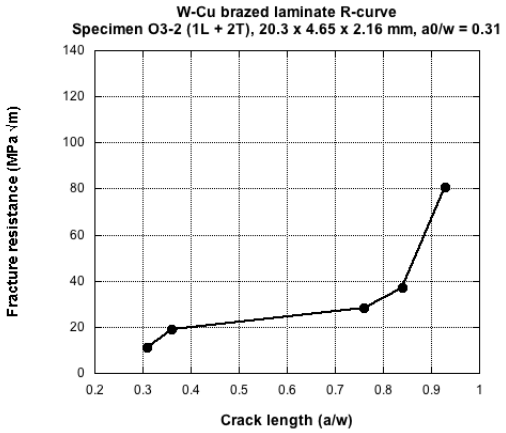

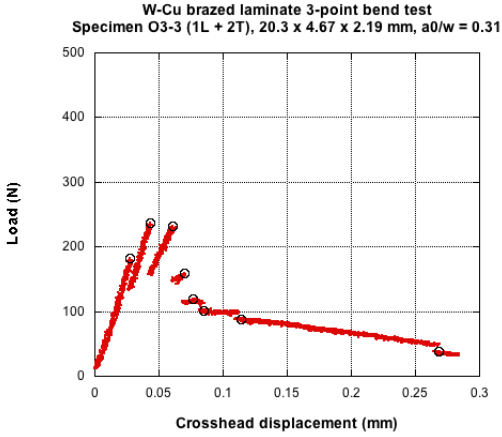
W-Cu brazed laminate 3-point bend test
Specimen O3-3 (1L + 2T), 20.3 x 4.67 x 2.19 mm, a0/w = 0.31
Load (N)
Crosshead displacement (mm)

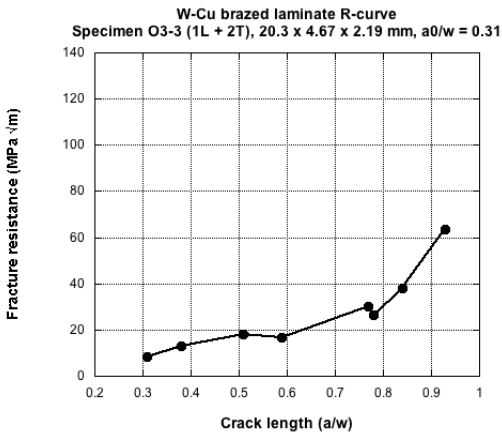
W-Cu brazed laminate R-curve
Specimen O3-3 (1L + 2T), 20.3 x 4.67 x 2.19 mm, a0/w = 0.31
Fracture resistance (MPa √m)
Crack length (a/w)

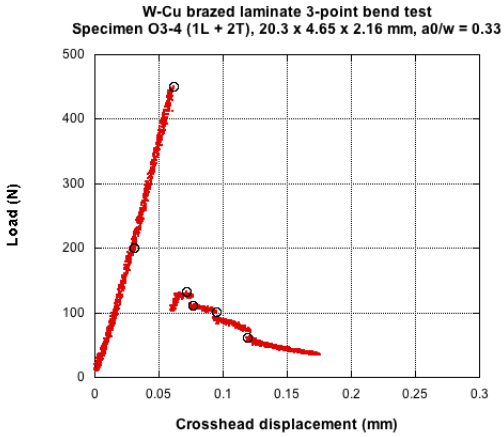
W-Cu brazed laminate 3-point bend test
Specimen O3-4 (1L + 2T), 20.3 x 4.65 x 2.16 mm, a0/w = 0.33
Load (N)
Crosshead displacement (mm)

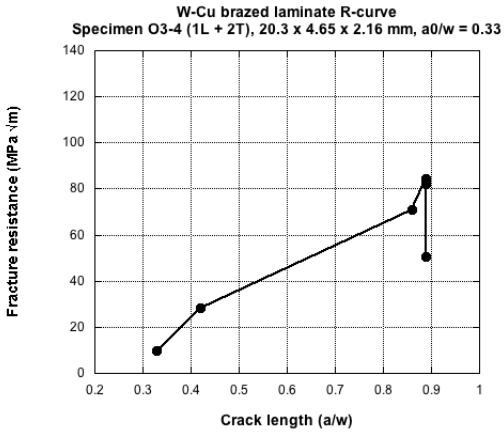
W-Cu brazed laminate R-curve
Specimen O3-4 (1L + 2T), 20.3 x 4.65 x 2.16 mm, a0/w = 0.33
Fracture resistance (MPa √m)
Crack length (a/w)

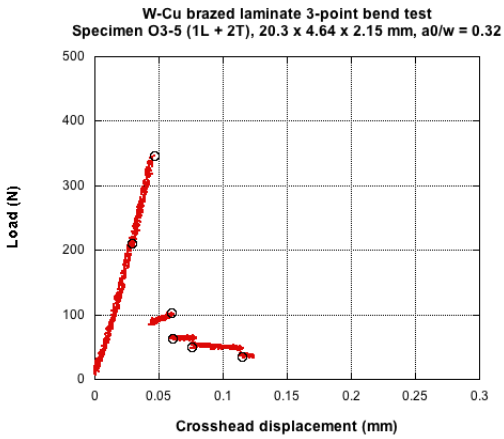
W-Cu brazed laminate 3-point bend test
Specimen O3-5 (1L + 2T), 20.3 x 4.64 x 2.15 mm, a0/w = 0.32
Load (N)
Crosshead displacement (mm)

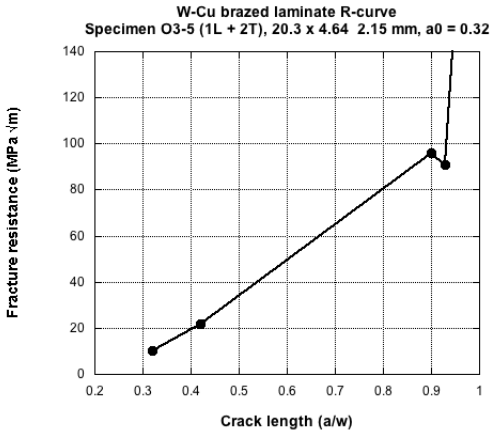
W-Cu brazed laminate R-curve
Specimen O3-5 (1L + 2T), 20.3 x 4.64 2.15 mm, a0 = 0.32
Fracture resistance (MPa √m)
Crack length (a/w)

Large-Scale Crack Bridging Code

Large - Scale Bridging Code: Case 1

```
ClearAll["Global`*"];
```

Input data

Specimen Geometry

```
w = 0.01524; (* width in m *)
s = 4 w; (* span in m *)
b = 0.00508; (* thickness in m *)
a0 = 0.41 w ; (* Pre-crack depth in m *)
shape[x_] := 1 (*Face orientation meshing shape function*)
```

Matrix properties

```
e = 172 (10^9); (* Young's modulus in Pa *)
ν = 0.33; (* Poisson's ratio *)
KIC = 8 (10^6); (* matrix toughness in Pa√m*)
```

Bridging law parameters

```
σmax = 200 (10^6); (* peak stress in Pa *)
Δ1 = 2 (10^-6); (* displacement at peak stress in m *)
Δ2 = 110 (10^-6); (* failure displacement of bridging ligaments in m *)
n = 1; (* post-peak shape parameter *)
σr = 0; (* residual stress in ductile phase *)
```

Calculation parameters

```
inc = 0.05 w; (* crack growth increment in m *)
conv = 1; (* convergence criterion for stress distribution in Pa *)
cconv = 0.0001; (* convergence criterion for bridging zone length as a fractional change *)
breakcheck = 0.9999; (*convergence criterion to resolve instances where the error in stress distribution oscillates*)
maxbreak = 5; (*maximum number of times the error can increase with each iteration in the stress disctribution calculation;
lower values may cause convergence on local minima insteaed of global minumum*)
```

Calculation

List Setup

```
a1 = a0 + inc; (* first calculated crack length *)
c = a0; (* set the initial bridging zone edge as the precrack length *)
a = a1; (* set the first crack growth increment for calculating K_TR *)
ee = e / (1 - ν^2); (* Plane strain Young's modulus *)
gg = e / (2 + 2 ν); (* Shear modulus *)
σguess = σmax; (* guess for crack face traction in Pa *)
ninc = Round[(w - a0) / inc];

(* Creates lists that will be filled during iteration, starting from initial values *)
alist = {a0}; (*list of all crack lengths used to calculate the R-curve*)
clist = {a0}; (*list for values of the end of the bridging zone calculated for each crack length*)
Klist = {KIC}; (*list of K_TR values*)
plist = {0}; (*list of applied loads*)
dlist = {0}; (*list of load-point displacements*)
error = {0}; (*list of the convergent error for the stress distribution for each crack length*)
finalerrordist = {}; (*list of the distribution of bridging-stress errors along the crack face for each crack length*)
finalstressevolution = {}; (*list of the stress distributions for each crack length*)
finalcrackevolution = {}; (*list of the crack shapes for each crack length*)
finalopeningevolution = {}; (*list of crack opening displacement distributions*)
finalclosingevolution = {}; (*list of crack closing displacement distributions*)
points = {0}; (*number of points in the mesh for each crack length*)
```

Function Definitions

```
(* Bridging law *)
σb[u_] := Piecewise[{{0, u < 0}, {(σmax - σr) (u / Δ1), 0 ≤ u ≤ Δ1}, {(σmax / 2) (1 - (u - Δ1) / (Δ2 - Δ1)) ^ n + (σmax / 2) (1 - ((u - Δ1) / (Δ2 - Δ1)) ^ (1 / n)), Δ1 < u ≤ Δ2},
    {0, Δ2 < u}}];

(* Correction factor for 3pb K_{I,P} *)
F1[x_] := Pi ^ -0.5 (1.99 - x (1 - x) (2.15 - 3.93 x + 2.7 x^2)) / ((1 + 2 x) (1 - x) ^ 1.5);

(*Correction factor for 3pb K_{I,F} *)
g1[x_] := 0.46 + 3.06 x + 0.84 (1 - x) ^ 5 + 0.66 x^2 (1 - x) ^ 2;
g2[x_] := -3.52 x^2;
g3[x_] := 6.17 - 28.22 x + 34.54 x^2 - 14.39 x^3 - (1 - x) ^ 1.5 - 5.88 (1 - x) ^ 5 - 2.64 x^2 (1 - x) ^ 2;
g4[x_] := -6.63 + 25.16 x - 31.04 x^2 + 14.41 x^3 + 2 (1 - x) ^ 1.5 + 5.04 (1 - x) ^ 5 + 1.98 x^2 (1 - x) ^ 2;
G[x_, y_] := g1[y] + g2[y] x + g3[y] x^2 + g4[y] x^3;
F2[x_, y_] := G[x, y] / (1 - (y)) ^ 1.5 / (1 - (x) ^ 2) ^ 0.5;

(* Stress intensity at crack tip due to a pair of point forces on the crack face *)
KIF[f_, x_, a_] := 2 f / (Pi a) ^ 0.5 F2[x / a, a / w];

(* Stress intensity at the crack tip due to remote loading in 3-point bending *)
KIP[P_, a_] := (6 / w ^ 2) (P s / 4) (Pi a) ^ 0.5 F1[a / w]; (*P (Pi a)^0.5 F3[a/w];*)

(*Crack opening displacements from remote loading*)
ΔP[z_] := 2 / ee NIntegrate[KIP[Pguess, x] D[KIF[f, z, x], f], {x, z, a}, Method → {Automatic, "SymbolicProcessing" → 0}, MaxRecursion → 0];

(*Crack closing displacements from bridging - requires nested numerical integration*)
ΔFinner[z_?NumericQ, a_?NumericQ] := NIntegrate[KIF[σx[aaa], aaa, a], {aaa, c, z}, Method → {Automatic, "SymbolicProcessing" → 0}, MaxRecursion → 0];

ΔF[z_, zz_] := 2 / ee NIntegrate[ΔFinner[aa, aa] D[KIF[f, z, aa], f], {aa, zz, a}, Method → {Automatic, "SymbolicProcessing" → 0}, MaxRecursion → 0];

(*Remote load (3pb) for specified crack length and applied stress intensity*)
P[KI_, a_] := KI / (6 s / (4 w ^ 2) (Pi a) ^ 0.5 F1[a / w]);

(*Function used in calculation of load-point displacements*)
V2[x_] := (x / (1 - x)) ^ 2 (5.58 - 19.57 x + 36.82 x^2 - 34.94 x^3 + 12.77 x^4);

(*Initial guess for bridging zone stress distribution*)
σx = Interpolation[{{-20 ^ -10, 0}, {c - 10 ^ -10, 0}, {c, σguess}, {a, σguess}, {a + 10 ^ -10, 0}, {w, 0}}, InterpolationOrder → 1];

(*Face orientation meshing shape function*)
shape[x_] := 1
```

Iterative Calculation

```
(*Iterator to keep track of which crack increment is being calculated*)
loop = 0;

(*Output useful information about the state of the calculation*)
Print["Crack length (a/w), increments remaining, and error"]
Dynamic[{a / w, loop - ninc, εsum}]

While[a < w,

  loop++; (*keep track of iteration number*)

  Label["resetc"]; (*if the bridging zone size is changing, the calculation will restart from here*)

  (*Ratios for scaling the distribution of guess points when the bridging zone changes size*)
  If[loop == 1, (*If this loop is removed, the mesh will have the same density for each crack length;
   otherwise the same number of points will be used for each iteration. The non-
    adaptive strategy has not shown significant error in tests of the code, and it significantly reduces computation time. *)
   scale1 = (a - c) / (a1 - a0);
   scale2 = c / a0;

   (*These values can be adjusted: higher numbers mean a denser mesh and longer calculation time*)
   xxx1 = Round[10 scale2]; (*mesh density in the short region near crack mouth*)
   xxx2 = Round[10 scale2]; (*mesh density for the majority of the non-bridged portion of the crack*)
   xxx3 = Round[10 scale2]; (*mesh density in the non-bridged region near the edge of the bridging zone*)
   xxx4 = Round[40 scale1]; (*mesh density in the short region in the bridging zone near its edge*)
   xxx5 = Round[15 scale1]; (*mesh density for the majority of the bridging zone*)
   xxx6 = Round[40 scale1]; (*mesh density near the crack tip*)

   (*Define the mesh of x-values at which the crack face displacements and stresses will be calculated*)
   cdata = Join[Array[# * 0.03 / xxx1 &, xxx1 + 1, 0], Array[0.03 + # (0.96 - 0.03) / xxx2 &, xxx2, 1], Array[0.96 + # * (1 - 0.96) / xxx3 &, xxx3 - 1, 1]];

   bridgex = Join[Array[# * 0.25 / xxx4 &, xxx4, 1], Array[0.25 + # (0.75 - 0.25) / xxx5 &, xxx5, 1], Array[0.75 + # (1 - 0.75) / xxx6 &, xxx6, 1]]
  ];

  (*mesh of points for calculating stress distribution and crack-face displacements*)
  guessx = Sort[Join[cdata c, {c - 10 ^ -10, c, c + 10 ^ -10}, c + bridgex (a - c)]];

  (*Set an initial value for the error in the stress distribution and create an empty list for the series of error values*)
  εsum = 1 000 000 000. ee; (*an arbitrarily high initial guess value that will be higher than the convergence criterion *)
  elist = {εsum}; (*a list that will hold the error in the stress distribution and allow for convergence checks*)

  (*Create lists for the internal iteration process, where the lowest-error solution will be put into the main solution list*)
  stressevolution = {}; (*holds the stress distribution list as it converges; the convergent value is saved in the list defined above*)
  crackevolution = {}; (*same function, for crack shape*)
  closingevolution = {}; (*same function, for closing displacements*)
  openingevolution = {}; (*same function, for opening displacements*)
  Klist1 = {}; (*same function, for K_{IR}*)
  plist1 = {}; (*same function, for P*)
  error1 = {}; (*same function, for error in stress distribution*)
  errordist = {}; (*same function, for distribution of errors on crack face*)

  break = 0; (*initial value for a counter that allows a certain number of increases in error to occur,
  in an attempt to move past local minima towards the global minimum*)
```

```
(* Iterative loop that calculates opening profile and stresses using stress distribution convergence criterion *)
While[εsum > conv,

 (*A check to make sure that the mesh of x-values does not force the code to attempt to make any calculations beyond the crack tip*)
 While[guessx[[Length[guessx]]] > a, guessx = Delete[guessx, -1]];

 (*Calculate the total stress intensity reduction due to the bridging zone, the applied stress intensity, and applied load*)
 Clear[ΔKIF, KIR, Pguess];
 ΔKIF = NIntegrate[KIF[ shape[aaa] σx[aaa], aaa, a], {aaa, c, a}, Method → {Automatic, "SymbolicProcessing" → None}, MaxRecursion → 0];
 (*calculated stress intensity shielding due to bridging zone;
 integrals are optimized for speed and errors are reduced by multiple iterative passes*)
 KIR = KIC + ΔKIF; (*calculated fracture resistance*)
 Pguess = P[KIR, a]; (*calculated applied load*)

 (*Calculate the constant value for crack face closing displacements at all points behind the bridging zone*)
 Clear[opening, closing, Δnet, σdist];

 (*Calculate crack face opening displacements at all mesh points*)
 opening = Array[If[guessx[[#]] ≥ a, 0, Re[ΔP[guessx[[#]]], 10^-10] &, Length[guessx]];

 (*Calculate crack face closing displacements at all mesh points*)
 (*using this loop structure prevents memory overflow*)
 counter1 = 1;
 closing = Re[Reap[
       Do[
        Sow[
         If[guessx[[counter1]] ≤ c,
          ΔF[guessx[[counter1]], c],
          ΔF[guessx[[counter1]], guessx[[counter1]]]
         ]
        ];
        ++counter1;
        , {Length[guessx]}
       ]
      ]
      [[2]]
     [[1]]
  ];

 (*Calculate net crack face displacements, preventing negative values*)
 Δnet = Array[If[opening[[#]] - closing[[#]] < 0, 0, opening[[#]] - closing[[#]]] &, Length[guessx]];

 (*Calculate crack face stresses at all mesh points using bridging law*)
 σdist =  Array[ Re[σb[Δnet[[#]]]] &, Length[guessx]];

 (*Ensure that there is no stress behind the bridging zone; broken ligaments are handled by the definition of σdist*)
 Do[σdist = Delete[σdist, 1]
  , {Length[Select[guessx, # < c &]]}];
 Do[PrependTo[σdist, 0]
  , {Length[Select[guessx, # < c &]]}];

 (*Make sure there are no undefined points in the functions over the entire width of the specimen by adding the values of each distribution at x=
  w*)
 AppendTo[guessx, w];
 AppendTo[σdist, 0];
 AppendTo[Δnet, 0];
 AppendTo[closing, 0];
 AppendTo[opening, 0];

 (*Interpolate over the stress distribution*)
 Clear[σinterp];
 σinterp = Interpolation[Transpose@{guessx, σdist}, InterpolationOrder → 1];

 (*Calculate the error in stress at each mesh point and sum absolute values for a total error*)
 εx = σdist - Array[ Re[shape[guessx[[#]]] σx[guessx[[#]]]] &, Length[guessx]];
 εsum = Sum[Abs[εx[[x]]], {x, Length[εx]}];

 (*Safety checks to prevent infinite looping*)
 check = (Min[εlist] - εsum) / Min[εlist];
 If[check ≤ 0, ++break];
 If[break > maxbreak, Break[]];
 If[break > 0, If[Abs[check] > breakcheck, Break[]]];

 (*Record the calculated values for this intermediate iteration to allow for examination of how the distribution converges to a self-
  consistent solution*)
 AppendTo[stressevolution, Transpose@{guessx, σdist}];
 AppendTo[crackevolution, Transpose@{guessx, Δnet}];
 AppendTo[openingevolution, Transpose@{guessx, opening}];
 AppendTo[closingevolution, Transpose@{guessx, closing}];
 AppendTo[Klist1, KIR];
 AppendTo[plist1, Pguess];
 AppendTo[error1, εsum];
 AppendTo[errordist, Transpose@{guessx, εx}];
 AppendTo[εlist, εsum];

 Clear[σx];
 (*update the stress distribution for the next iteration*)
 σx = σinterp;

 (*stop if any of the stress distributions in the list are identical*)
 If[Min[εlist] == 0, Break[]];

];
```

```
  cguess = c; (*save the current end of the bridging zone for comparison*)

  result = Extract[Position[error1, Min[error1]] , {1, 1}]; (*make sure that the lowest-error solution is recorded later on*)

  Clear[crackshape, ccheck];

  crackshape = Interpolation[crackevolution[[result]], InterpolationOrder → 1]; (*define a continuous function for the crack shape*)

  ccheck = If[Max[Transpose[crackevolution[[result]]][[2]]] ≥ Δ2, x /. FindRoot[crackshape[x] == Δ2, {x, a0 / 2}], 0];
  (*define the point in the crack shape that reaches the failure displacement of the reinforcement*)

  c = Max[ccheck, a0]; (*update the bridging zone length*)

  If[Abs[(c - cguess) / cguess] ≥ cconv, Goto["resetc"]]; (*check convergence criterion for brisging zone length*)

  (*Record convergent solutions for this crack length*)
  AppendTo[alist, a];
  AppendTo[clist, c];
  AppendTo[Klist, Klist1[[result]]];
  AppendTo[plist, plist1[[result]]];
  AppendTo[error, error1[[result]]];
  AppendTo[finalstressevolution, stressevolution[[result]] ];
  AppendTo[finalcrackevolution, crackevolution[[result]] ];
  AppendTo[finalopeningevolution, openingevolution[[result]] ];
  AppendTo[finalclosingevolution, closingevolution[[result]] ];
  AppendTo[finalerrordist, errordist[[result]]];
  AppendTo[points, Length[guessx]];

  (* Increase crack length and increase counter for loop *)
  a += inc;
 ];
(* Calculate load-displacement curve *)
qq = 1;
Do[
  ++qq;
  Clear[σx];
  σx = Interpolation[finalstressevolution[[qq - 1]], InterpolationOrder → 1];
  Δnc = plist[[qq]] (s^3 / (4 ee w^3) + s / (2 w) (3 / (4 gg) - 3 / (10 ee) - 3 ν / (4 ee)) - 0.21 / ee);
  Δc = 6 plist[[qq]] s^2 / (4 ee w^2) V2[alist[[qq]] / w];
  Δbrinner[z_?NumericQ] := NIntegrate[KIF[σx[xx], xx, z], {xx, clist[[qq]], z}, Method → {Automatic, "SymbolicProcessing" → None}];
  Δbr = Re[2 / ee NIntegrate[Δbrinner[x] D[KIP[P, x], P], {x, clist[[qq]], alist[[qq]]}, Method → {Automatic, "SymbolicProcessing" → None}]];
  d = (Δc + Δnc) - Δbr;
  AppendTo[dlist, d];
  , {Length[plist] - 1}];

(*Set crack length to the final value*)
a = alist[[Length[alist]]];
```

Solution Output

```
(*Output a table of values from the calculation*)
data = Transpose[{Round[alist * 1000, 0.01], Round[alist / w, 0.01], Klist / 1 000 000, Round[plist b, 0.01], Round[dlist * 1000, 0.001],
    Round[(alist - clist) * 1000, 0.001], Round[error / 1 000 000, 0.001], points}];
PrependTo[data, {"mm", "-", "MPa" Superscript["m", "0.5"], "N", "mm", "mm", "MPa", "#"}];
PrependTo[data, {"a", "a/w", "K_IR", "P", "D", "LSB size", "Error-σ", "Points"}];
Grid[data, Frame → All]

(*Plot the bridging law*)
Plot[σb[u] , {u, 0, Δ2}, PlotLabel → "Bridging Law", AxesLabel → {"Displacement (m)", "Stress (Pa)"}, PlotStyle -> Thickness[Large],
 PlotRange → {{0, 1.2 Δ2}, {0, σmax}}]

Clear[rcurve, loaddisp];

(*Plot the resistance curve*)
rcurve = Transpose@{(alist) / w, Klist / 1 000 000};
ListLinePlot[rcurve, PlotRange → {{a0 / w, 1}, {0, Max[Klist] / 1 000 000}}, Epilog → Point[rcurve], PlotLabel → "Resistance curve",
 AxesLabel → {"Crack extension (m)", "Fracture resistance (Pa m^0.5)"}, AxesOrigin → {a0 / w, 0}, PlotStyle -> {{Thick, Blue}}]

(*Load-displacement curve is normalized by values for unbridged specimen*)
pp = P[KIC, a0];(*calculate pure-matrix failure load*)
Δnc = pp (s^3 / (4 ee w^3) + s / (2 w) (3 / (4 gg) - 3 / (10 ee) - 3 ν / (4 ee)) - 0.21 / ee);
Δc = 6 pp s^2 / (4 ee w^2) V2[a0 / w];
dd = Δc + Δnc;(*calculate pure-matrix failure displacement*)
loaddisp = Transpose@{dlist / dd, plist / pp};
ListLinePlot[loaddisp, PlotRange → {{0, Max[dlist] / dd}, {0, Max[plist] / pp}}, Epilog → Point[loaddisp], PlotLabel → "Load-displacement curve",
 AxesLabel → {"Load-point displacement (m)", "Load (N)"}, PlotStyle → {{Thick, Blue}, {Thick, Black, Dashed}}]

(*Plot the evolution of the crack shape over the entire specimen*)
(*grid lines show location of precrack and the failure displacement of the reinforcement*)
Show[Array[ListLinePlot[finalcrackevolution[[#]], PlotRange → All, PlotStyle -> Thickness[Large]] &, Length[finalcrackevolution]],
 PlotRange → {{0, w}, {0, Max[finalcrackevolution[[All, All, 2]]]}}, GridLines → {{a0}, {Δ2}}, PlotRangePadding → None, AxesOrigin → {0, 0},
 PlotLabel → "Crack growth evolution", AxesLabel → {"Position (m)", "Crack opening (m)"}]

(*Plot the crack shape only for the bridging zone, from the precrack to w*)
Show[Array[ListPlot[finalcrackevolution[[#]], PlotRange → All, PlotStyle -> Thickness[Large]] &, Length[finalcrackevolution]],
 PlotRange → {{a0, w}, {0, Δ2}}, PlotRangePadding → None, AxesOrigin → {a0, 0}, PlotLabel → "Crack growth evolution (Bridging zone only)",
 AxesLabel → {"Position (m)", "Crack opening (m)"}]

(*Plot the opening displacements used in the calculation*)
Show[Array[ListPlot[finalopeningevolution[[#]], PlotRange → All, PlotStyle -> Thickness[Large]] &, Length[finalopeningevolution]],
 PlotRange → {{0, w}, {0, Max[finalopeningevolution[[All, All, 2]]]}}, PlotRangePadding → None, AxesOrigin → {0, 0},
 PlotLabel → "Opening displacements only", AxesLabel → {"Position (m)", "Displacement (m)"}]

(*Plot the closing displacements used in the calculation*)
Show[Array[ListPlot[finalclosingevolution[[#]], PlotRange → All, PlotStyle -> Thickness[Large]] &, Length[finalclosingevolution]],
 PlotRange → {{0, w}, {0, Max[finalclosingevolution[[All, All, 2]]]}}, PlotRangePadding → None, AxesOrigin → {0, 0},
 PlotLabel → "Closing displacements only", AxesLabel → {"Position (m)", "Displacement (m)"}]
```

```
(*Plot the evolution of the stress distribution on the crack face with overlaid error bars*)
Needs["ErrorBarPlots`"]
Show[
 Array[
  ErrorListPlot[Transpose[{Transpose[finalstressevolution[[#]]][[1]], Transpose[finalstressevolution[[#]]][[2]],
      Abs[Transpose[finalerrordist[[#]]][[2]]]}],
    ErrorBarFunction → Function[{coords, errs}, {Opacity[1, Red], Line[{coords - {0, errs[[2, 1]]}, coords + {0, errs[[2, 1]]}}]}] &,
  Length[finalstressevolution]], Array[ListLinePlot[finalstressevolution[[#]]] &, Length[finalstressevolution]], PlotRange → {{a0, w}, {0, σmax}},
 PlotRangePadding → None, AxesOrigin → {a0, 0}, PlotLabel → "Crack stress distribution", AxesLabel → {"Position(m)", "Stress (Pa)"}]
```

a	a/w	K_{IR}	P	D	LSB size	Error-σ	Points
mm	-	MPa $m^{0.5}$	N	mm	mm	MPa	#
6.25	0.41	8	0.	0.	0.	0.	0
7.01	0.46	15.3063	1019.33	0.044	0.762	0.	129
7.77	0.51	21.6935	1237.2	0.059	1.524	0.	129
8.53	0.56	29.1866	1406.1	0.073	2.286	0.	129
9.3	0.61	38.2513	1529.33	0.088	3.048	0.	129
10.06	0.66	50.047	1622.17	0.105	3.81	0.	129
10.82	0.71	65.3083	1662.5	0.124	4.572	0.	129
11.58	0.76	84.3083	1611.76	0.143	5.334	0.	129
12.34	0.81	106.719	1433.22	0.159	6.096	0.	129
13.11	0.86	126.131	1067.39	0.175	6.708	0.	129
13.87	0.91	144.073	624.8	0.214	5.339	0.	129
14.63	0.96	177.653	226.24	0.369	3.329	0.	129

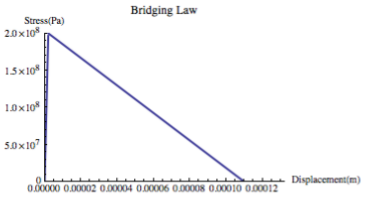

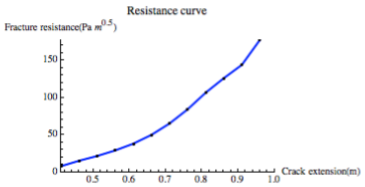

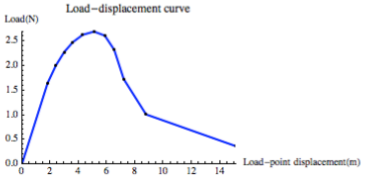

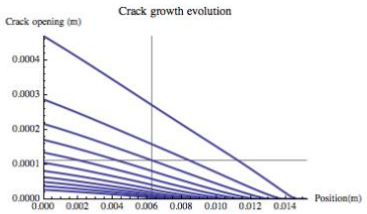

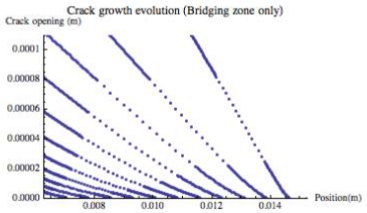

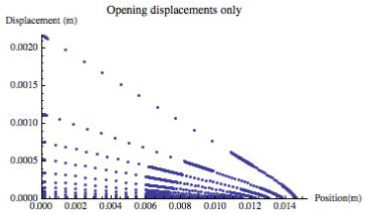

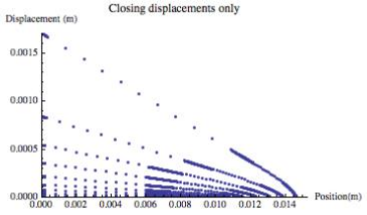

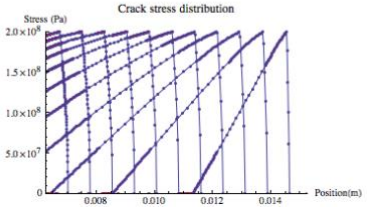

Large - Scale Bridging Code: Case 2

```
ClearAll["Global`*"];
```

Input data

R-Curve and Bridging Law Guess

```
(* Input the R-curve points in lists of a/w and K_IR (MPa) *)
rcurve = Transpose@{{0.5`, 0.52`, 0.54`, 0.56`, 0.58`, 0.6`, 0.65`, 0.7`, 0.75`, 0.8000000000000002`},
    {10.6567122438882`, 13.25389394589456`, 16.340948701249737`, 19.53250502206072`,
     22.906565213184184`, 26.652268761857048`, 38.15539941713198`, 54.45012313651892`,
     80.0983111463113`, 122.29455710376598`}};

rcurveint = Interpolation[rcurve, InterpolationOrder → 1];
```

Bridging Law Guess Values

```
σmax = 1 (10^6); (* peak stress in Pa *)
Δ1 = 0.1 (10^-6); (* displacement at peak stress in m *)
n = 0.0001; (*variable to describe the shape of post-peak curve*)
Δ2 = 350 (10^-6); (* failure displacement of bridging ligaments in m *)
σr = 0; (* residual stress in ductile phase *)
```

Specimen Geometry

```
s = 0.02028698; (* span in m *)
w = s / 4; (* width in m *)
b = w / 2; (* thickness in m *)
shape[x_] := 1; (*Face orientation meshing shape function*)
```

Matrix properties

```
e = 410 (10^9); (* Young's modulus in Pa *)
ν = 0.28; (* Poisson's ratio *)
```

Calculation parameters

```
conv =  0.1*10^6; (* convergence criterion for stress distribution in Pa *)
cconv = 0.0001; (* convergence criterion for bridging zone length as a fractional change *)
breakcheck = 0.9999; (*convergence criterion to resolve instances where the error in stress
 distribution oscillates*)
maxbreak = 5; (*maximum number of times the error can increase with each iteration in the stress
 disctribution calculation; lower values may cause convergence on local minima insteaed of global minumum*)
Δ1step = 0.1*10^-6; (* step size in Δ1 for simultaneous calculation of σmax and Δ1 *)
nconv = 0.01; (*convergence criterion for n as a fractional change*)
npower = 5; (*gain exponent to increase convergence speed for n*)
```

Calculation

List Setup

```
a0 = rcurve[[1, 1]] w ; (* Pre-crack depth in m comes from R-curve*)
a1 = rcurve[[2, 1]] w; (* first calculated crack length comes from R-curve*)
KIC = rcurve[[1, 2]] (10^6); (* matrix toughness comes from R-curve*)

c = a0; (* set the initial bridging zone edge as the precrack length *)
a = a1; (* set the first crack growth increment for calculating K_IR *)
ee = e / (1 - ν^2); (* Plane strain Young's modulus *)
gg = e / (2 + 2 ν); (* Shear modulus *)
σguess = σmax; (* guess for crack face traction in Pa *)
```

```
(* Creates lists that will be filled during iteration, starting from initial values *)
alist = {a0};(*list of all crack lengths used to calculate the R-curve*)
clist = {a0};(*list for values of the end of the bridging zone calculated for each crack length*)
Klist = {KIC};(*list of K_IR values*)
plist = {0};(*list of applied loads*)
dlist = {0};(*list of load-point displacements*)
error = {0};(*list of the convergent error for the stress distribution for each crack length*)
finalerrordist = {};(*list of the distribution of bridging-
 stress errors along the crack face for each crack length*)
finalstressevolution = {};(*list of the stress distributions for each crack length*)
finalcrackevolution = {};(*list of the crack shapes for each crack length*)
finalopeningevolution = {};(*list of crack opening displacement distributions*)
finalclosingevolution = {};(*list of crack closing displacement distributions*)
points = {0};(*number of points in the mesh for each crack length*)

σmaxlist = {};
Δ1list = {};
nlist = {};
```

Function Definitions

```
(* Bridging law *)
σb[Δ_] :=
  Piecewise[{{0, Δ < 0}, {(σmax - σr) (Δ / Δ1), 0 ≤ Δ ≤ Δ1},
    {(σmax / 2) (1 - (Δ - Δ1) / (Δ2 - Δ1)) ^ n + (σmax / 2) (1 - ((Δ - Δ1) / (Δ2 - Δ1)) ^ (1 / n)), Δ1 < Δ ≤ Δ2}, {0, Δ2 < Δ}}];

(* Correction factor for 3pb K_I,P *)
F1[x_] := Pi ^ -0.5 (1.99 - x (1 - x) (2.15 - 3.93 x + 2.7 x ^ 2)) / ((1 + 2 x) (1 - x) ^ 1.5);

(*Correction factor for 3pb K_I,P ;*)
g1[x_] := 0.46 + 3.06 x + 0.84 (1 - x) ^ 5 + 0.66 x ^ 2 (1 - x) ^ 2;
g2[x_] := -3.52 x ^ 2;
g3[x_] := 6.17 - 28.22 x + 34.54 x ^ 2 - 14.39 x ^ 3 - (1 - x) ^ 1.5 - 5.88 (1 - x) ^ 5 - 2.64 x ^ 2 (1 - x) ^ 2;
g4[x_] := -6.63 + 25.16 x - 31.04 x ^ 2 + 14.41 x ^ 3 + 2 (1 - x) ^ 1.5 + 5.04 (1 - x) ^ 5 + 1.98 x ^ 2 (1 - x) ^ 2;
G[x_, y_] := g1[y] + g2[y] x + g3[y] x ^ 2 + g4[y] x ^ 3;
F2[x_, y_] := G[x, y] / (1 - (y)) ^ 1.5 / (1 - (x) ^ 2) ^ 0.5;

(* Stress intensity at crack tip due to a pair of point forces on the crack face *)
KIF[f_, x_, a_] := 2 f / (Pi a) ^ 0.5 F2[x / a, a / w];

(* Stress intensity at the crack tip due to remote loading in 3-point bending *)
KIP[P_, a_] := (6 / w ^ 2) (P s / 4) (Pi a) ^ 0.5 F1[a / w]; (*P (Pi a)^0.5 F3[a/w];*)

(*Crack opening displacements from remote loading*)
ΔP[z_] :=
  2 / ee NIntegrate[KIP[Pguess, x] D[KIF[f, z, x], f], {x, z, a}, Method → {Automatic, "SymbolicProcessing" → 0},
    MaxRecursion → 0];

(*Crack closing displacements from bridging - requires nested numerical integration*)
ΔFinner[z_?NumericQ, a_?NumericQ] :=
  NIntegrate[KIF[σx[aaa], aaa, a], {aaa, c, z}, Method → {Automatic, "SymbolicProcessing" → 0},
   MaxRecursion → 0];

ΔF[z_, zz_] :=
  2 / ee NIntegrate[ΔFinner[aa, aa] D[KIF[f, z, aa], f], {aa, zz, a},
    Method → {Automatic, "SymbolicProcessing" → 0}, MaxRecursion → 0];

(*Remote load (3pb) for specified crack length and applied stress intensity*)
P[KI_, a_] := KI / (6 s / (4 w ^ 2) (Pi a) ^ 0.5 F1[a / w]);

(*Function used in calculation of load-point displacements*)
V2[x_] := (x / (1 - x)) ^ 2 (5.58 - 19.57 x + 36.82 x ^ 2 - 34.94 x ^ 3 + 12.77 x ^ 4);

Δo = Δ1;(*note the initial Δ1 guess*)

(*Initial guess for bridging zone stress distribution*)
σx0 = Interpolation[{{-20 ^ -10, 0}, {c - 10 ^ -10, 0}, {c, σguess}, {a, σguess}, {a + 10 ^ -10, 0}, {w, 0}},
   InterpolationOrder → 1];
```

Estimate σ_{max} and Δ_1 Simultaneously

```
σmaxcheck = 1;(*initial value for variable that determines when to stop calculaing Δ1 and σmax estimates*)

(*Output useful information about the state of the calculation*)
Print["Crack length (a/w), σmax (MPa), Δ1 (μm), n, and Δ2 (μm)"]
Dynamic[{a/w, σmax*10^-6, Δ1*10^6, n, Δ2*10^6}]
Dynamic[ListPlot[Transpose@{Δ1list, σmaxlist}]]

While[σmaxcheck > 0, (*this loop will stop when the calculated Δ1 vs. σmax curve passes its maximum*)

  a = a0 + (Pi/2 (ee/4/KIC(Δ1))^2);
  (* set a short increment in crack growth such that the bridging zone displacements will not
   go past the guessed Δ1 value *)

  (*The adaptive mesh is very important for this calculation*)

  (*Ratios for scaling the distribution of guess points when the bridging zone changes size*)
  scale1 = (*(a-c)/(a1-a0)*)1;
  scale2 = c/a0;

  (*These values can be adjusted: higher numbers mean a denser mesh and longer calculation time*)
  xxx1 = Round[5 scale2]; (*mesh density in the short region near crack mouth*)
  xxx2 = Round[5 scale2]; (*mesh density for the majority of the non-bridged portion of the crack*)
  xxx3 = Round[5 scale2]; (*mesh density in the non-bridged region near the edge of the bridging zone*)
  xxx4 = Round[25 scale1]; (*mesh density in the short region in the bridging zone near its edge*)
  xxx5 = Round[50 scale1]; (*mesh density for the majority of the bridging zone*)
  xxx6 = Round[100 scale1]; (*mesh density near the crack tip*)

  (*Define the mesh of x-values at which the crack face displacements and stresses will be calculated*)
  cdata = Join[Array[#*0.03/xxx1 &, xxx1+1, 0], Array[0.03+#*(0.96-0.03)/xxx2 &, xxx2, 1],
    Array[0.96+#*(1-0.96)/xxx3 &, xxx3-1, 1]];

  bridgex = Join[Array[#*0.25/xxx4 &, xxx4, 1], Array[0.25+#(0.75-0.25)/xxx5 &, xxx5, 1],
    Array[0.75+#(1-0.75)/xxx6 &, xxx6, 1]];

  (*mesh of points for calculating stress distribution and crack-face displacements*)
  guessx = Sort[Join[cdata c, {c-10^-10, c, c+10^-10}, c+bridgex(a-c)]];

  (*Set an initial value for the error between σmax guesses*)
  σdiff = 1 000 000 000. ee; (*an arbitrarily high initial guess value that will be higher than
   the convergence criterion *)

  (*Create lists for the internal iteration process,
  where the lowest-error solution will be put into the main solution list*)
  stressevolution = {}; (*holds the stress distribution list as it converges;
  the convergent value is saved in the list defined above*)
  crackevolution = {}; (*same function, for crack shape*)
  closingevolution = {}; (*same function, for closing displacements*)
  openingevolution = {}; (*same function, for opening displacements*)
  Klist1 = {}; (*same function, for KIR*)
  plist1 = {}; (*same function, for P*)

  σmaxguess = {}; (*same function, for σmax*)
  nguess = {}; (*same function, for n*)
  Δ1guess = {}; (*same function, for Δ1*)

  break = 0; (*initial value for a counter that allows a certain number of increases in error to occur,
  in an attempt to move past local minima towards the global minimum*)
```

```
(* Iterative loop that calculates opening profile and stresses using stress distribution
 convergence criterion *)
While[σdiff > conv,

 (*A check to make sure that the mesh of x-
  values does not force the code to attempt to make any calculations beyond the crack tip*)
 While[guessx[[Length[guessx]]] > a, guessx = Delete[guessx, -1]];

 (*Calculate the total stress intensity reduction due to the bridging zone,
 the applied stress intensity, and applied load*)
 Clear[ΔKIF, KIR, Pguess];
 ΔKIF = NIntegrate[KIF[shape[aaa] σx0[aaa], aaa, a], {aaa, c, a},
   Method → {Automatic, "SymbolicProcessing" → None}, MaxRecursion → 0];
 (*calculated stress intensity shielding due to bridging zone;
 integrals are optimized for speed and errors are reduced by multiple iterative passes*)

 (*Scale the stress distribution and the corresponding σmax guess using the known K_IR value
  for this crack length*)
 Ktrue = rcurveint[a / w] * 10 ^ 6; (*the true K_IR value for the current crack length*)
 Kratio = (Ktrue - KIC) / ΔKIF; (*this is a scaling factor for the current stress intensity
  shielding value*)

 Clear[σx];
 σx[x_] := Kratio σx0[x]; (*update the stress distribution*)

 (*recalculate values and continue using the updated stress distribution*)
 Clear[ΔKIF, KIR, Pguess];
 ΔKIF = Re[NIntegrate[KIF[ shape[aaa] σx[aaa], aaa, a], {aaa, c, a},
    Method -> {Automatic, "SymbolicProcessing" -> None}]];
 KIR = KIC + ΔKIF;
 Pguess = P[KIR, a];

 σmax =  Kratio σmax; (*update the bridging law parameter guess*)

 (*Calculate the constant value for crack face closing displacements at all points behind
  the bridging zone*)
 Clear[opening, closing, Δnet, σdist];

 (*Calculate crack face opening displacements at all mesh points*)
 opening = Array[If[guessx[[#]] ≥ a, 0, Re[ΔP[guessx[[#]]], 10 ^ -10] &, Length[guessx]];

 (*Calculate crack face closing displacements at all mesh points*)
 (*using this loop structure prevents memory overflow*)
 counter1 = 1;
 closing = Re[Reap[
       Do[
        Sow[
         If[guessx[[counter1]] ≤ c,
          ΔF[guessx[[counter1]], c],
          ΔF[guessx[[counter1]], guessx[[counter1]]]
         ]
        ];
        ++counter1;
        , {Length[guessx]}
       ]
      ]
      [[2]]
     [[1]]
  ];

 (*Calculate net crack face displacements, preventing negative values*)
 Δnet = Array[If[opening[[#]] - closing[[#]] < 0, 0, opening[[#]] - closing[[#]]] &, Length[guessx]];

 (*Calculate crack face stresses at all mesh points using bridging law*)
 σdist =  Array[ Re[σb[Δnet[[#]]]] &, Length[guessx]];

 (*Ensure that there is no stress behind the bridging zone;
 broken ligaments are handled by the definition of σdist*)
 Do[σdist = Delete[σdist, 1]
  , {Length[Select[guessx, # < c &]]}];
 Do[PrependTo[σdist, 0]
  , {Length[Select[guessx, # < c &]]}];
```

```
 (*Make sure there are no undefined points in the functions over the entire width of the
   specimen by adding the values of each distribution at x=w*)
 AppendTo[guessx, w];
 AppendTo[σdist, 0];
 AppendTo[Δnet, 0];
 AppendTo[closing, 0];
 AppendTo[opening, 0];

 (*Interpolate over the stress distribution*)
 Clear[σinterp];
 σinterp = Interpolation[Transpose@{guessx, σdist}, InterpolationOrder → 1];

 (*Record the calculated values for this intermediate iteration to allow for examination
   of how the distribution converges to a self-consistent solution*)
 AppendTo[stressevolution, Transpose@{guessx, σdist}];
 AppendTo[crackevolution, Transpose@{guessx, Δnet}];
 AppendTo[openingevolution, Transpose@{guessx, opening}];
 AppendTo[closingevolution, Transpose@{guessx, closing}];
 AppendTo[Klist1, KIR];
 AppendTo[plist1, Pguess];

 (*prevent infinite loops*)
 If[σmax == σmaxguess[[-2]], Break[]];

 AppendTo[σmaxguess, σmax];
 AppendTo[Δlguess, Δl];

 (*check for convergence in the σmax guess*)
 If[Length[σmaxguess] > 1,
  σdiff = Abs[σmaxguess[[Length[σmaxguess]]] - σmaxguess[[Length[σmaxguess] - 1]]]
 ];

 (*update the stress distribution for the next iteration*)
 Clear[σx0];
 σx0 = σinterp;

];

(*update the check value that determines whether to continue calculating estimates for Δl and σmax*)
If[Length[σmaxlist] > 1, σmaxcheck = σmaxguess[[Length[σmaxguess]]] - σmaxlist[[Length[σmaxlist]]]
];

(*record convergent solutions for this crack length*)
AppendTo[σmaxlist, σmaxguess[[Length[σmaxguess]]]];
AppendTo[Δllist, Δlguess[[Length[Δlguess]]]];

(*increase Δl by the specified step size*)
Δl = Δl + Δlstep;
];
```

```
(*Select the best-guess point from the Δ1 vs. σmax estimate curve*)

delloop = 0;(*initial value for iterator*)
lmlist = {};(*create a list to fill with linear model fits*)

(*with each iteration, select one fewer point from the Δ1 vs. σmax curve to perform a linear regression,
then save the regression results in a list*)
Do[
 Clear[Δ1list2, σmaxlist2, lm];
 Δ1list2 = Drop[Δ1list, -delloop]; (*select the list of Δ1 values*)
 σmaxlist2 = Drop[σmaxlist, -delloop]; (*select the list of σmax values*)
 lm = LinearModelFit[Transpose@{Δ1list2, σmaxlist2}, x, x]; (*fit a line to the current set of points*)
 AppendTo[lmlist, lm];
 ++delloop;
 , {Length[Δ1list] - 2}]

rsquaredlist = Array[lmlist[[#]]["RSquared"] &, Length[lmlist]];
(*pull only the R^2 values from the list of linear models*)

(*Find the index of the first local maximum r-squared value,
which corresponds to the index of the "yield" point, counting from the right in Δ1list and σmaxlist*)
test = Array[rsquaredlist[[# + 1]] - rsquaredlist[[#]] &, Length[rsquaredlist] - 1];
index = Position[test, Select[test, # ≤ 0 &, 1][[1]]][[1, 1]];
(*Select the first value in the "test" list that has a negative value,
corresponding to the first local maximum in the list of R^2 values. This index corresponds to
 the point at which the plot of estimated Δ1 and σmax values starts to go nonlinear*)

(*Choose the final estimates for these two parameters*)
Δ1 = Δ1list[[-index]];
σmax = σmaxlist[[-index]];
Crack length (a/w), σmax (MPa), Δ1 (μm), n, and Δ2 (μm)
{0.8, 401.781, 1., 1.18989, 350}
```

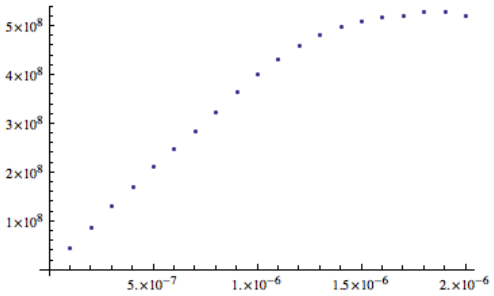

Estimate n

```
n = 100; (*high initial guesses can help n converge more quickly*)

RCurveList = {}; (*create a list to hold each successive R-curve estimate as n converges*)

(*integrate the true R-curve with respect to a/w to use for scaling the n guess*)
rcurvetotal =
  NIntegrate[rcurveint[x], {x, Transpose[rcurve][[1, 1]], Transpose[rcurve][[1, Length[rcurve]]]}];

ncheck = (1 + nconv) / 2; (*initial value for the n convergence check*)

Print["Crack length (a/w),esum, σmax(MPa),Δ1 (μm), n, and Δ2 (μm)"]
Dynamic[{a / w, esum, σmax * 10^-6, Δ1 * 10^6, n, Δ2 * 10^6}]

(*Show the convergence of the R-curves corresponding to each successive iteration in n*)
Dynamic[
 Show[
  Array[
   ListLinePlot[RCurveList[[#]], PlotStyle → Opacity[0.5, Blue]] &, Length[RCurveList] - 1
  ],
  ListLinePlot[RCurveList[[Length[RCurveList]]], PlotStyle → Opacity[1, Red]], ListPlot[rcurve],
  AxesOrigin → {0, rcurve[[1, 1]]},
  PlotRange → {{Transpose[rcurve][[1, 1]], 1},
    {0, Max[Max[Transpose[rcurve][[2]]], Max[Transpose[RCurveList[[-1]]][[2]]]]}}
 ]
]

(*Loop for varying n*)
While[ncheck > nconv,

 c = a0; (*reset the bridging zone edge to the precrack length*)
 alist = Transpose[rcurve][[1]] w;
 (*the list of crack lengths has already been defined by the true R-curve*)
 ninc = Length[alist] - 1; (*set the number of iterations to match the number of actual R-curve points*)

 (*Initial guess for bridging zone stress distribution*)
 σx = Interpolation[{{-20^-10, 0}, {c - 10^-10, 0}, {c, σmax}, {a, σmax}, {a + 10^-10, 0}, {w, 0}},
   InterpolationOrder → 1];

 loop = 2; (*start with 2 because the first calculation occurs at the second point in the R-curve*)

 clist = {a0}; (*list for values of the end of the bridging zone calculated for each crack length*)
 Klist = {KIC}; (*list of K_IR values*)
 plist = {0}; (*list of applied loads*)
 dlist = {0}; (*list of load-point displacements*)
 error = {0}; (*list of the convergent error for the stress distribution for each crack length*)
 finalerrordist = {}; (*list of the distribution of bridging-
  stress errors along the crack face for each crack length*)
 finalstressevolution = {}; (*list of the stress distributions for each crack length*)
 finalcrackevolution = {}; (*list of the crack shapes for each crack length*)
 finalopeningevolution = {}; (*list of crack opening displacement distributions*)
 finalclosingevolution = {}; (*list of crack closing displacement distributions*)
 points = {0}; (*number of points in the mesh for each crack length*)
```

```
Do[

 a = alist[[loop]];
 (*make sure that the crack lengths used in the calculation are the same as those measured in the R-
  curve*)

 (*The following is the same as in Case 1*)

 Label["resetc"];

 If[loop == 1,
  scale1 = (a - c) / (a1 - a0);
  scale2 = c / a0;

  xxx1 = Round[5 scale2];
  xxx2 = Round[5 scale2];
  xxx3 = Round[5 scale2];
  xxx4 = Round[25 scale1];
  xxx5 = Round[50 scale1];
  xxx6 = Round[100 scale1];

  cdata = Join[Array[# * 0.03 / xxx1 &, xxx1 + 1, 0], Array[0.03 + # * (0.96 - 0.03) / xxx2 &, xxx2, 1],
    Array[0.96 + # * (1 - 0.96) / xxx3 &, xxx3 - 1, 1]];

  bridgex = Join[Array[# * 0.25 / xxx4 &, xxx4, 1], Array[0.25 + # (0.75 - 0.25) / xxx5 &, xxx5, 1],
    Array[0.75 + # (1 - 0.75) / xxx6 &, xxx6, 1]]
 ];

 guessx = Sort[Join[cdata c, {c - 10^-10, c, c + 10^-10}, c + bridgex (a - c)]];

 esum = 1 000 000 000. ee;
 elist = {esum};

 stressevolution = {};
 crackevolution = {};
 closingevolution = {};
 openingevolution = {};
 Klist1 = {};
 plist1 = {};
 error1 = {};
 errordist = {};

 break = 0;

 While[esum > conv,

  While[guessx[[Length[guessx]]] > a, guessx = Delete[guessx, -1]];

  Clear[ΔKIF, KIR, Pguess];
  ΔKIF = NIntegrate[KIF[ shape[aaa] σx[aaa], aaa, a], {aaa, c, a},
    Method → {Automatic, "SymbolicProcessing" → None}, MaxRecursion → 0];
  KIR = KIC + ΔKIF;
  Pguess = P[KIR, a];

  Clear[opening, closing, Δnet, σdist];

  opening = Array[If[guessx[[#]] ≥ a, 0, Re[ΔP[guessx[[#]]]], 10^-10] &, Length[guessx]];
```

```
counter1 = 1;
closing = Re[Reap[
      Do[
       Sow[
        If[guessx[[counter1]] ≤ c,
         ΔF[guessx[[counter1]], c],
         ΔF[guessx[[counter1]], guessx[[counter1]]]
        ]
       ];
       ++counter1;
       , {Length[guessx]}
      ]
     ]
     [[2]]
    [[1]]
 ];

Δnet = Array[If[opening[[#]] - closing[[#]] < 0, 0, opening[[#]] - closing[[#]]] &, Length[guessx]];

σdist =  Array[ Re[σb[Δnet[[#]]]] &, Length[guessx]];

Do[σdist = Delete[σdist, 1]
  , {Length[Select[guessx, # < c &]]}];
Do[PrependTo[σdist, 0]
  , {Length[Select[guessx, # < c &]]}];

AppendTo[guessx, w];
AppendTo[σdist, 0];
AppendTo[Δnet, 0];
AppendTo[closing, 0];
AppendTo[opening, 0];

Clear[σinterp];
σinterp = Interpolation[Transpose@{guessx, σdist}, InterpolationOrder → 1];

εx = σdist - Array[ Re[shape[guessx[[#]]] σx[guessx[[#]]]] &, Length[guessx]];
εsum = Sum[Abs[εx[[x]]], {x, Length[εx]}];

check = (Min[εlist] - εsum) / Min[εlist];
If[check ≤ 0, ++break];
If[break > maxbreak, Break[]];
If[break > 0, If[Abs[check] > breakcheck, Break[]]];

AppendTo[stressevolution, Transpose@{guessx, σdist}];
AppendTo[crackevolution, Transpose@{guessx, Δnet}];
AppendTo[openingevolution, Transpose@{guessx, opening}];
AppendTo[closingevolution, Transpose@{guessx, closing}];
AppendTo[Klist1, KIR];
AppendTo[plist1, Pguess];
AppendTo[error1, εsum];
AppendTo[errordist, Transpose@{guessx, εx}];
AppendTo[εlist, εsum];

Clear[σx];
σx = σinterp;

If[Min[εlist] == 0, Break[]];

];
```

```
  cguess = c;

  result = Extract[Position[error1, Min[error1]] , {1, 1}];

  Clear[crackshape, ccheck];

  crackshape = Interpolation[crackevolution[[result]], InterpolationOrder → 1];

  ccheck = If[Max[Transpose[crackevolution[[result]]][[2]]] ≥ Δ2, x /. FindRoot[crackshape[x] == Δ2, {x, a0 / 2}],
    0];

  c = Max[ccheck, a0];

  If[Abs[(c - cguess) / cguess] ≥ cconv, Goto["resetc"]];

  AppendTo[clist, c];
  AppendTo[Klist, Klist1[[result]]];
  AppendTo[plist, plist1[[result]]];
  AppendTo[error, error1[[result]]];
  AppendTo[finalstressevolution, stressevolution[[result]] ];
  AppendTo[finalcrackevolution, crackevolution[[result]] ];
  AppendTo[finalopeningevolution, openingevolution[[result]] ];
  AppendTo[finalclosingevolution, closingevolution[[result]] ];
  AppendTo[finalerrordist, errordist[[result]]];
  AppendTo[points, Length[guessx]];

  loop++;

  , {ninc}];

 (*integrate the estimated R-curve with respect to a/w*)
 Clear[rcurveEst];
 rcurveEst = Transpose@{(alist) / w, Klist / 1 000 000};
 rcurveEstInt = Interpolation[rcurveEst, InterpolationOrder → 1];
 rcurveEsttotal = NIntegrate[rcurveEstInt[x],
   {x, Transpose[rcurveEst][[1, 1]], Transpose[rcurveEst][[1, Length[rcurveEst]]]}];

 rcurveratio = rcurveEsttotal / rcurvetotal; (*set a scale factor to update the n guess*)
 n = n * rcurveratio ^ npower; (*update n, using the gain exponent npower to increase the convergence speed*)

 (*update the convergence check by calculating the fractional change in n*)
 If[Length[nlist] > 0,
  ncheck = Abs[nlist[[-1]] - n] / nlist[[-1]]
 ];

 (*record the estimates for n and for the R-curve, and repeat until n converges*)
 AppendTo[nlist, n];
 AppendTo[RCurveList, rcurveEst];

]
Crack length (a/w),∈sum, σmax(MPa),Δ1 (μm), n, and Δ2 (μm)
{0.8, 65043.8, 401.781, 1., 1.18989, 350}
```